A Dynamical Systems Analysis of Movement Coordination Models

Submitted by

Sohaib Talal Hasan Al-Ramadhani

to the University of Exeter
as a thesis for the degree of

Doctor of Philosophy in Mathematics

June, 2018

Supervisors

Prof Krasimira Tsaneva-Atanasova
Dr Markus Mueller

I certify that all material in this thesis which is not my own work has been identified and that no material has previously been submitted and approved for the award of a degree by this or any other University.

Signature: .....

Abstract

In this thesis, we present a dynamical systems analysis of models of movement coordination, namely the Haken-Kelso-Bunz (HKB) model and the Jirsa-Kelso excitator (JKE).

The dynamical properties of the models that can describe various phenomena in discrete and rhythmic movements have been explored in the models' parameter space. The dynamics of amplitude-phase approximation of the single HKB oscillator has been investigated. Furthermore, an approximated version of the scaled JKE system has been proposed and analysed.

The canard phenomena in the JKE system has been analysed. A combination of slow-fast analysis, projection onto the Poincaré sphere and blow-up method has been suggested to explain the dynamical mechanisms organising the canard cycles in JKE system, which have been shown to have different properties comparing to the classical canards known for the equivalent FitzHugh-Nagumo (FHN) model. Different approaches to defining the maximal canard periodic solution have been presented and compared.

The model of two HKB oscillators coupled by a neurologically motivated function, involving the effect of time-delay and weighted self- and mutual-feedback, has been analysed. The periodic regimes of the model have been shown to capture well the frequency-induced drop of oscillation amplitude and loss of anti-phase stability that have been experimentally observed in many rhythmic movements and by which the development of the HKB model has been inspired. The model has also been demonstrated to support a dynamic regime of stationary bistability with the absence of periodic regimes that can be used to describe discrete movement behaviours.

To my wonderful family...

Acknowledgements

First of all, I am extremely grateful to my main supervisor Prof Krasimira Tsaneva-Atanasova for the patient guidance, encouragement and advice she has provided throughout my time as her student.

I would also like to thank my second supervisor Dr Markus Mueller and all the members of the Department of Mathematics in the University of Exeter for the constant support and kind advice they provided.

I am grateful to my collaborator Dr Piotr Slowinski for his invaluable insights and contribution to this thesis. I would especially like to thank my classmate Harun Baldemir who always helped whenever I needed and gave me the enjoyable studying environment.

I must express my gratitude to all my friends for all the great help they gave over the years.

I am truly grateful to my dear father Talal, my dear mother Nidhal and all my family for the love and support they have given. I owe many thanks to my wonderful wife Marwah for her continued love, care and encouragement throughout these years. Sweet thanks to my sweethearts Yaman, Sama and Hasan.

This research was supported by The Higher Committee for Education Development in Iraq (HCED) and the University of Mosul.

Contents

List of Figures

LIST OF FIGURES

Chapter 1

Introduction

Movement coordination is a goal-directed motor behaviour between two or more effectors (muscles, joints, limbs, or even different people) characterised by the dependency of movement commands to one effector (in a causal or statistical sense) on the state of the other effector(s) [1]. Motor behaviour underlies complicated coordination among different physiological systems in our body. Many mathematical models have been proposed to describe different patterns of movement coordination in various contexts, from finger tapping to human-computer interface [2–7]. In this thesis, we consider two pioneering mathematical models of movement coordination, namely the Haken-Kelso-Bunz (HKB) model [8] and the Jirsa-Kelso excitator (JKE) [9]. Our aim is to investigate further some unexplored aspects of their dynamics using dynamical systems analysis.

In this chapter, we introduce the HKB and JKE models and discuss their motivation. Then we review some existing results and address some important questions regarding the models' dynamics that we are going to consider and answer throughout this work. Finally, we state the aims and outline of the thesis.

1.1 Dynamical models of movement coordination

Human movement is a complex behaviour resulting from participation of different complex physiological subsystems; such as neural, muscular, vascular and skeletal systems, which act in a coordinated manner relative to each other and to the environment and operate at different time scales [3, 4, 10]. The relation between the

behaviour of the component subsystems and the coordination pattern, observed at the macroscale of the biological organisation, is yet barely understood [11]. Due to this compositional complexity, solving the problem of movement coordination is extremely difficult [4].

During the last four decades, various approaches have been adopted, and a large number of mathematical models have been developed to describe and predict different coordination patterns that are empirically observed in movement behaviour [2, 8, 9]. In addition, continuous criticising efforts are carried out to test, validate and improve the proposed models into a different movement tasks and contexts [2, 5–7, 12].

In this thesis, we focus on two dynamical models of movement coordination, namely the Haken-Kelso-Bunz (HKB) model and the Jirsa-Kelso excitator (JKE), which have been empirically tested and validated by comparing their solutions to the experimental data [6, 13]. The models have also been applied various movement contexts such as rhythmic and discrete movement in intra- and interpersonal motor behaviour [7, 14–16]. A brief review of the two models and their motivation is given in the following subsections.

1.1.1 Haken-Kelso-Bunz (HKB) model

According to the dynamical systems approach inspired by Synergetics (an approach to explain the formation and self-organization of patterns and structures in complex systems [17]), the qualitative aspects of the resulting coordination pattern of movement behaviour can be successfully described and modelled in terms of one or a few collective variables called *order parameters* [11]. According to synergetics theory [17], the self organised in many complex systems can be understood by the order parameters apart from the structural properties of the system's components and without requiring an explicit prescription of the mechanisms underlying their interaction. Furthermore, any parameter that influences the dynamics of order parameters inducing qualitative changes in the collective behaviour is called *control parameter* [11]. Scaling a control parameter may lead the original coordination pattern to lose stability and switch to a different coordination mode that is now stable. This abrupt switching between different coordination patterns, in the sense

of losing stability, is the key to identify the order and control parameters that define coordination states and their dynamics. The synergetics theory [17] also suggests that the collective behaviour of the complex system on a macroscopic scale may exhibit low-dimensional dynamics close to the points where the transition occurs. Therefore, studying the stability and bifurcations of movement coordination models is essential to the dynamical systems approach to movement coordination [3, 18].

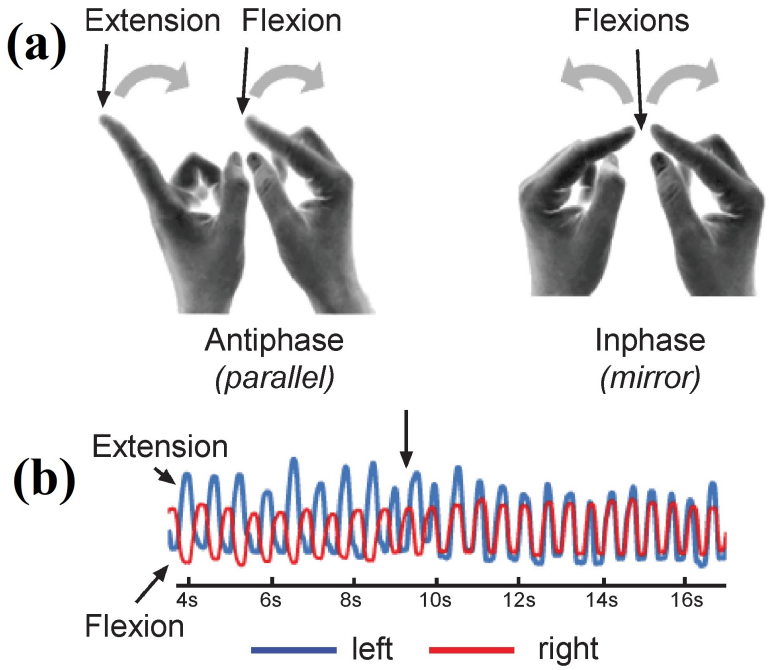

Figure 1.1: Transition of coordination patterns in bimanual movements. Panel (**a**) illustrates two experimental conditions for fingers movement (parallel and mirror) corresponding to the in-phase and anti-phase coordination patterns; panel (**b**) shows a representative time series of the finger movements. In trials initiated in the anti-phase pattern and as the pace rate increases, a spontaneous switching of the movement coordination form anti-phase to in-phase pattern occurs after exceeding a certain critical frequency rate of the movement (identified with a vertical arrow). No similar pattern transition occurs for the trials initiated in the in-phase pattern. The figure is adapted from [3].

In human motor behaviour, a basic phenomenon of changing coordination pattern is the involuntary switching from anti-symmetrical to symmetrical coordination mode that has been observed in bimanual fingers movement [19], then demonstrated in a wide range of movement coordination contexts [11, 20–29]. When both human index fingers are moved in an anti-phase coordination pattern (one flexes while the

other extends) then increasing movement frequency results in a spontaneous switching of the movement pattern to in-phase (both flex and extend at the same time) after exceeding a certain critical frequency rate (see Figure 1.1). No similar pattern transition occurs if the initial movement was in-phase.

Inspired by the Synergetics theory [30], Haken *et al.* (1985) developed in their landmark work a theoretical model for frequency-induced transitions in bimanual movement widely referred to in the literature as the Haken-Kelso-Bunz (or HKB) model [8, 29]. The aim of the model is to capture the following experimentally observed phenomena [31]:

1) For low frequency, both in-phase and anti-phase movement can be performed;

2) As the frequency of movement increases and crosses a certain rate; subjects spontaneously switch from anti-phase to in-phase;

3) For high frequency, only in-phase movement can be performed.

To describe the transition in the coordination pattern of two moving effectors (fingers, joints, limbs, ... etc.), Haken *et al.* (1985) proposed a model of two coupled oscillators describing the kinematic properties of the two effectors. In the following, we present a brief description of the single HKB oscillator, in addition to the coupling of the full HKB system. We also discuss the transition of movement coordination pattern on the level of relative phase of the effectors.

1.1.1.1 The HKB single oscillator

Inspired by the Synergetics theory [17], the HKB model was proposed to describe the change of patterns in rhythmic movements by considering the spatial and temporal properties (order parameters) of the movement apart from the underlying physiological properties of the effectors [3, 8]. Modelling rhythmic movements requires a dynamic that supports existence of periodic regimes. Therefore, the internal dynamics of rhythmic movements can be modeled by an autonomous second order differential equation. To this end, Haken *et al.* (1985) [8] suggested a combination of two well-known nonlinear oscillators, namely the Van-der-Pol and Rayleigh oscillators, to form the hybrid oscillator:

$$\ddot{x} + \omega^2 x - \gamma \dot{x} + \alpha x^2 \dot{x} + \beta \dot{x}^3 = 0 \tag{1.1}$$

where $x(t)$ and $\dot{x}(t)$ denote, respectively, the effector position and velocity (the internal variables), where the dot notation indicates time derivatives. in the view of the Synergetics theory, movement pattern described by the order parameters (the internal variables x and $\dot{x}$) can be changed by a control parameter (oscillation frequency controlled by the time dependent parameter ω). The typical experimental setup for this movement class is an individual performing rhythmic movements with their effector(s) in a frequency that follows a pacing metronome [6, 29].

Notice that all the terms of the HKB single oscillators are odd, which guarantees the odd symmetry of the internal variables that is required to capture the symmetry of the flexion and extension phase of the movement. The averaged oscillation amplitude (r) of the proposed HKB hybrid oscillator (1.1) has been shown [6, 8] to have the form

$$r = \sqrt{\frac{4\gamma}{\alpha + 3\beta\,\omega^2}} \tag{1.2}$$

exhibiting a bounded and monotonic decrease as the frequency parameter ω increases [6, 8] (see section 2.1.2). This inverse relation between movement frequency and amplitude has been experimentally validated and observed in relevant movement tasks [6, 12].

1.1.1.2 The coupled HKB oscillators

The full HKB model proposed by Haken *et al.* (1985)[8] is a system of two coupled hybrid oscillators of the form:

$$\begin{aligned} \ddot{x_1} + \omega^2 x_1 - \gamma \dot{x}_1 + \alpha x_1^2 \dot{x}_1 + \beta \dot{x}_1^3 &= I(x_1, \dot{x}_1, x_2, \dot{x}_2) \\ \ddot{x}_2 + \omega^2 x_2 - \gamma \dot{x}_2 + \alpha x_2^2 \dot{x}_2 + \beta \dot{x}_2^3 &= I(x_2, \dot{x}_2, x_1, \dot{x}_1). \end{aligned} \tag{1.3}$$

The main challenge in the proposed system was the derivation of a suitable coupling function I that leads to dynamics supporting the transition of coordination pattern. The coupling function needs to have odd symmetry (*i.e.* all terms are odd) to guarantee the symmetry between the left and right effectors.

Haken *et al.* (1985) proposed two formulations of the coupling function I: the first version is a function of the differences of the effectors positions and velocities given [8] by

$$F_{i,j} = (\dot{x}_i - \dot{x}_j)\big(a + b(x_i - x_j)^2\big) \tag{1.4}$$

The second proposed coupling function depends on the differences of the effectors positions at previous times τ and is given [8] by

$$J_{i,j} = \int_{-\infty}^{t} \big[c(x_{i\tau} - x_{j\tau}) + d(x_{i\tau} - x_{j\tau})^3\big] e^{-\sigma(t-\tau)} d\tau \tag{1.5}$$

The integration (1.5) is an averaging of the difference of the effectors positions over the past time. The parameter σ is proposed to facilitate the calculation of the approximation and is assumed to be sufficiently small $\sigma \ll \omega$ [8].

1.1.1.3 The potential of the relative phase

The next modelling step in Haken *et al.*'s work was to show that the two coupling functions (1.4) and (1.5) lead to the desired frequency-induced transition of coordination pattern. To this end, Haken *et al.* (1985) applied two approximation principles, namely the slowly varying amplitude approximation (neglecting the time derivative of the amplitude compared to the amplitude) and the rotating wave approximation (neglecting the terms of higher frequencies compared to the low frequency terms) [8], to demonstrate that the relative phase dynamics of two HKB oscillators coupled

by the functions (1.4) and (1.5) can be expressed [8, 29], respectively, by

$$\dot{\phi} = (a + 2br^2)\sin(\phi) - br^2\sin(2\phi) \tag{1.6}$$

$$\dot{\phi}_\tau = -\frac{1}{\omega^2}\left[(c + 6dr^2)\sin(\phi_\tau) - 3dr^2\sin(2\phi_\tau)\right] \tag{1.7}$$

where ϕ and ϕ_τ represent the relative phase of the oscillators coupled by the functions (1.4) and (1.5), respectively, r represents the amplitude of the oscillation, and a, b, c and d are coupling parameters. Both the equations (1.4) and (1.5) can be written in the form:

$$\dot{\phi} = f(\phi) = -A\sin(\phi) - 2B\sin(2\phi) \tag{1.8}$$

where A and B are constants. The potential of equation (1.8) is determined by

$$\dot{\phi} = -\frac{\partial V(\phi)}{\partial \phi} \tag{1.9}$$

and has the explicit form

$$V(\phi) = -A\cos(\phi) - B\cos(2\phi) \tag{1.10}$$

Figure 1.2 illustrates the potential function defined by (1.10). It can be noticed that depending on the ratio $\frac{B}{A}$, the potential function curve either has three minima at $\phi = 0,\ \pm\pi$ for $0°$ and $\pm 180°$, or only one minimum at $\phi = 0$, corresponding to the stable states of the relative phase. The critical ratio associated with the loss of anti-phase stability is $\frac{B}{A} = 0.25$ [3, 8]. Computing this ratio for the detailed potential functions of the equations (1.6) and (1.7) leads to the critical amplitude of the pattern transition given [18, 29] by:

$$r_0 = \sqrt{\frac{-a}{4b}} \tag{1.11}$$

$$r_{\tau 0} = \sqrt{\frac{-c}{12d}} \tag{1.12}$$

provided that $a, c < 0$, where r_0 and $r_{\tau 0}$ represent the critical amplitudes below which

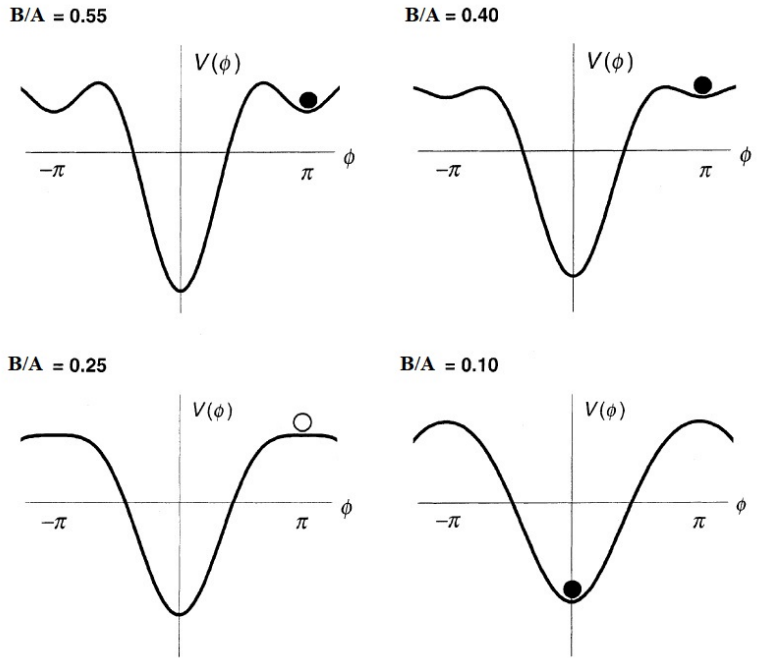

Figure 1.2: Potential of relative phase. The potential $V(\phi)$ defined by (1.10). *Black/white ball* corresponds to stable/unstable coordination pattern. The stability of the anti-phase state $\phi = \pm\pi$ is controlled by the ratio $\frac{B}{A}$. The figure is adapted from [3].

the anti-phase relative phase of two oscillators coupled, respectively, by the functions (1.4) and (1.5) loses stability *i.e.* the anti-phase periodic solution is unstable for $r < r_0$.

Considering the relative phase ϕ and movement frequency ω, respectively, as the order and control parameters of the movement coordination [8], and building on the inverse amplitude-frequency relation (1.2) associated with the hybrid oscillator [8], Haken *et al.* (1985) predicted that the frequency-induced loss of anti-phase stability is mediated by the inverse relation between movement frequency and amplitude [18, 29]. As the movement frequency increases, the amplitude of oscillation decreases until crossing the critical amplitude, then a loss of anti-phase stability occurs leading to the transition from anti-phase to in-phase coordination pattern [8]. Later on, the prediction of an inverse relation between movement frequency and amplitude has been examined and observed experimentally in unimanual and bimanual rhythmic movements [6, 12] at least for unrestricted movement amplitude tasks [29].

While in the time-derivative coupling function (1.4) the frequency-induced transitions of coordination pattern is fully mediated by the amplitude-frequency relation [29], the time-delays coupling function (1.5) shows an additional inverse dependence of relative phase stability (determined by (1.7)) on movement frequency ω [18, 29]. Due to this additional dependence on movement frequency, pattern stability of system (1.7) becomes too small [29] to resist the stochastic fluctuations observed experimentally [32].

On the other hand, the time-derivative coupling function (1.4) is more commonly used and cited in the movement coordination literature [6, 7, 14, 33–37]. Moreover, perceptual time delay has been recently [16] incorporated into the time-derivative coupling version to be in the form:

$$F_{i,j} = (\dot{x_i} - \dot{x}_{j\tau}) \left(a + b(x_i - x_{j\tau})^2\right) \tag{1.13}$$

In our work, we will consider the HKB model with the coupling version (1.13), which we refer to as the *phenomenologically motivated coupling*.

1.1.2 The Jirsa-Kelso excitator model

Discrete and rhythmic movements can be distinguished based on the directional field of their phase flow [2]. This can be confirmed experimentally by extracting fixed point dynamics from discrete movements as well as limit cycle dynamics from rhythmic movements [38, 39]. In their novel work, Jirsa and Kelso [9] defined a universal class of excitatory system that admits limit cycle and fixed-points dynamical regimes reproducing rhythmic and discrete movement, respectively [15]. It also provides novel predictions, through threshold properties, regarding phenomena such as false starts that have been confirmed experimentally [9, 13].

1.1.2.1 The single Jirsa-Kelso excitator

Jirsa and Kelso [9, 13] suggested a specific formulation of their system, the so-called excitator. The proposed formulation is a 2D system of the form:

$$\begin{aligned} \dot{u} &= v \\ \dot{v} &= \left(-\frac{b}{3}u^3 + (b-1)u + a + I\right) - \left(u^2 - 1 + \frac{b}{c^2}\right)cv \end{aligned} \tag{1.14}$$

Here, the internal variables u and v are interpreted as the position and the velocity of the moving effector, respectively, a and b are intrinsic model parameters, c is a constant controlling the time scale and I is an external stimulus input (time-dependent parameter). Typical experimental setup for tis model is an individual performing rhythmic, or discrete movement [from a point to itself (monostable) or form a point to another (bistable)] following external stimulus (*e.g.* metronome). For the discrete movement, the strength of the external stimulus determines whether the performed movement is just a perturbation in a small neighborhood of the equilibrium (also known as false starting) or whether it is a full movement in a large loop to the same point (in the monostable case) or to the other point (in a bistable case) [9, 13].

Furthermore, Jirsa and Kelso [9] showed that the proposed formulation (1.14) can be transformed into the well-known FitzHugh-Nagumo system [40] given by

$$\begin{aligned} \dot{x} &= \left(y + x - \frac{x^3}{3}\right)c \\ \dot{y} &= -\left(x - a + by - I\right)/c \end{aligned} \tag{1.15}$$

using the transformation

$$\begin{aligned} u &= x \\ v &= \left(y + x - \frac{x^3}{3}\right)c \end{aligned} \tag{1.16}$$

Since the transformation (1.16) is homeomorphism (for $c \neq 0$), the intrinsic dynamics of both systems (1.14) and (1.15) are equivalent [9]. This equivalence of the phase flow topology is important since a wide range of interesting 2D dynamical behaviour, e.g. threshold properties, relaxation oscillation and canards, exhibited

by the excitator system can be understood in light of the excitatory properties and fast-slow dynamics of FitzHugh-Nagumo model, that has been extensively studied [41–43].

1.1.2.2 The coupled excitators

Motivated by neurological observations, Banerjee and Jirsa (2007) [44] proposed a system of two coupled excitators to describe the dynamics of rhythmic bimanual coordination using a version of coupling function that incorporates time delays and allows for various degrees of neural crosstalk between two moving effectors. The proposed coupling function is given [44] by:

$$G(x_i, x_j, x_{i\tau}, x_{j\tau}) = \varepsilon \left((x_i - (1-r)x_{i\tau} - rx_{j\tau}) - \frac{1}{3}(x_i - (1-r)x_{i\tau} - rx_{j\tau})^3 \right) \tag{1.17}$$

where r is a constant representing the degree of crosstalk in the coupling and ε is the strength of the coupling (could be small or large). Furthermore, to describe the intrinsic dynamics of the two effectors, Banerjee and Jirsa (2007) used two FitzHugh-Nagumo systems (which have dynamics that are equivalent to the JK-excitators). The proposed full model takes the form:

$$\begin{aligned} \dot{x}_i &= c \left[y_i + x_i - R_0^{-2} \frac{x_i^3}{3} + G(x_i, x_{3-i}) \right] \\ \dot{y}_i &= -\left(x_i - a\right)/c \end{aligned} \tag{1.18}$$

where $i = 1, 2$, with the parameters: c controlling the time scale, a corresponding to the abscissa of the fixed point and R_0 approximating the amplitude of oscillation [see [44] Appendix A]. The two systems are decoupled for $r = 0$. The model shows consistency with related experimental observations of the influence of neural connectivity on bimanual coordination [44] and gives explanations of the decreased stability of the anti-phase mode of coordination in split brain patients (patients suffering from epilepsy whose corpus callosum has been surgically sectioned [44, 45]). Such patients tend to switch into in-phase mode even if they are instructed to maintain some other coordination phase patterns [45].

1.2 Previous work

Since the HKB model was presented in 1985 [8], several articles have studied the dynamics of the model including the single hybrid oscillator [6, 46] the full system of two coupled oscillators [46, 47] in addition to the reduced dynamics of the relative phase [29, 48] proposed to describe the anti-phase to in-phase transition in the HKB model [8].

An approximation of the limit cycle amplitude in the single HKB oscillator has been derived using slowly varying amplitudes, rotating wave approximations and averaging method [6, 8, 48]. The approximation undergoes an inverse amplitude-frequency relation that has been validated in empirical studies of unconstrained movement amplitude tasks (where the individual was asked to perform a fixed amplitude rhythmic movement) [6, 12, 29]. Using this relation, the parameters of the HKB oscillator were fitted to the experimental data and had been adopted in recent studies [6, 14]. Furthermore, the amplitude-frequency relation was also important to explain phase transition in the full model of coupled oscillators via properties of the reduced relative phase system [8, 29].

In addition, the local bifurcation and global transition in the dynamics of steady state and periodic attractors of the single HKB oscillator have been systematically analysed in the space spanned by the position and velocity of the oscillator for general parameter setting [46]. To our knowledge, however, a numerical continuation of the periodic orbits and their stability for the experimentally fitted parameter setting has not been explicitly presented in previous work. Such numerical analysis does not only investigate the suitability of the dynamics of the model to further analytical and experimental studies in the narrow range of fitted parameters but also allow for comparing the actual computed solutions from the model to the approximating oscillatory solutions and to the experimental data.

The dynamics of the relative phase proposed in the HKB work [8] and related modified versions have been studied considering the bifurcations leading to transitions between anti-phase and in-phase coordination states [see *e.g.* [49]]. Furthermore, the influence of the frequency and the coupling parameters on the stability of solutions in phase-approximation dynamics of the HKB model and the ability to switch between the multiple stable states of the system was investigated in [48].

The bifurcation analysis of the full HKB model (the two coupled oscillators) in four-dimensional state space was systematically performed considering all model parameters as well as general coupling strengths [46]. Recently, perceptual time delay has been incorporated into the HKB coupling [16] in the form (1.13), which we refer to as the phenomenologically motivated coupling. Bifurcation analysis has been performed to explore the influence of the time delay on increasing the degree of bistability of the in-phase and anti-phase periodic solutions [47]. The parameter settings of the intrinsic dynamics in the latter analysis was fixed to the values estimated from experimental data [6]. However, the later numerical analysis revealed stability and amplitude properties of the anti-phase periodic solutions which are not in a good agreement with the phase switching and amplitude drop phenomena observed in the experiments. Therefore, finding an alternative coupling that well represents the frequency-induced transition from anti-phase to in-phase pattern, and consistently exhibits an inverse amplitude-frequency relation, will have a significant implication on the HKB model [8] applications.

The topological properties of the dynamics in the Jersa-Kelso excitator (JKE) [9] can be inferred from the equivalent FitzHugh-Nagumo (FHN) model [40], which has been fully analysed in the literature [41]. However, there are still some interesting dynamical properties that are distinct between the two models. Canard phenomenon is an example of such differences. Although, canard solutions have been studied and well understood in the FitzHugh-Nagumo, and more general systems that involve folded singularity in an N-shaped critical manifold, using different approaches, *e.g.* blow-up technique [50] and curves of inflection points [51]. However, the applicability of these approaches to the JKE is not straightforward. Furthermore, since the homomorphism transformation between the FHN and JKE models depends on the timescale parameter ε, different scenarios for the organising mechanism of singular canard occur in the singular case. Therefore, understanding the canard phenomena in the JKE requires exploring alternatives to the classical approaches applied to the FHN model.

In addition, a study of the stability of in-phase and anti-phase solutions in a model of two excitators (represented by the equivalent FHN dynamics) coupled by (1.17) has been presented in [44]. This study discussed possible mechanisms that lead to change of linear stability and switch from one pattern of coordination to

another. The suggested mechanisms are induced by the degree of crosstalk r and the time delay τ involved in the crosstalk between the two effectors. Furthermore, the article studied the contribution of the movement amplitude, approximated by the parameter R_0, on the stability boundaries which can be related to the influence of movement frequency, following the assumption of frequency-amplitude interdependence [6]. However, a systematic study of the possible solution the model might support and their stability will demonstrate the dynamical properties of the actual (non-approximated) solutions and their consistency with the related experimental results.

1.3 Aims and outline of the thesis

In this thesis, we aim to answer open questions outlined in the previous section. We perform dynamical systems analysis to explore unknown aspects of the dynamics supported by the HKB and JKE models. The outline of this thesis is as follows:

The second chapter discusses the dynamics of the single oscillator in the HKB and JKE models. First, we present a dynamical systems analysis of the steady states and periodic solutions of the HKB hybrid oscillator for the fitted and general parameter setting. We also investigate the averaged amplitude-phase dynamics of the system and compare the approximated solutions to those computed numerically from the HKB oscillator. Secondly, we discuss the equivalence of the JKE system to the FHN model by comparing the bifurcation diagrams of the models and through projecting the dynamics of the two systems on a 3D hypersurface. In addition, we present a scaling of the JKE system that allows for an explicit separation of time-scale. Moreover, we propose an approximated version of the JKE system and present a comparison of the bifurcations in the two versions of the model.

The third chapter is dedicated to studying the canard phenomena in the JKE model. First, canard solutions of the JKE are computed and compared to the corresponding solutions in the FHN model. We, then, discuss the applicability of the parameter-estimation and inflection-points approaches to characterise the existence of canard solutions and identify the maximal canard. Furthermore, we examine alternative approaches to determine the maximal canards in the JKE that require solving multi-segment BVPs, *e.g.* the orbit of maximal following time and

the orbit through the non-hyperbolicity. Moreover, we use the blow-up technique and Poincaré sphere projection to analyse the singular canards, and explain the returning mechanism via nonhyperbolic equilibria at infinity. Such behaviour is not found in the classical fold singularity canards of FHN model.

In the fourth chapter, a systematic dynamical systems analysis of a system of two HKB oscillators coupled by the neurologically motivated function (1.17) is presented. We compare the influence of the coupling on the stability and amplitude properties of the in-phase and anti-phase solution. We, then, investigate the influence of time-delay and coupling parameters on producing the desired frequency-induced transition of coordination pattern stability and drop of amplitude properties observed in the related experimental studies [6, 19].

In chapter five, we discuss our findings and highlight their contribution to the movement coordination field. Finally, we draw conclusions and outline some future directions in the final chapter of the thesis.

Chapter 2

Dynamical systems analysis of the HKB and JKE single oscillators

In this chapter, we explore the dynamics of the single Haken-Kelso-Bunz (HKB) oscillator and the Jirsa-Kelso excitator (JKE). Our aim is to characterise the different types and stability of the model solutions and understand their dependence on the models' parameters.

In the first section, we consider the system of HKB single oscillator. We first theoretically analyse the stability of the steady state. Then, we present numerical bifurcation analysis of the steady and periodic regimes. Furthermore, we cast the HKB single oscillator into polar coordinates and investigate the averaged amplitude-phase dynamics of the system. Moreover, we compare the approximated solutions, obtained from the averaged amplitude-phase system, to the actual solutions computed numerically from the HKB oscillator for the physically relevant parameter setting.

In the second section, we analyse the dynamics of the JKE model demonstrating the wide variety of different dynamics that the model supports comparing to the HKB system. We discuss the equivalence of dynamics in the JKE and FHN models by demonstrating the smoothness of the transformation for the non-singular case. Furthermore, we illustrate this equivalence by projecting the phase spaces of the two systems on a 3D hypersurface, as well as, by comparing the bifurcation diagrams of the two systems. In addition, we present a rescaled version of the JKE model that exhibits an explicit separation of time-scales and allows for a direct comparison

of the slow and fast flow in the JKE to that in the FHN model. Moreover, we propose an approximated version of the JKE system, then, compare and discuss the bifurcation in the two models.

We also discuss the implications of our results for future applications of the HKB and JKE models.

2.1 The HKB oscillator

Recall the second-order differential equation of the HKB oscillator

$$\ddot{x} = -\dot{x}\left(\alpha x^2 + \beta \dot{x}^2 - \gamma\right) - \omega^2 x \tag{2.1}$$

The equation (2.1) can be written as a system of differential equations of the first order:

$$\begin{aligned} \dot{x} &= y && = f(x,y) \\ \dot{y} &= -\omega^2 x - y\left(\alpha x^2 + \beta y^2 - \gamma\right) && = g(x,y) \end{aligned} \tag{2.2}$$

2.1.1 Bifurcation analysis

In this part, we consider the bifurcations of the steady state and periodic solutions in the single HKB oscillator system (2.2). The stability of the steady state and the bifurcations leading to the appearance and disappearance of periodic solutions in the HKB oscillator have been analysed in [46]. Here we review these bifurcations, present the corresponding two-parameter continuations for representative parameter settings, and then discuss and classify the different regions in the parameter space according to the number and stability of solutions the HKB single oscillator supports.

2.1.1.1 Stability of the trivial steady state

The trivial equilibrium point $(x, y) = (0, 0)$ is the only steady state that the HKB system (2.2) has for $\omega \neq 0$. For the degenerate case $\omega = 0$, however, the steady state consists of a family of infinite non-isolated fixed points given by $\{(x, y)|y = 0\}$. This is true due to the fact that all the constant functions $x(t) = x_0$ are solutions of the second-order equation (2.1) for $\omega = 0$. The linearization of the system at the trivial equilibrium $(x, y) = (0, 0)$ for the non-degenerate case $\omega \neq 0$ is given by the

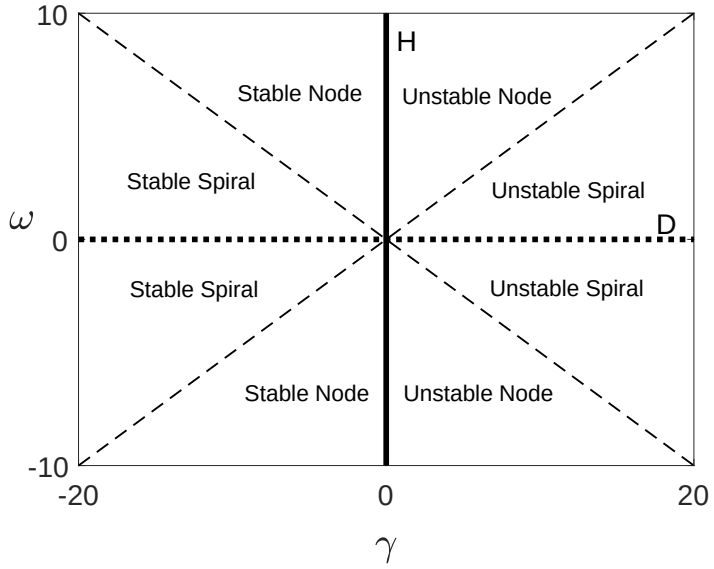

Figure 2.1: Types of steady state of the HKB oscillator in (γ, ω)-plane. *Solid line* indicates the locus of Hopf bifurcation (H); *dotted line* corresponds to the degenerate case (D) of a family of infinite non-isolated fixed points; *dashed lines* represent the boundary between node and spiral (focus) types of equilibrium.

Jacobian matrix

$$J_{(0,0)} = \begin{bmatrix} 0 & 1 \\ -\omega^2 & \gamma \end{bmatrix} \tag{2.3}$$

which has the eigenvalues:

$$\lambda_{\pm} = \frac{\gamma \pm \sqrt{\gamma^2 - 4\omega^2}}{2} \tag{2.4}$$

For $|\gamma| \geq 2\omega$, the eigenvalues are a pair of non-zero real numbers. The equilibrium in this case is a stable (unstable) node if $\gamma < 0$ ($\gamma > 0$) [46]. However, for $|\gamma| < 2\omega$, the eigenvalues are a pair of complex-conjugate numbers that can be written as:

$$\lambda_{\pm} = \frac{\gamma \pm i\sqrt{4\omega^2 - \gamma^2}}{2} \tag{2.5}$$

Thus, the equilibrium is a stable (unstable) spiral if $\gamma < 0$ ($\gamma > 0$) [46].

Figure 2.1 illustrates the types and stability of the trivial steady state in the (γ, ω)-parameter plane. Since the parameter ω is related to the natural frequency

of the oscillator (2.1) [46], we will only consider $\omega > 0$ in our analysis.

2.1.1.2 Existence of periodic solutions

Next, we consider the bifurcations that lead to the appearance or disappearance of periodic solutions of system (2.2). The pair of complex eigenvalues (2.5) becomes purely imaginary for $\gamma = 0$ corresponding to Hopf bifurcation which gives rise to the periodic solution. The non-degeneracy conditions for this bifurcation are:

1. $\left.\frac{\partial \Re(\lambda)}{\partial \gamma}\right|_{\gamma=0} \neq 0$
2. $\ell_1(0) \neq 0$

where $\ell_1(0)$ is the first Lyapunov coefficient at $\gamma = 0$ [52].

From (2.5), we have

$$\left.\frac{\partial \Re(\lambda)}{\partial \gamma}\right|_{\gamma=0} = \frac{1}{2} \neq 0 \tag{2.6}$$

To compute the first Lyapunov coefficient, we adopt the formula in [53]. For the planer system:

$$\begin{aligned} \dot{x} &= f(x, y) \\ \dot{y} &= g(x, y) \end{aligned} \tag{2.7}$$

that has an equilibrium $(x, y) = (0, 0)$ of Jacobian:

$$J = \begin{bmatrix} f_x(0,0) & f_y(0,0) \\ g_x(0,0) & g_y(0,0) \end{bmatrix} = \begin{bmatrix} a & b \\ c & d \end{bmatrix} \tag{2.8}$$

such that $\sigma := a + d = 0$ and $\Delta := ad - bc > 0$, the first Lyapunov coefficient can be defined by [53]:

$$\begin{aligned} \ell_1(0) := \frac{b}{16\Delta^2} \{ & \Delta \left[b(f_{xxx} + g_{xxy}) + 2d(f_{xxy} + g_{xyy}) - c(f_{xyy} + g_{yyy}) \right] \\ & - bd(f_{xx}^2 - f_{xx}g_{xy} - f_{xy}g_{xx} - g_{xx}g_{yy} - 2g_{xy}^2) \\ & - cd(g_{yy}^2 - g_{yy}f_{xy} - g_{xy}f_{yy} - f_{yy}f_{xx} - 2f_{xy}^2) \\ & + b^2(f_{xx}g_{xx} + g_{xx}g_{xy}) - c^2(f_{yy}g_{yy} + f_{xy}f_{yy}) \\ & - (\Delta + 3d^2)(f_{xx}f_{xy} - g_{xy}g_{yy}) \} \end{aligned} \tag{2.9}$$

Other scaled versions of the first Lyapunov coefficient can also be found in the literature, see *e.g.* [52, 54–56].

Consider the functions f and g in (2.2) and the Jacobian (2.3). Since f and g are odd, all second-order terms in (2.9) can be eliminated. Hence, we can easily show that

$$\ell_1(0) = \frac{-(\alpha + 3\beta\omega^2)}{8\omega^2} \tag{2.10}$$

For $\alpha + 3\beta\omega^2 \neq 0$ (*i.e.* $\ell_1(0) \neq 0$), the Hopf bifurcation is non-degenerate and a branch of periodic solutions, that have an opposite stability state compared to the equilibrium, bifurcates from the Hopf point as the parameter γ crosses the value $\gamma = 0$. The local range of γ along which the branch of periodic solution exists is determined by the sign of the first Lyapunov coefficient $\ell_1(0)$. If $\ell_1(0) < 0$, the branch of periodic solutions bifurcates as the parameter γ increases (*i.e.* for $\gamma > 0$) and the Hopf bifurcation is supercritical. Whereas, for $\ell_1(0) > 0$, the family of periodic orbits emanates from the Hopf point as γ decreases (*i.e.* for $\gamma < 0$) and the Hopf bifurcation is subcritical [56].

Furthermore, changing one of the parameters α, β and ω can lead to the degenerate case $\ell_1(0) = 0$ (as $\alpha + 3\beta\omega^2 = 0$), which is associated with codim 2 bifurcation called Generalized Hopf bifurcation (GHB) (also known as degenerate Hopf or Bautin bifurcation) [46, 56]. Considering the parameter planes spanned by γ and any of the parameters α, β and ω (for $\alpha\beta < 0$), the location of the Generalized Hopf lies on the curve $\gamma = 0$ corresponding to the locus of the Hopf bifurcation and splits the curve into sub- and supercritical Hopf bifurcation branches (*e.g.* GHB occurs at $\gamma = 0$, $\alpha = \pm 1.2$, $\beta = \mp 0.1$ and $\omega = 2$). Furthermore, a curve corresponding to the locus of a saddle-node (fold) bifurcation of limit cycles (where two limit cycles collide and disappear) bifurcates from the Generalized Hopf point [56].

Moreover, the regions in the parameter plane corresponding to the existence of periodic solutions are also bounded by a global bifurcation reported in [46] at which the periodic solutions of the HKB model disappear via a heteroclinic cycle at infinity.

2.1.1.3 Numerical bifurcation analysis

To understand how the bifurcations reported in [46] bound the existence regions of periodic solutions in the parameter space, we carry out bifurcation analysis using

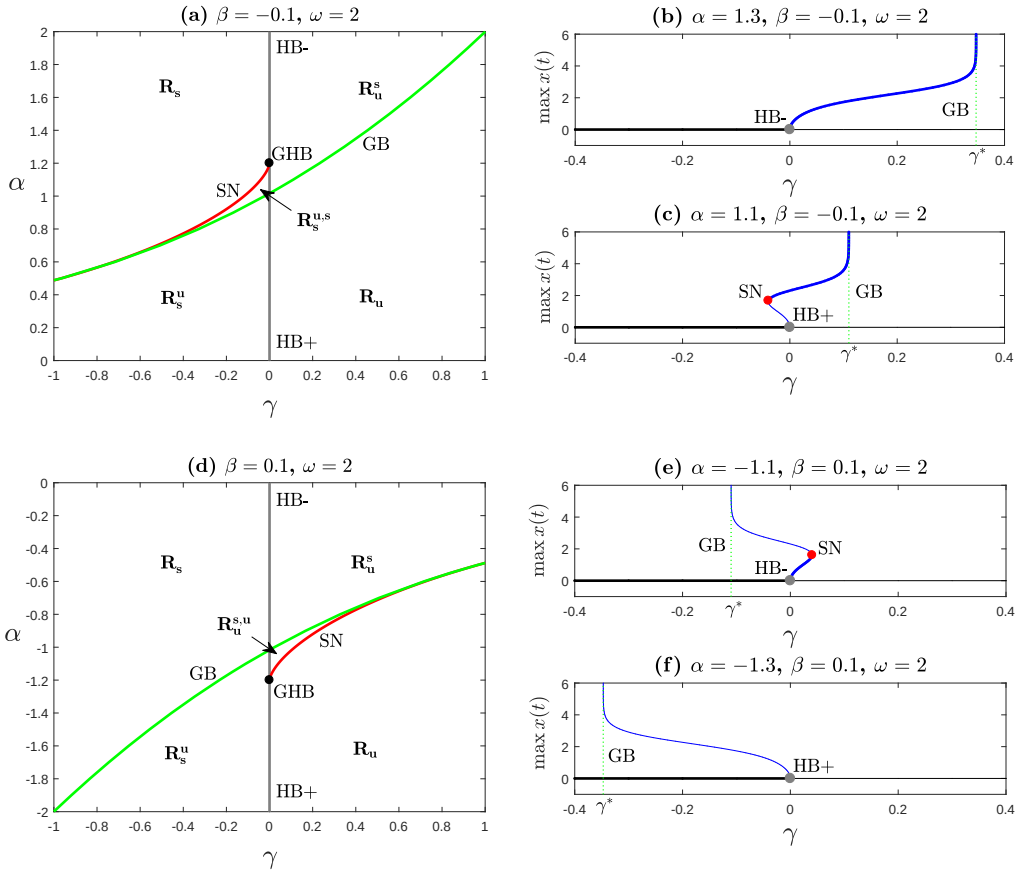

Figure 2.2: Bifurcation diagrams of HKB in γ and α. Panels **(a)** and **(d)** show two-parameter bifurcation diagrams of (2.2) in the (γ, α)-plane for $\beta = -0.1$ and $\beta = 0.1$, respectively. *Grey line* indicates the locus of Hopf bifurcation (HB-/HB+ for supercritical/subcritical); GHB for generalised Hopf bifurcation; *red line* for the locus of saddle-node bifurcation of limit cycles (SN); *green line* is corresponding to the locus of global bifurcation of periodic orbit (GB). The subscript of the regions labels R indicates the stability of steady state (s/u for stable/unstable equilibrium) and the superscript is corresponding to the number and stability of periodic solutions (blank superscript for no periodic solutions). Panels (**b-c**) and (**e-f**) illustrate one-parameter bifurcation diagrams of (2.2) ($\max x(t)$ against γ) for representative fixed values of α in panels (**a**) and (**b**), respectively. *Black/blue lines* represent the $x/\max(x)$ value of the equilibrium/periodic orbits branch, respectively, (*thick* for stable, *thin* for unstable); *grey dot* indicates Hopf bifurcation (HB-/HB+ for supercritical/subcritical); *red dot* (labeled as SN) for saddle-node bifurcation of limit cycles; *green dotted line* (labeled as GB) indicates the critical value γ^* for the event of global bifurcation of periodic orbit.

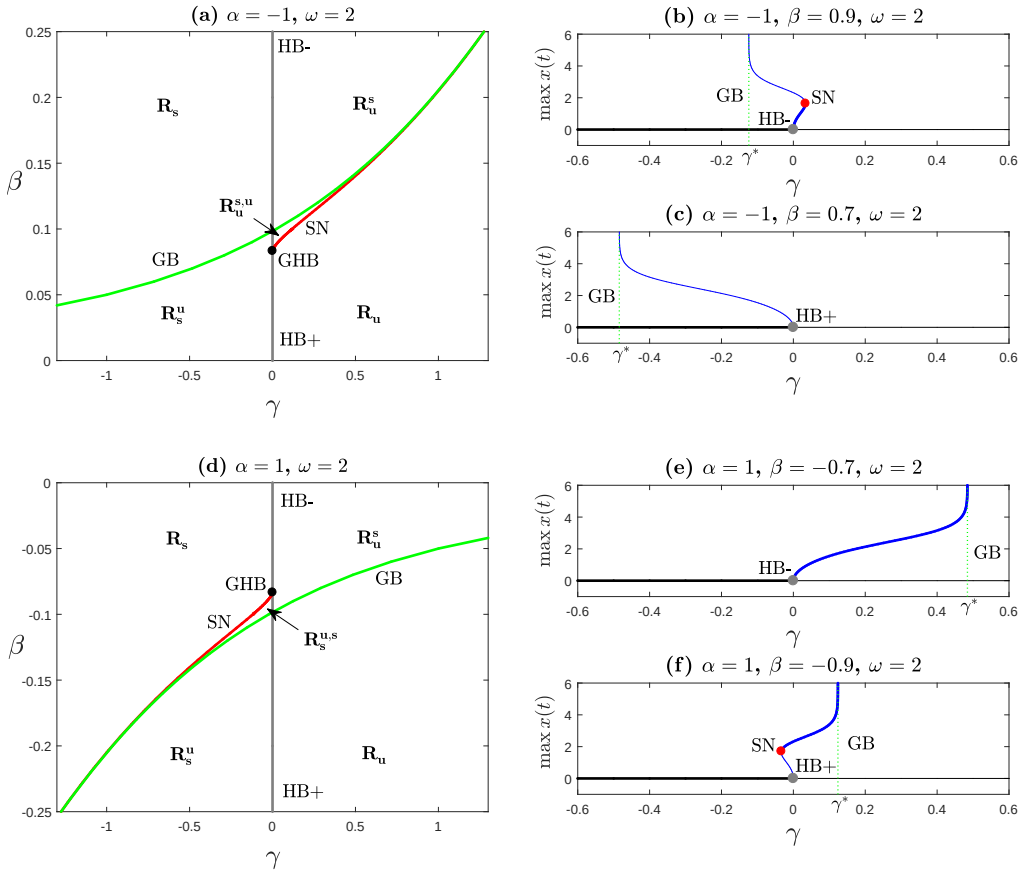

Figure 2.3: Bifurcation diagrams of HKB in γ and β. Panels **(a)** and **(d)** show two-parameter bifurcation diagrams of (2.2) in the (γ, β)-plane for $\alpha = -1$ and $\alpha = 1$, respectively. *Grey line* indicates the locus of Hopf bifurcation (HB-/HB+ for supercritical/subcritical); GHB for generalised Hopf bifurcation; *red line* for the locus of saddle-node bifurcation of limit cycles (SN); *green line* is corresponding to the locus of global bifurcation of periodic orbit (GB). The subscript of the regions labels R indicates the stability of steady state (s/u for stable/unstable equilibrium) and the superscript is corresponding to the number and stability of periodic solutions (blank superscript for no periodic solutions). Panels (**b-c**) and (**e-f**) illustrate one-parameter bifurcation diagrams of (2.2) ($\max x(t)$ against γ) for representative fixed values of α in panels (**a**) and (**b**), respectively. *Black/blue lines* represent the $x/\max(x)$ value of the equilibrium/periodic orbits branch, respectively, (*thick* for stable, *thin* for unstable); *grey dot* indicates Hopf bifurcation (HB-/HB+ for supercritical/subcritical); *red dot* (labeled as SN) for saddle-node bifurcation of limit cycles; *green dotted line* (labeled as GB) indicates the critical value γ^* for the event of global bifurcation of periodic orbit.

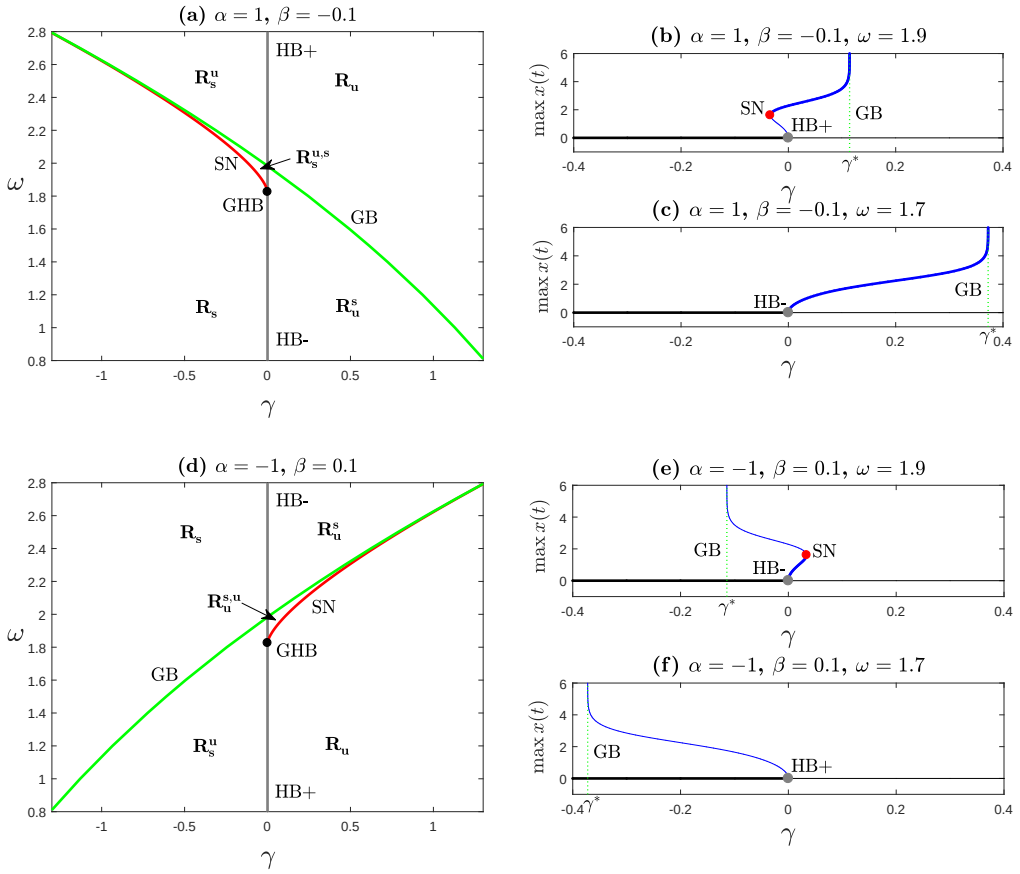

Figure 2.4: Bifurcation diagrams of HKB in γ and ω. Panels **(a)** and **(d)** show two-parameter bifurcation diagrams of (2.2) in the (γ, ω)-plane for $\alpha = 1, \beta = -0.1$ and $\alpha = -1, \beta = 0.1$, respectively. *Grey line* indicates the locus of Hopf bifurcation (HB-/HB+ for supercritical/subcritical); GHB for generalised Hopf bifurcation; *red line* for the locus of saddle-node bifurcation of limit cycles (SN); *green line* is corresponding to the locus of global bifurcation of periodic orbit (GB). The subscript of the regions labels R indicates the stability of steady state (s/u for stable/unstable equilibrium) and the superscript is corresponding to the number and stability of periodic solutions (blank superscript for no periodic solutions). Panels (**b-c**) and (**e-f**) illustrate one-parameter bifurcation diagrams of (2.2) ($\max x(t)$ against γ) for representative fixed values of α in panels (**a**) and (**b**), respectively. *Black/blue lines* represent the $x/\max(x)$ value of the equilibrium/periodic orbits branch, respectively, (*thick* for stable, *thin* for unstable); *grey dot* indicates Hopf bifurcation (HB-/HB+ for supercritical/subcritical); *red dot* (labeled as SN) for saddle-node bifurcation of limit cycles; *green dotted line* (labeled as GB) indicates the critical value γ^* for the event of global bifurcation of periodic orbit.

numerical continuation in XPPAUT [35] (which includes a frontend to the continuation and bifurcation package AUTO [57]). We set NTST = 100 and NCOL = 4, respectively, for the number of mesh intervals used for discretization and the number of Gauss collocation points per mesh interval. We also set EPSL = 10^{-9} and EPSU = 10^{-9} for the tolerances of the Newton/Chord method. We follow the loci of the reported bifurcations in the parameter-planes for various representative parameter settlings. Our results confirm the occurrence of the saddle-node of limit cycles and the global bifurcations reported in [46] robustly for wide ranges of the parameter space. The loci of the global bifurcation in the parameter planes has been computed form numerical one parameter continuation of the periodic orbits in γ for a discrete values of of the second parameters. The parameter value has been chosen corresponding to the periodic orbit of largest period and amplitude.

In our analysis we use the representative parameter values $\alpha = \pm 1$, $\beta = \mp 0.1$ and $\omega = 2$. We alternate the signs of α and β, accordingly, to ensure the existence of the saddle-node and global bifurcations of limit cycles. Our results are illustrated in Figures 2.2-2.4.

Figure 2.2 shows bifurcation diagrams of the steady state and periodic solutions of (2.2) for $\omega = 2$. Panels **(a)** and **(d)** show two-parameter bifurcation diagrams in the (γ, α)-plane for $\beta = -0.1$ and $\beta = 0.1$, respectively. Panels (**b-c**) and (**e-f**) illustrate one-parameter bifurcation diagram of (2.2) for representative choices of α from panels (**a**) and (**b**), respectively. The generalised Hopf bifurcation (labelled as GHB) is situated on the vertical grey line, corresponding the locus of Hopf bifurcation, splitting the supercritical (HB-) and subcritical (HB+) bifurcation branches. The red curve bifurcating from the generalised Hopf point (GHB) corresponds to the locus of saddle-node bifurcation of limit cycles (SN), where two periodic solutions collide and disappear (see panels (**c**) and (**e**) in Figure 2.2).

The green curve represents the locus of global bifurcation at which the periodic orbit disappears via heteroclinic cycle connecting four saddle equilibria at infinity [46]. As the parameter values change towards the curve GB in the parameter plane, the amplitude and period of the largest periodic orbit grow to infinity in an exponentially small vicinity of this curve (see panels (**c**) and (**e**) in Figure 2.2).

The different regions of the parameter plane (see Figure 2.2 (**a**) and (**d**)), are labelled as R with subscripts indicating the stability of the steady state (s/u for

stable/unstable equilibrium) and superscript corresponding to the number and stability of periodic solutions (*s/u* for one stable/unstable periodic orbit; *su* and *us* for two coexisting stable and unstable periodic orbits ordered by amplitudes; and blank superscript for regions of no periodic solutions). The same colours and labels are used in Figures 2.3 and 2.4 corresponding to the bifurcation diagrams in (γ, β)- and (γ, ω)-planes, respectively.

2.1.1.4 Implications of the bifurcation analysis for movement modelling

Although the HKB model was originally developed for bimanual movement coordination, the single HKB hybrid oscillator has been tested for tasks involves rhythmic movements of a single effector [6, 12]. Hence, identifying the regions in the parameter space where the model supports stable periodic solution regime would help in predicting what parameter settings are suitable for rhythmic movement tasks. It would also provides an insight into the intrinsic dynamics of the coupled oscillator in the full HKB model for bimanual rhythmic movement tasks.

Considering the bifurcation analysis illustrated in Figures 2.2, the regions in the parameter planes labeled as R_u^s are corresponding to the existence of stable limit cycle, for which the HKB oscillator system (2.2) supports rhythmic movement dynamics (see panels (**a**) and (**d**) in Figure 2.2).

Furthermore, bistability can be noticed in the regions labeled as $R_s^{u,s}$ in the parameter planes (see panels (**a**) and (**d**) in Figure 2.2). The bistability corresponds to the existence of two attracting regimes (stable equilibrium and stable limit cycle). The coexistence of static and periodic attracting regimes might be considered describing discrete and rhythmic movements dynamics. The boundary between the two different dynamics is represented by unstable limit cycle (of smaller amplitude) separating the basins of attraction of the two attractors in the phase space.

2.1.2 Approximation of the oscillatory solution

Approximation techniques, such as slowly varying amplitudes and rotating wave approximations, has been used to approximate the amplitude of oscillation in HKB single oscillator [6, 8]. Here, we derive the same approximation by applying the averaging method to an amplitude-phase representation of the HKB system (2.2).

Furthermore, we compare the dynamics of the resulting averaged system to that discussed earlier for the HKB system. Moreover, we discuss some interesting characteristics of the approximated amplitude relating to the experimental observations.

Consider the amplitude-phase transformation:

$$\begin{aligned} x(t) &= r(t)\ \cos(\omega t + \phi(t)) \\ y(t) &= -\,\omega\ r(t)\ \sin(\omega t + \phi(t)) \end{aligned} \tag{2.11}$$

where r and ϕ are dynamic variables corresponding to the amplitude and phase angle, respectively [6, 48]. Differentiating (2.11) leads to:

$$\begin{aligned} \dot{x} &= \dot{r}\cos(\omega t + \phi) - (\omega + \dot{\phi}) r \sin(\omega t + \phi) \\ \dot{y} &= -\,\omega \left[\dot{r}\sin(\omega t + \phi) + (\omega + \dot{\phi}) r \cos(\omega t + \phi) \right] \end{aligned} \tag{2.12}$$

Substituting (2.11) and (2.12) into system (2.2) leads to the equations:

$$\begin{aligned} &\dot{r}\cos(\omega t + \phi) - \dot{\phi}\, r \sin(\omega t + \phi) = 0 \\ &\dot{r}\sin(\omega t + \phi) + \dot{\phi}\, r \cos(\omega t + \phi) = r\ \sin(\omega t + \phi) \\ &\qquad\qquad \left(\gamma - r^2 \left[\alpha \cos^2(\omega t + \phi) + \beta\omega^2 \sin^2(\omega t + \phi)\right]\right) \end{aligned} \tag{2.13}$$

Solving (2.13) for $\dot{r}$ and $\dot{\phi}$ gives:

$$\begin{aligned} \dot{r} &= r\ \sin^2(\omega t + \phi) \left(\gamma - r^2 \left[\alpha \cos^2(\omega t + \phi) + \beta\omega^2 \sin^2(\omega t + \phi)\right]\right) \\ \dot{\phi} &= \cos(\omega t + \phi)\ \sin(\omega t + \phi) \left(\gamma - r^2 \left[\alpha \cos^2(\omega t + \phi) + \beta\omega^2 \sin^2(\omega t + \phi)\right]\right) \end{aligned} \tag{2.14}$$

After applying some related trigonometric identities, system (2.14) can be written as:

$$\begin{aligned} \dot{r} &= \frac{r}{8}\left[4\gamma - r^2(\alpha + 3\beta\omega^2)\right] - \frac{r}{2}\left[\gamma - \beta\omega^2 r^2\right]\cos(2\omega t + 2\phi) + \frac{r^3}{8}\left[\alpha - \beta\omega^2\right]\cos(4\omega t + 4\phi) \\ \dot{\phi} &= \frac{1}{4}\left[2\gamma - r^2(\alpha + \beta\omega^2)\right]\sin(2\omega t + 2\phi) - \frac{r^2}{8}\left[\alpha - \beta\omega^2\right]\sin(4\omega t + 4\phi) \end{aligned} \tag{2.15}$$

We refer to (2.15) as the *amplitude-phase representation* of the single HKB oscillator. The time dependent system (2.15) can be reduced to a non-autonomous system by

averaging over time period $T = \frac{2\pi}{\omega}$ [48, 58] leading to the system

$$\begin{aligned} \frac{d\bar{r}}{dt} =& \frac{\bar{r}}{8}\left[4\gamma - \bar{r}^2(\alpha + 3\beta\omega^2)\right] := R(\bar{r}) \\ \frac{d\bar{\phi}}{dt} =& 0 \end{aligned} \tag{2.16}$$

We refer to (2.16) as the *averaged amplitude system*. The system (2.16) admits trivial equilibrium $\bar{r} = 0$, in addition to an extra pair of equilibria of the form

$$\bar{r} = \pm\sqrt{\frac{4\gamma}{\alpha + 3\beta\,\omega^2}} \tag{2.17}$$

which exists for $\gamma(\alpha + 3\beta\omega^2) > 0$. From (2.12) and (2.17), we can define an approximation of the oscillatory solution as:

$$\begin{aligned} \tilde{x}(t) =& \quad\sqrt{\frac{4\gamma}{\alpha + 3\beta\,\omega^2}}\,\cos(\omega t + \phi_0) \\ \tilde{y}(t) =& -\omega\sqrt{\frac{4\gamma}{\alpha + 3\beta\,\omega^2}}\,\sin(\omega t + \phi_0) \end{aligned} \tag{2.18}$$

where $r_* := \sqrt{\frac{4\gamma}{\alpha+3\beta\,\omega^2}}$ is the approximated amplitude and ϕ_0 is the initial phase [6, 48]. For $\omega \gg |\gamma|$, the frequency of the periodic solution of (2.2) is, to a good approximation, just ω [6], therefore, the oscillatory function $\tilde{x}$ represents a good approximation to the periodic solution of the HKB single oscillator (2.2) [6, 8].

To relate the dynamics of the averaged amplitude system to the HKB oscillator system (2.2), notice that the trivial equilibrium $\bar{r} = 0$ represents the trivial steady state of the HKB system. The stability of $\bar{r} = 0$ is determined by the eigenvalue

$$\lambda_0 = \left.\frac{dR}{d\bar{r}}\right|_{\bar{r}=0} = \frac{\gamma}{2}$$

Hence, equivalent to the trivial steady state of (2.2), the equilibrium $\bar{r} = 0$ is stable (unstable) for $\gamma < 0$ ($\gamma > 0$), respectively. For $\gamma = 0$, the averaged amplitude system (2.16) undergoes pitchfork bifurcation with non-degeneracy condition $\sigma := -\frac{(\alpha+3\beta\,\omega^2)}{8} \neq 0$ [52]. As the parameter γ changes near $\gamma = 0$, two branches of extra equilibria, described by (2.17), emanate from the pitchfork bifurcation point

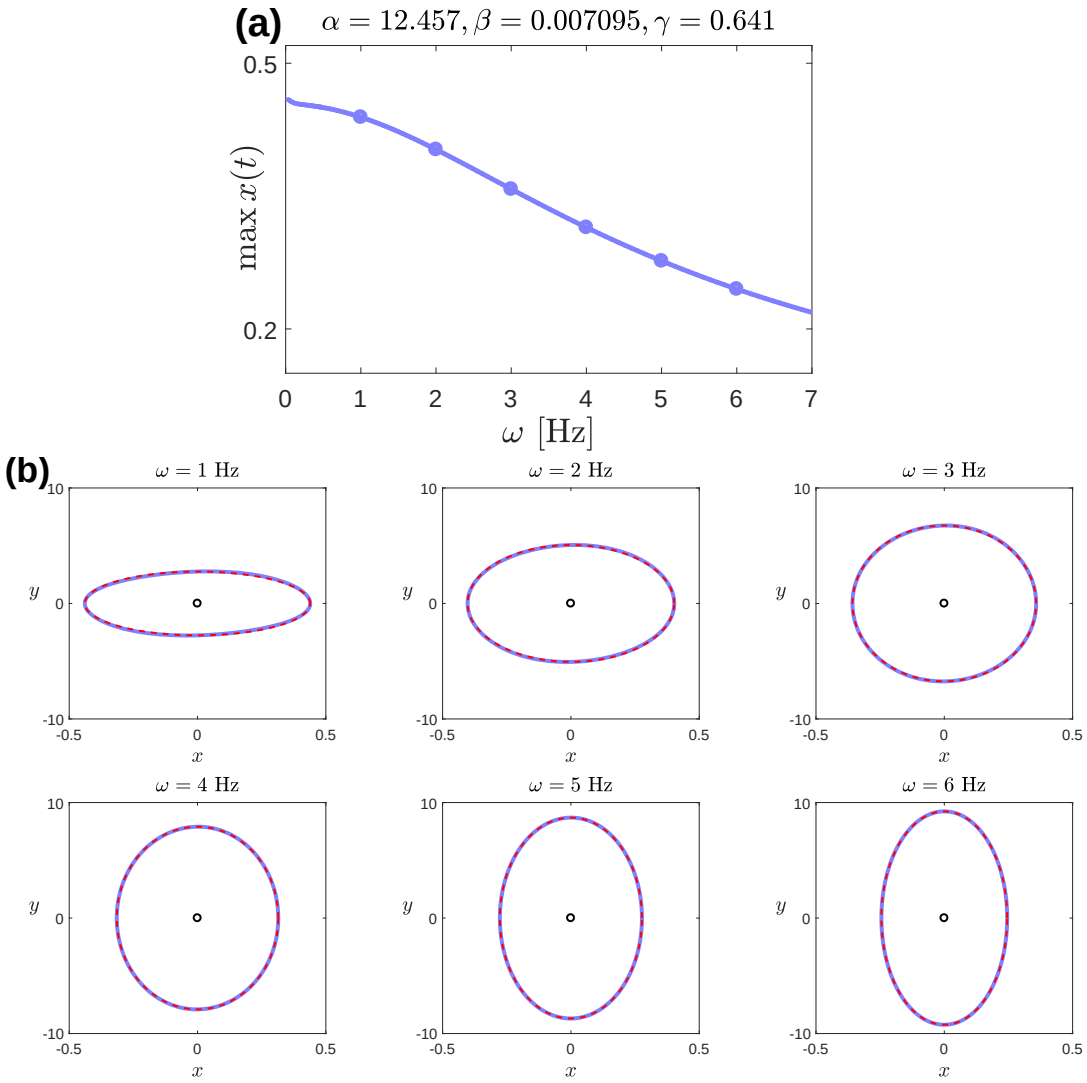

Figure 2.5: The limit cycle of the single HKB oscillator for fitted parameter values. Panel (**a**); numerical continuation of the stable periodic solution of system (2.2) in ω (plotted in blue line) for the parameter values fitted to experimental data (see [6]). Panel (**b**); phase space of system (2.2) for the selected values $\omega = 1, 2, \ldots, 6$Hz. *Blue solid line* for the stable limit cycle (corresponding to the blue dots in panel **a**)), *red dashed line* for the approximated oscillatory solution (2.18), and *black circle* for the unstable trivial equilibrium. The figure shows the drop in the amplitude of periodic solution as the frequency parameter ω increases. It also illustrates how well the solution of averaged system (2.16) approximates the limit cycle of the single HKB oscillator (2.2) for the fitted parameter setting.

$(\bar{r}, \gamma) = (0, 0)$. The pair of extra equilibria correspond to a periodic solution of (2.2). The sign of σ $(= \ell_1(0)\,\omega^2)$ determines the direction toward which the extra branches bifurcate. Therefore, equivalent to the Hopf bifurcation of the trivial steady state in (2.2), the pitchfork bifurcation is supercritical (subcritical) if $\sigma < 0$ $(\sigma > 0)$, respectively. To show that the stability state of the extra branches $\bar{r} = \mp r_*$ is an opposite to that of the trivial equilibrium $\bar{r} = 0$, observe the sign of the eigenvalues

$$\lambda_{\pm} = \frac{dR}{d\bar{r}}\bigg|_{\bar{r}=\pm r_*} = \frac{\gamma}{2} - \frac{3}{8} r_*^2(\alpha + 3\beta\omega^2) = -\gamma$$

Hence the extra pair of equililbria, corresponding to the periodic solution of (2.2), are stable (unstable) if they exist for $\gamma < 0$ $(\gamma > 0)$, respectively.

Moreover, the non trivial amplitude described by (2.17) demonstrates an important relation between amplitude and frequency of the oscillation in (2.2) (represented by $\bar{r}$ and ω, respectively). As the natural frequency parameter ω increases, the amplitude $\bar{r}$ decreases hyperbolically with finite intercept at $\omega = 0$ [6]. This amplitude-frequency relation is consistent with experimental observations reported in related human movement studies [6, 12, 29]. The studies associate a drop in the amplitude of movement with increasing the movement frequency. Therefore, the amplitude-frequency relation was a key motivation to adopt the hybrid oscillator (2.1) in the HKB model [6, 8].

The amplitude-frequency relation (2.17) can also be used to determine best-fit values for the parameters α, β and γ based on experimental data of moving effector with different frequencies. The parameter values $\alpha = 12.457$, $\beta = 0.007095$ and $\gamma = 0.641$ has been estimated directly from experimental data for hand movements [6] and used later in related works [14, 47, 59].

To illustrate the drop in amplitude of the periodic solution of HKB system as the frequency increases, we perform numerical continuation of the periodic orbit of (2.2) in ω for the fitted parameter values mentioned above [see Figure 2.5 **(a)**]. Furthermore, we plot a number of the computed periodic orbits in the phase space for representative frequencies [see the blue orbits in Figure 2.5 **(b)**]. We also include, for a comparison purpose, the corresponding approximated oscillatory solution (plotted in red dashed line), that is described by (2.18). The figure shows that the approximated oscillatory solution represents well the periodic solutions of the single HKB

system (2.2) for the fitted parameter setting.

2.2 The JK-excitator model

In this section, we consider the dynamics of a single JK-excitator and discuss its equivalence to the FitzHugh-Nagumo model. Furthermore, we present a rescaled version for the JKE that allows for a comparison of slow and fast flow to that of the FHN model using the same separation of time-scales. We suggest an approximated version for the JKE and compare its dynamics to the JKE model.

2.2.1 Equivalence of the JK-excitator and FitzHugh-Nagumo models

Recall the Jirsa-Kelso excitator (JKE)

$$\begin{aligned} \dot{u} &= v \\ \dot{v} &= \left(-\frac{b}{3}u^3 + (b-1)u + a + I\right) - \left(u^2 - 1 + \frac{b}{c^2}\right)cv \end{aligned} \tag{2.19}$$

which can be transformed to the FitzHugh-Nagumo (FHN) system

$$\begin{aligned} \dot{u} &= \left(w + u - \frac{u^3}{3}\right)c \\ \dot{w} &= -\left(u - a + bw - I\right)/c \end{aligned} \tag{2.20}$$

by the transformation

$$\begin{bmatrix} u \\ v \end{bmatrix} \mapsto \begin{bmatrix} u \\ \left(w + u - \frac{u^3}{3}\right)c \end{bmatrix} \tag{2.21}$$

Unlike the original work of [9], here we use the same notation for the first dynamical variable of the JKE and FHN models to emphasize that the two equivalent systems share the same dynamic variable, however, it has different meaning to the applications of the two systems (see the discussion below). Here we discuss the topological equivalence of the systems (2.19) and (2.20). We use the notation $\mathbf{v} = [u, v]^\top$ and $\mathbf{w} = [u, w]^\top$ to denote the vectors of dynamic variables of (2.19) and (2.20),

respectively, and let

$$\mathbf{f}(\mathbf{v}) = \begin{bmatrix} v \\ \left(-\frac{b}{3}u^3 + (b-1)u + a + I\right) - \left(u^2 - 1 + \frac{b}{c^2}\right) cv \end{bmatrix}$$
$$\mathbf{g}(\mathbf{w}) = \begin{bmatrix} (w + u - \frac{u^3}{3})\ c \\ -(u + bw - a - I)/c \end{bmatrix}$$

refer to the right hand side of JKE (2.19) and FHN (2.20), respectively. The transformation (2.21) can be denoted by $\mathbf{h} : \mathbf{w} \mapsto \mathbf{v}$, where $\mathbf{h}$ is defined by

$$\mathbf{h}(\mathbf{w}) = \begin{bmatrix} u \\ \left(w + u - \frac{u^3}{3}\right) c \end{bmatrix} \tag{2.22}$$

and has the inverse

$$\mathbf{h}^{-1}(\mathbf{v}) = \begin{bmatrix} u \\ \left(\frac{v}{c} - u + \frac{u^3}{3}\right) c \end{bmatrix} \tag{2.23}$$

The Jacobian matrix and its inverse for $\mathbf{h}$ are given, respectively, by

$$\mathbf{M} = \begin{bmatrix} 1 & 0 \\ -c(u^2 - 1) & c \end{bmatrix}$$

$$\mathbf{M}^{-1} = \begin{bmatrix} 1 & 0 \\ (u^2 - 1) & 1/c \end{bmatrix}$$

Observe that

$$\begin{aligned} \mathbf{M}^{-1}\ \mathbf{f}(\mathbf{h}(\mathbf{w})) = & \\ & \mathbf{M}^{-1} \begin{bmatrix} (w + u - \frac{u^3}{3})\ c \\ \left(-\frac{b}{3}u^3 + (b-1)u + a + I\right) - \left(u^2 - 1 + \frac{b}{c^2}\right) c^2 (w + u - \frac{u^3}{3}) \end{bmatrix} \\ & = \begin{bmatrix} 1 & 0 \\ (u^2 - 1) & 1/c \end{bmatrix} \begin{bmatrix} (w + u - \frac{u^3}{3})\ c \\ -c^2(u^2 - 1)(w + u - \frac{u^3}{3}) - (u + bw - a - I) \end{bmatrix} \\ & = \begin{bmatrix} (w + u - \frac{u^3}{3})\ c \\ (u + bw - a - I)/c \end{bmatrix} \end{aligned}$$

As the transformation $\mathbf{h}$ is diffeomorphism (invertible and smooth together with its

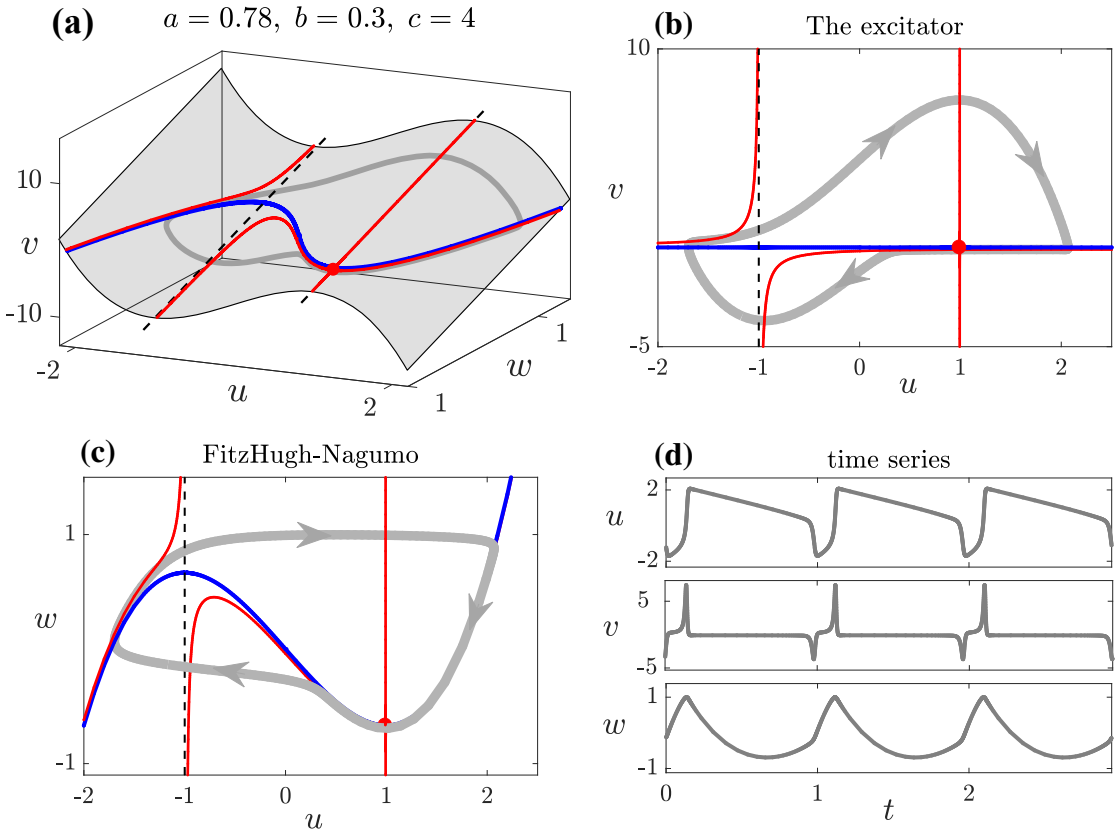

Figure 2.6: Shared dynamics of the JKE and the FHN models. (**a**) hypersurface H 2.24 with nullclines, equilibrium and a periodic orbit. (**b**) and (**c**) state spaces of the JKE (2.19) and the FHN (2.20) systems, respectively. (**d**) time series of the variables u, v and w. In panels (**a-c**): *grey line*, periodic orbit; *blue line*, u-nullcline of the JKE and FHN; *red lines* v-nullcline of the JKE; *dashed black lines* asymptotes of the v-nullcline; *red dot* unstable equilibrium. In panel (**d**): *grey line*, time series of u, v and w corresponding to the periodic orbit in panels (**a-c**).

inverse) and since

$$\mathbf{M}^{-1}\ \mathbf{f}(\mathbf{h}(\mathbf{w})) = \mathbf{g}(\mathbf{w}),$$

the JKE (2.19) and FHN (2.20) systems are smoothly equivalent (diffeomorphic) [see definition 2.3 [56]] and their dynamics are topologically equivalent.

The equivalence of dynamics of the JKE and FHN systems can also be easily understood by considering the relation between the state variables u, v and w described in (2.21). We illustrate this relation by projecting the state spaces of the JKE (2.19) and FHN (2.20) systems on the hypersurface H in the (u, v, w)-space

defined by

$$H = \left\{ (u, v, w) \in \mathbb{R}^3 \middle| \; v = \left(w + u - \frac{u^3}{3} \right) c \right\} \tag{2.24}$$

Figure 2.6 illustrates equivalence of the intrinsic dynamics of the JKE (2.19) and the FHN (2.20) models. Panel (**a**) shows the hypersurface H together with projection of the common u-nullcline of the JKE (2.19) and the FHN (2.20) (blue curve) and v-nullcline of the JKE (2.19) (red curve). Additionally, it shows the equilibrium (red dot) and the periodic orbits (grey curve) for representative parameter values. Panels (**b**)-(**c**) illustrate the state spaces of the JKE (2.19) and the FHN (2.20), respectively, which can be viewed as projections of the hypersurface H in panel (**a**) into (u, v)- and (u, w)- planes respectively. The time-series shown in panel (**d**) correspond to the periodic orbit in panel (**a**). Figure 2.6 shows that the variable u is invariant between the two systems, while the variables v and w have a different time-courses. In spite of the invariance of the variable u under the transformation (2.21), the physical interpretations it has in the two models are different. In the JKE (2.19) system, the variable u represents the position of a moving effector while the variable v describes the velocity. Whereas, in the FHN (2.20) system, u has been commonly interpreted as a membrane potential of a neuronal cell, while the variable w represents a recovery variable associated with a slow dynamics (usually attributed to ion channels' gating) that controls the generation of action potentials [40, 60].

2.2.1.1 Numerical bifurcation analysis

In order to illustrate further the various dynamical regimes shared by the JKE (2.19) and the FHN (2.20) models, we perform numerical bifurcation analysis using numerical continuation in `XPPAUT`. In our computations we consider the case $I = 0$.

First, we continue the steady states and periodic orbits in the parameter b for representative values of the parameter a and fixed $c = 2$. The resulting bifurcation diagrams are shown in Figures 2.7-2.9. Panels (**a-b**) in Figure 2.7 show the bifurcation diagram of the JKE and FHN systems, respectively, for $a = 1$. Three equilibrium branches exist for $b < 0$, two of them are of saddle type and the intermediate branch is a node. The two saddle branches diverge as $b \to 0$ having an asymptote at $b = 0$. As the parameter b increases, a stable periodic solution is born from homoclinic bifurcation and ends in a subcritical Hopf bifurcation where the unstable equilibrium gains stability.

For $a = 0.1$ (Figure 2.7 panels **c-d**), similar scenario occurs for $b < 0$. Two saddle branches diverge before $b = 0$ leaving one unstable node branch, and homoclinic bifurcation gives birth to a stable branch of periodic orbits. However, the Hopf bifurcation is now supercritical giving rise to an unstable branch of periodic orbits which merges and collides with the stable orbit branch in a saddle-node bifurcation of limit cycles. In addition, a saddle-node bifurcation gives birth to two branches of unstable equilibria. The branch of unstable nodes gains stability after a second supercritical Hopf bifurcation giving rise to an extra branch of unstable periodic orbits which ends at a homoclinic bifurcation (Figure 2.7 panels **c2-d2**).

For $a = 0.03$ (Figure 2.8), the bifurcation for $b < 0$ is similar to the previous cases. However, as b increases, the saddle-node bifurcation of equilibria occurs before the first supercritical Hopf bifurcation. The unstable branch of periodic orbit emanating from the Hopf bifurcation ends in a small homoclinic (surrounding one equilibrium) (Figure 2.8 panels **c2-d2**). Then, a large homoclinic (surrounding two equilibria) occurs giving existence to another branch of unstable periodic orbits which merges and collides with stable branch of periodic orbits in a saddle-node bifurcation of limit cycles (Figure 2.8 panels **c3-d3**). The other bifurcation scenarios are similar to the case $a = 0.1$ mentioned above.

The bifurcation diagram for $a = 0$ is symmetric about the b-axis (Figure 2.9).

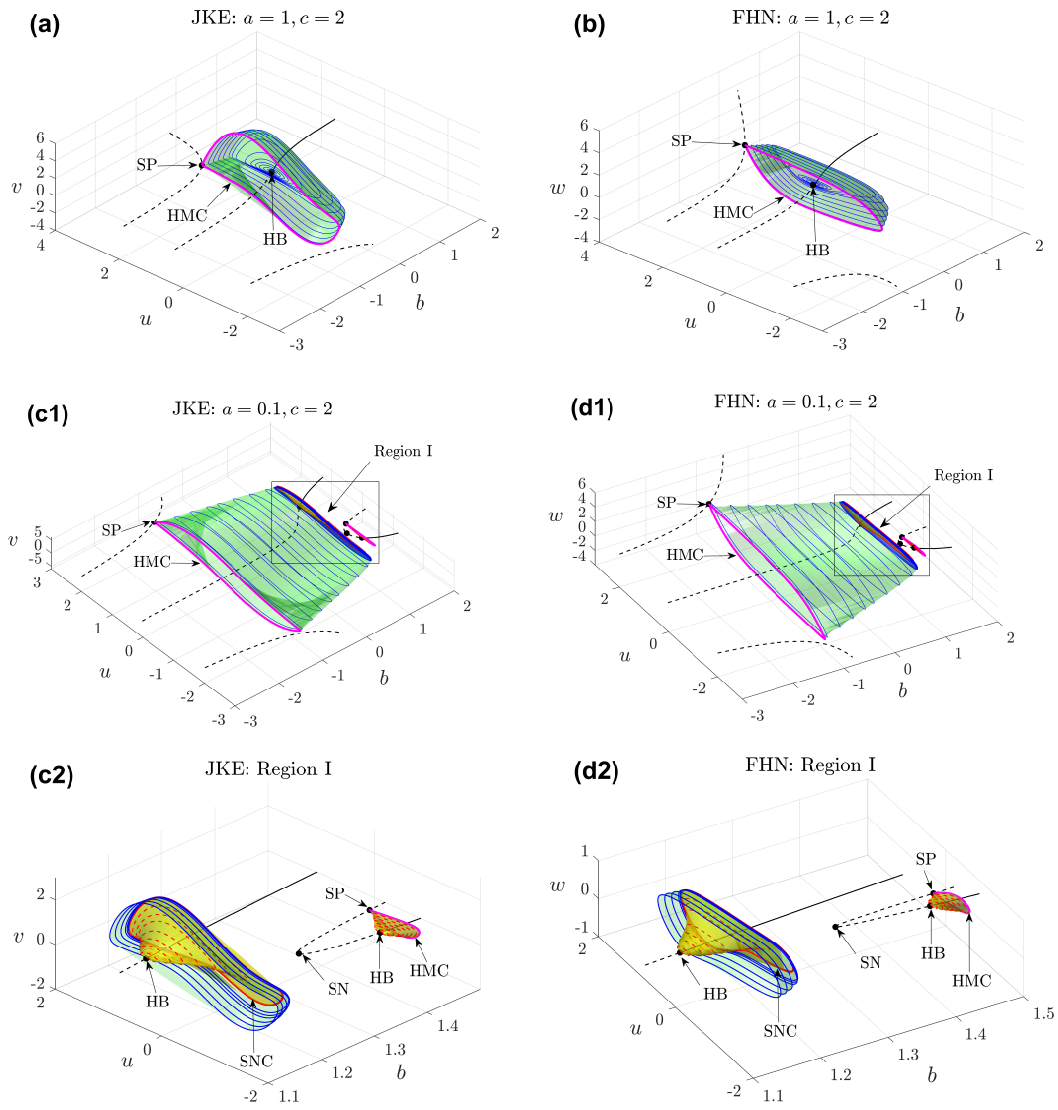

Figure 2.7: Bifurcation diagrams of JKE and FHN systems for a=1 and a=0.1. Phase space against the bifurcation parameter b. Panels (**a-b**) for $a = 1, c = 2$, and panels (**c-d**) for $a = 0.1, c = 2$. Panels (**c2**) and (**d2**) show zoomed regions from panels (**c1**) and (**d1**), respectively. The left column panels (**a**) and (**c**) for JKE system (2.19) and the right column panels (**b**) and (**d**) for FHN system (2.20). *Solid* (*dashed*) *black curves* for stable (unstable) branches of equilibrium, respectively; *solid blue* (*dashed red*) *cycle* for stable (unstable) periodic orbit, respectively; *magenta curve* for homoclinic trajectory (*HMC*); *solid red cycle* for saddle-node limit cycle (*SNC*); *SP* for saddle equilibrium; *SN* for saddle-node equilibrium; *HB* for Hopf bifurcation.

As the parameter b increases, a heteroclinic cycle bifurcation (double heteroclinic trajectories connecting two saddles) gives birth to the branch of stable periodic

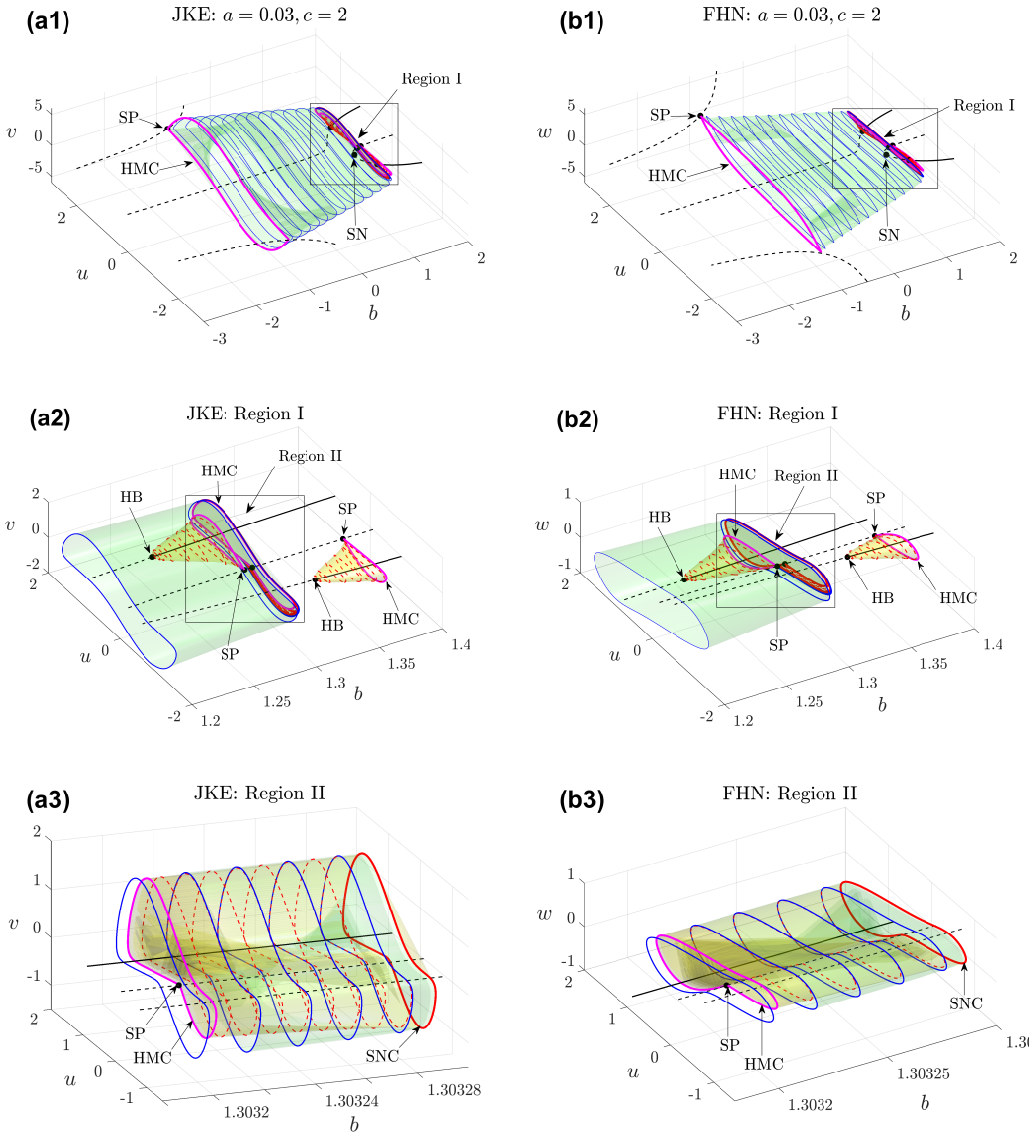

Figure 2.8: Bifurcation diagrams of JKE and FHN systems for a=0.03. Phase space against the bifurcation parameter b for $c = 2$. Panels (**c2-d2**) and (**c3-d3**) show zoomed regions from panels (**c1-d1**) and (**c2-d2**), respectively. The left column panels (**a1-3**) for JKE system (2.19) and the right column panels (**b1-3**) for FHN system (2.20). *Solid* (*dashed*) *black curves* for stable (unstable) branches of equilibrium, respectively; *solid blue* (*dashed red*) *cycle* for stable (unstable) periodic orbit, respectively; *magenta curve* for homoclinic trajectory (*HMC*); *solid red cycle* for saddle-node limit cycle (*SNC*); *SP* for saddle equilibrium; *SN* for saddle-node equilibrium; *HB* for Hopf bifurcation.

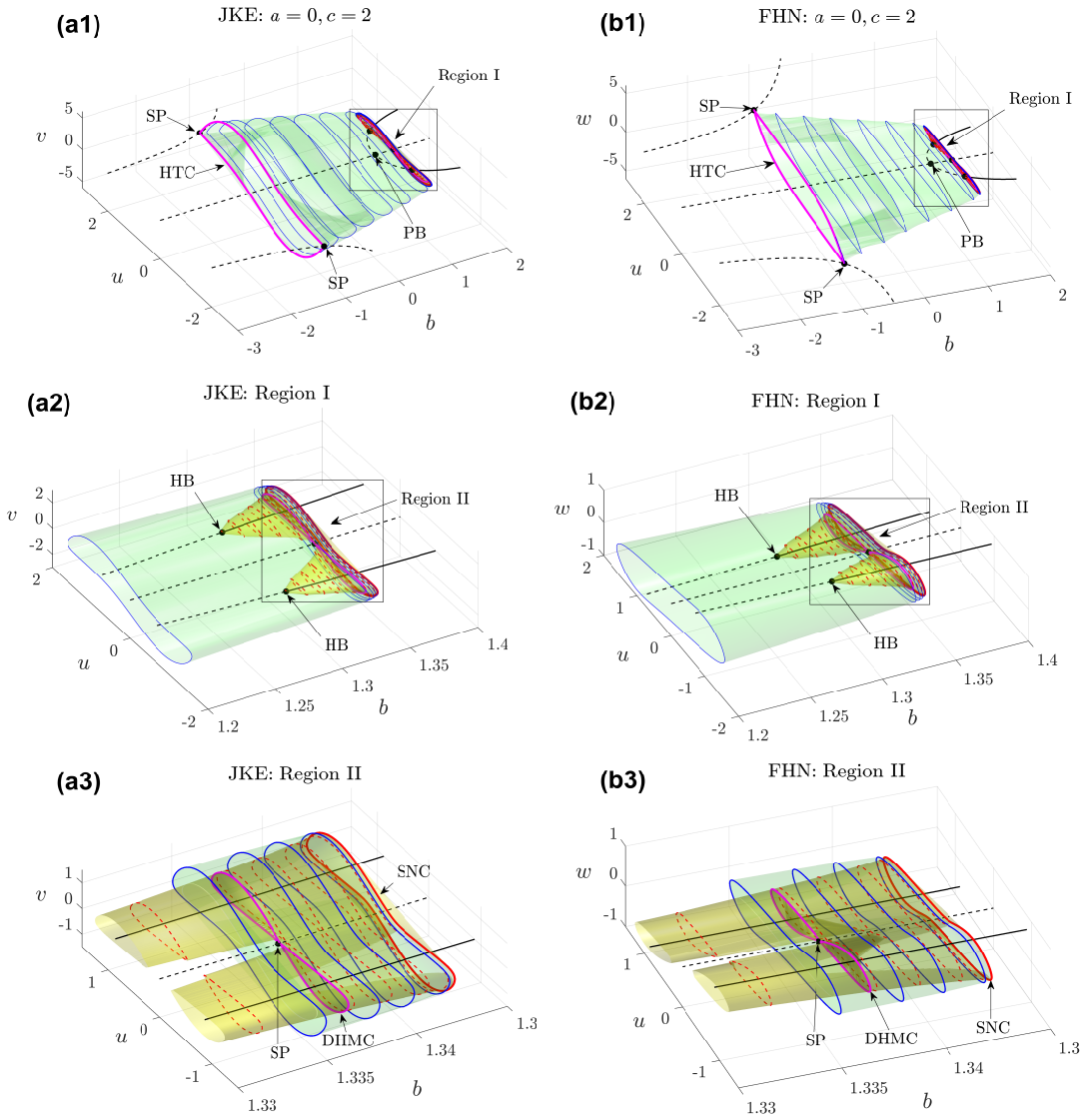

Figure 2.9: Bifurcation diagram of JKE and FHN systems for a=0. Phase space against the bifurcation parameter b for $c = 2$. Panels (**c2-d2**) and (**c3-d3**) show zoomed regions from panels (**c1-d1**) and (**c2-d2**), respectively. The left column panels (**a1-3**) for JKE system (2.19) and the right column panels (**b1-3**) for FHN system (2.20). *Solid* (*dashed*) *black curves* for stable (unstable) branches of equilibrium, respectively; *solid blue* (*dashed red*) *cycle* for stable (unstable) periodic orbit, respectively; *magenta curve* for heteroclinic cycle (*HTC*) and double homoclinic (*DHMC*); *solid red cycle* for saddle-node limit cycle (*SNC*); *SP* for saddle equilibrium; *PB* for pitchfork bifurcation; *HB* for Hopf bifurcation.

orbits. Furthermore, a pitchfork bifurcation yields the unstable node to become of saddle type and two unstable equilibrium branches of node type bifurcate from the pitchfork point (Figure 2.9 panels **a1-b1**). In addition, two supercritical Hopf bifurcations give rise to two branches of unstable periodic orbits leading the unstable equilibrium branches to gain stability (Figure 2.9 panels **c2-d2**). The two branches of unstable orbits expand and end in a double homoclinic bifurcation (two homoclinic trajectories connected to the same saddle point). Then, the double homoclinic breaks and leads to a single family of large unstable periodic orbits that merges and collides with the branch of stable periodic orbits in a saddle-node bifurcation of limit cycles (Figure 2.9 panels **c3-d3**).

Next, we continue the bifurcations occurring in Figures 2.7-2.9 in the two parameters a and b. The resulting bifurcation diagrams are shown in Figure 2.10.

Four (black) curves, corresponding to the locus of saddle-node bifurcation of equilibrium, separate the regions in (a, b)-plane according to the number of the corresponding equilibria. In the left half of the plane (for $b < 0$), the regions labelled as R1 correspond to a single equilibrium of saddle type. The regions between the two saddle-node locus curves correspond to three equilibria; two of them are saddle points diverging, in the state variables, as $b \to 0$, and the third one is a node. In the right half of the plane (for $b > 0$), the two saddle-node locus curves are connected at a cusp bifurcation. The region between the two saddle-node locus curves labelled as R3, corresponds to three equilibria (two nodes and one saddle). The other regions in the right half plane, apart from R3 and the saddle-node locus curve, correspond to a single equilibrium of node type (see Figure 2.10 panels **a**).

In addition, four Bogdanov-Takens bifurcation points (BT) are situated on the saddle-node locus curves bounding two (grey) curves representing the locus of Hopf bifurcations. Furthermore, the Hopf bifurcation switches its criticality via two generalised Hopf bifurcation points (GHB) which are situated on the Hopf bifurcation locus curves and connected by a (red) curve corresponding to the locus of saddle-node bifurcation of limit cycles (see Figure 2.10 panels **b-c**).

Also, four (magenta) curves, corresponding to the locus of homoclinic bifurcations, start from the four Bogdanov-Takens bifurcation points (BT). The two homoclinic locus curves in the left half of the (a, b)-plane end at a heteroclinic cycle bifurcation (HTC) (Figure 2.10 panel **a**), whereas, the two homoclinic locus curves

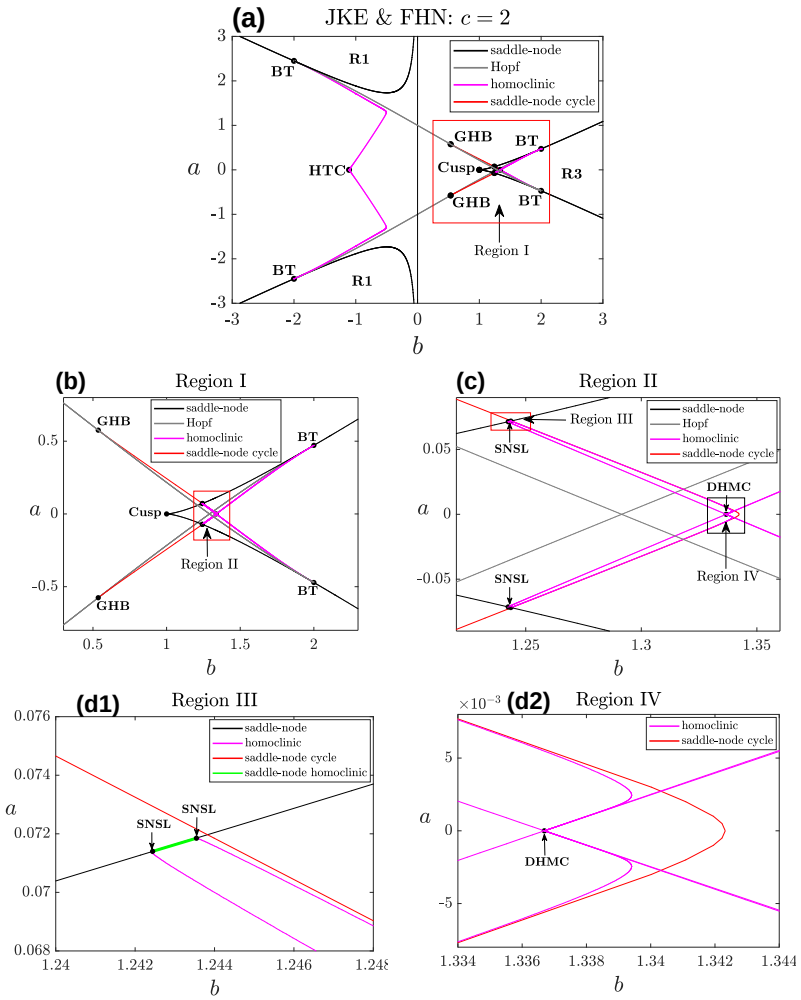

Figure 2.10: Bifurcation diagrams of JKE and FHN systems in (a, b)-plane. The curves represent two-parameter continuations (in a and b) of bifurcations occurring in Figures 2.7-7: *black* for locus of saddle-node bifurcation; *grey* for locus of Hopf bifurcation; *magenta* for locus of homoclinic bifurcation; *red* for locus of saddle-node bifurcation of limit cycles; *green* for locus of saddle-node homoclinic. The black dots correspond to codim 2 bifurcations: *BT* for Bogdanov-Takens bifurcation; *GHB* for generalized Hopf (Bautin) bifurcation, *Cusp* for Cusp bifurcation; *HTC* for heteroclinic cycle; *DHMC* for double homoclinic; *SNSL* for saddle-node separatrix-loop bifurcation. Three eqiulibria exist in the left half plane (for $b < 0$) except on the saddle-node curves and in the regions labeled as *R1* (corresponding to a single equilibrium). Whereas, a single equilibrium exists in the right half plane (for $b \geq 0$) except on the saddle-node curves and in the region labeled *R3* (corresponding to three equilibria).

in the right half of the (a, b)-plane end at a double homoclinic curve (DHMC) (Figure 2.10 panel **d2**). Moreover, the latter homoclinic locus curves become tangent to the saddle-node locus curve (corresponding to a saddle-node homoclinic) via a saddle-node separatrix-loop bifurcation (SNSL) [61]. The saddle-node homoclinic branches continue for a small range before leaving the saddle-node locus curve via another saddle-node separatrix-loop bifurcation (Figure 2.10 panel **d1**). The left magenta curve in panel (**d1**) corresponds to small homoclinic, while, the right magenta curve represents big homoclinic (see Figure 2.8 panels **a2-b2**). The two-parameter bifurcation diagram for $c > 2$ is qualitatively similar to Figure 2.10. However, as the parameter c increases, the loci of Bogdanov-Takens and generalized Hopf bifurcation points spread towards infinity narrowing the regions between the adjacent loci of bifurcations, such as the Hopf and saddle-node of limit cycles bifurcation curves, and Hopf and homoclinic bifurcation curves lying in the right half of the (a, b)-plane [41]. We remark here that the bifurcation diagrams we presented above qualitatively agree with known results for the FHN model (2.20) in the literature (see the qualitative representation of the two-parameter bifurcation diagram of the FHN system for general values of the parameter c in Chapter 5 [41]).

2.2.1.2 Implications of the bifurcation analysis for movement modelling

The essential contribution of the JK-excitator is to provide a description of the dynamics of different movement classes through phase flow topologies of a unified dynamical model [9, 13]. Given suitable topological constraints on the phase flow, namely: the boundedness of the trajectories; the existence of a separatrix marking the boundary between two separate regimes; and the existence of attractors, the JK-excitator model (2.19) supports three main dynamical regimes: stable fixed point(s) for monostable and bistable discrete movements and a stable limit cycle for rhythmic movements [9, 13, 38, 39]. Therefore, identifying the parameter ranges corresponding to each distinct dynamical regime is of crucial importance to the empirical implications of the model. This identification would help in choosing the appropriate model parameter setting that suits the concerned movement task. In this section, we explain the meaning of different regions of Figure 2.10 in terms of movement modelling by relating the corresponding parameter setting to the class of movements that can be described by the dynamics of the JK-excitator model.

From the bifurcation analysis illustrated in Figure 2.10, it can be clearly noticed that sizable regions in the (a, b) parameter plane can be identified to support the different desired regimes. Firstly, the class of rhythmic movements can be described by a dynamic supporting stable periodic regimes. Hence, the rhythmic movement dynamics are supported in the region corresponding to the existence of stable limit cycle, which lies in the centre of the (a, b)-plane and it is bounded from the left by the left homoclinic locus curves and from the right by the locus curves of Hopf bifurcation and saddle-node of limit cycles.

Secondly, the class of monostable discrete movements, movements starting and ending at the same point, can be described by dynamics supporting the existence of a single stable equilibrium, which is corresponding to the regions of the parameter space lying between the locus curves of Hopf and saddle-node bifurcations in the left half of the (a, b)-plane and above the top Hopf and saddle-node locus curves or below the bottom Hopf and saddle-node locus curves in the right half of the (a, b)-plane.

Finally, the class of bistable discrete movements, movements starting at a point and ending at another, can be described by dynamics supporting the existence of two stable equilibrium, which is corresponding to the part of the region labeled as R3 (in the right half of the (a, b)-plane) that is bounded from the left by the right locus of homoclinic bifurcation. This region corresponds to bistable dynamics determined by two stable equilibria with attraction basins separated by the stable manifold of a saddle point.

2.2.2 Separation of time scales in the JK-excitator

The time parameter c in (2.19) is required to be sufficiently large $c \gg 1$ to guarantee a sufficient separation of time scales that leads to suitable fast flow and threshold proprieties in the JK-excitator [9]. In addition, analysing the fast and slow behaviour of the phase flow in the JKE model (2.19) would give us better understanding of some key topological characteristics in the JKE model, such as threshold properties and canards phenomena, and allow for a comparison to similar features in the classical FHN model (2.20). Therefore, and consistent with the convention of *Multiple time scale dynamics* [62–64], we define the separation of time scales as small parameter $\varepsilon = \frac{1}{c^2} \ll 1$, corresponding to the large constant $c = \frac{1}{\sqrt{\varepsilon}} \gg 1$. Hence, the JK-excitator

model described by (2.19) can be written as:

$$\begin{aligned} \dot{u} &= v \\ \dot{v} &= \left(-\frac{b}{3}u^3 + (b-1)u + a + I\right) - \left(u^2 - 1 + b\varepsilon\right)\frac{v}{\sqrt{\varepsilon}} \end{aligned} \tag{2.25}$$

or

$$\begin{aligned} \dot{u} &= v \\ \sqrt{\varepsilon}\,\dot{v} &= \sqrt{\varepsilon}\left(-\frac{b}{3}u^3 + (b-1)u + a + I\right) - \left(u^2 - 1 + b\varepsilon\right)v \end{aligned} \tag{2.26}$$

with time-differentiation notation $(\cdot)' = \frac{d}{ds}$. Similarly, the FHN model (2.20) can be written (after rescaling the time by $\sqrt{\varepsilon}$) as:

$$\begin{aligned} \varepsilon\,\dot{u} &= \left(w + u - \frac{u^3}{3}\right) \\ \dot{w} &= -\left(u - a + bw - I\right) \end{aligned} \tag{2.27}$$

As the time scales are mixed in the right hand side of the JKE (2.26) while they are unmixed in the FHN model (2.27) [9], it might be more appropriate for comparison purposes to introduce an equivalent representation of the JKE system (2.26) that allows for slow-fast analysis in the same time scales ratio of the FHN model. This can be achieved by rescaling the time variable (s) and the state variable (v) by $\sqrt{\varepsilon}$. Therefore, we introduce the new notation:

$$\left(\frac{s}{\sqrt{\varepsilon}}, u, \frac{v}{\sqrt{\varepsilon}}, w\right) \rightarrow (t, x, y, z) \tag{2.28}$$

The resulting JKE and FHN models is, respectively, read:

$$\begin{aligned} x' &= \varepsilon\, y \\ y' &= \left(-\frac{b}{3}x^3 + (b-1)x + a\right) - \left(x^2 - 1 + \varepsilon b\right) y \end{aligned} \tag{2.29}$$

$$\begin{aligned} x' &= \left(z + x - \frac{x^3}{3}\right) \\ z' &= -\,\varepsilon\,\left(x - a + bz - I\right) \end{aligned} \tag{2.30}$$

with time-differentiation notation $(\cdot)' = \frac{d}{dt}$. The corresponding homeomorphism transformation between (2.29) and (2.30) has the form:

$$y = \left(z + x - \frac{x^3}{3} \right) \Big/ \varepsilon \tag{2.31}$$

Henceforth, by JKE and FHN, we refer to the systems (2.29) and (2.30), respectively.

2.2.3 The approximated excitator

For large separation of time scales of the JKE system (2.29), the time-scales separation parameter has to be small $\varepsilon \ll 1$. The contribution of the term $(\varepsilon b\, y)$ in the second equation of (2.29) to the fast dynamic of the JKE system is negligible for small values of ε. Therefore, for sufficiently small $\varepsilon \ll 1$, ignoring the effect of the term $(\varepsilon b\, y)$ would not alter the dynamic of the JKE system. Notice that the term ϵy in the first equation has an important contribution to the slow flow of the system and ignoring it leads to a singular case as we will discuss in the next chapter. Hence, we propose an approximated version of the JKE system (2.29) by dropping the term $(\varepsilon b\, y)$ from the second equation in (2.29) leading to the system:

$$\begin{aligned} x' &= \varepsilon\, y \\ y' &= \left(-\frac{b}{3} x^3 + (b-1)x + a \right) - \left(x^2 - 1 \right) y \end{aligned} \tag{2.32}$$

We refer to (2.32) as *the approximated excitator* (AEX). The representation in (2.32) involves clear separation of the time scales since the parameter ε can be completely removed from either of the system equations by rescaling the time. The rest of this section be dedicated to comparing the dynamics of the approximated excitator (AEX) to the JK-excitator (JKE).

2.2.3.1 Comparison of dynamics of the JKE and AEX

First, it can be easily noticed that both the JKE and the AEX systems have the same slow and fast subsystems in the limit $\varepsilon \to 0$. Furthermore, the nullcline of the fast variable y of the JKE approaches the y-nullcline of the AEX, which represents the critical manifold of both systems at the singular limit $\varepsilon = 0$.

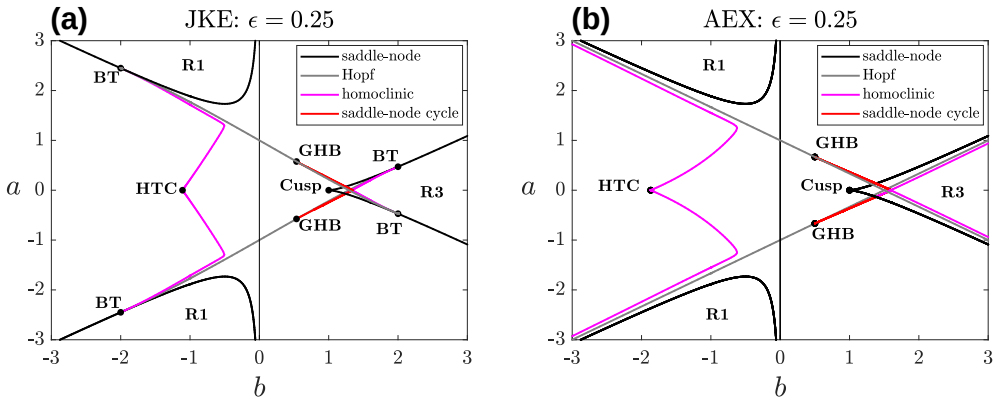

Figure 2.11: Bifurcation diagram of JKE and AEX systems in (a,b)-plane. Panel (**a**) for JKE system (2.29), panel (**b**) for AEX system (2.32). The colors and labels are similar to Figure 2.10. The diagrams show that the bifurcation diagram of the AEX system is qualitatively similar to the diagram of the JKE, except of the disappearance of Bogdanov-Takens bifurcations as the loci of saddle-node, Hopf and homoclinic bifurcations are asymptotically parallel.

In order to compare the dynamics for $\varepsilon > 0$, we carry out two-parameter bifurcation analysis of the JKE system (2.29) and the AEX system (2.32) using numerical continuation in `XPPAUT` for $\varepsilon = 0.25$, corresponding to the value $c = 2$ in the bifurcation analysis of the JKE model we presented earlier. The resulting bifurcation diagrams are illustrated in Figure 2.11. The bifurcation diagram of the AEX is qualitatively similar to that of the JKE (*i.e.* they both have almost similar distribution of the loci of bifurcations in the parameter plane except for some small regions). However, the locus of saddle-node, Hopf and homoclinic bifurcation are asymptotically parallel, and no Bogdanov-Takens bifurcations exist.

To explain theoretically the difference between the two bifurcation diagrams, we test the existence condition of the Bogdanov-Takens bifurcation for the JKE and the AEX systems.

The equilibria of both (2.29) and (2.32) systems must satisfy $p(x) = 0$ and $y = 0$, where

$$p(x) := -\frac{b}{3}x^3 + (b-1)x + a \tag{2.33}$$

The saddle-node bifurcation of the systems (2.29) and (2.32) is associated with the double roots of (2.33). Let x_e be a root of (2.33), the linearization of the JKE (2.29)

and the AEX (2.32) systems at the equilibrium $(x_e, 0)$ are given, respectively, by the Jacobian matrices:

$$J_{\text{JKE}} = \begin{bmatrix} 0 & \varepsilon \\ -[b(x_e^2-1)+1] & -[(x_e^2-1)+\varepsilon b] \end{bmatrix} \tag{2.34}$$

$$J_{\text{AEX}} = \begin{bmatrix} 0 & \varepsilon \\ -[b(x_e^2-1)+1] & -(x_e^2-1) \end{bmatrix} \tag{2.35}$$

The eigenvalues of the linearization have the form

$$\lambda_i = \frac{1}{2}\left(\sigma_i \pm \sqrt{\sigma_i^2 - 4\Delta_i}\right) \qquad i =_{\text{JKE, AEX}} \tag{2.36}$$

where

$$\begin{aligned} \sigma_{\text{JKE}} &= -\left[(x_e^2-1)+\varepsilon b\right] \\ \Delta_{\text{JKE}} &= \varepsilon\left[b(x_e^2-1)+1\right] \end{aligned} \tag{2.37}$$

and

$$\begin{aligned} \sigma_{\text{AEX}} &= -\left(x_e^2-1\right) \\ \Delta_{\text{AEX}} &= \varepsilon\left[b(x_e^2-1)+1\right] \end{aligned} \tag{2.38}$$

Hopf bifurcation requires a conjugate pair of pure imaginary eigenvalues, corresponding to $\sigma_i = 0$. Therefore, for the JKE system (2.29), the Hopf bifurcation is associated with the equilibria

$$(x_{\text{H}}, y_{\text{H}}) = \left(\pm\sqrt{1-\varepsilon b}, 0\right) \tag{2.39}$$

Since the equilibria satisfies $p(x_e) = 0$, we conclude that

$$a_{\text{H}} = \pm\sqrt{1-\varepsilon b}\left(1 - \frac{2}{3}b - \frac{1}{3}\varepsilon b^2\right) \tag{2.40}$$

The parameter relation (2.40) describes the locus of Hopf bifurcation of the JKE in the (a, b) parameter plane [41]. Similarly, the Hopf bifurcation in the AEX system (2.32) is associated with

$$(x_{\text{H}}, y_{\text{H}}) = (\pm 1, 0) \tag{2.41}$$

$$a_{\mathrm{H}} = \pm\left(1 - \frac{2}{3}b\right) \tag{2.42}$$

Notice that the relation (2.40) turns to (2.42) in the limit $\varepsilon \to 0$.

Furthermore, the saddle-node (fold) bifurcation requires a zero eigenvalue corresponding to $\Delta_i = 0$. Hence, for both systems, the saddle-node bifurcation is associated with

$$(x_{\mathrm{F}}, y_{\mathrm{F}}) = \left(\pm\sqrt{1 - \frac{1}{b}}, 0\right) \tag{2.43}$$

$$a_{\mathrm{F}} = \pm\frac{2}{3}(1-b)\sqrt{1 - \frac{1}{b}} \tag{2.44}$$

The Bogdanov-Takens bifurcation requires the existence of double zero eigenvalues, which is satisfied if $\sigma_i = \Delta_i = 0$. This corresponds to tangential intersections between the loci of Hopf and saddle-node bifurcations in the (a, b)-plane. For the JKE system (2.29), the locus of Bogdanov-Takens bifurcations in the (a, b)-plane are determined by:

$$\begin{aligned} a_{\mathrm{BT}} &= \pm\frac{2}{3}(1 - b_{\mathrm{BT}})\sqrt{1 - \frac{1}{b_{\mathrm{BT}}}} \\ b_{\mathrm{BT}} &= \pm\frac{1}{\sqrt{\varepsilon}} \end{aligned} \tag{2.45}$$

The relations (2.45) hold also for the equivalent FHN system (2.30) (see [41] for more details about Bogdanov-Takens bifurcation in the FHN model).

For the AEX system (2.32), the lines described by (2.42) corresponding to the locus of Hopf bifurcation are asymptotes to the locus of saddle-nod bifurcation, described by (2.44), in the (a, b)-plane. To show this, consider the limit of the

difference between (2.44) and (2.42) as $b \to \infty$:

$$\begin{aligned}
\lim_{b\to\infty}\left[a_{\mathrm{F}} - a_{\mathrm{H}}\right] &= \lim_{b\to\infty}\left[\pm\frac{2}{3}(1-b)\sqrt{1-\frac{1}{b}}\right] - \left[\pm\left(1-\frac{2}{3}b\right)\right] \\
&= \pm\lim_{b\to\infty}\left[\frac{2}{3}b\left(1-\sqrt{1-\frac{1}{b}}\right)+\frac{2}{3}\sqrt{1-\frac{1}{b}}-1\right] \\
&= \pm\lim_{b\to\infty}\left[\frac{2}{3}b\,\frac{\left(1-\left(1-\frac{1}{b}\right)\right)}{\left(1+\sqrt{1-\frac{1}{b}}\right)}+\frac{2}{3}\sqrt{1-\frac{1}{b}}-1\right] \\
&= \pm\lim_{b\to\infty}\left[\frac{2}{3}\,\frac{1}{\left(1+\sqrt{1-\frac{1}{b}}\right)}+\frac{2}{3}\sqrt{1-\frac{1}{b}}-1\right] \\
&= \pm\left[\frac{2}{3}\,\frac{1}{2}+\frac{2}{3}-1\right] = 0
\end{aligned}$$

Therefore, no tangential intersections exist among the loci of Hopf and saddle-node bifurcations of the AEX for finite parameter values in the (a, b)-plane. The absence of such intersections suggests that removing the term $(\varepsilon b\, y)$ from the JKE system results in shifting the locus of Bogdanov-Takens bifurcation in the parameter plane to infinity. Nevertheless, the infinite locus of the Bogdanov-Takens bifurcation in the AEX can be viewed by projecting the parameter plane onto Poincaré sphere (see section B.2 in the Appendices).

2.3 Summary

In this chapter, we explore the dynamics of the single HKB oscillator and JKE model.

In the first section, we discuss the dynamics of the HKB hybrid oscillator. We review the possible bifurcation of the system and classify the parameter space according to the different types and stability of the model solutions. Furthermore, we identify the parameter ranges corresponding to dynamical regimes that are suitable for modelling rhythmic movements. Moreover, we discuss approximating oscillatory solutions of fixed amplitude demonstrating how well they represent the actual

numerical solutions of the HKB single oscillator (computed for physically relevant parameter setting) in terms of phase-space characteristics and frequency-induced drop of amplitude property. The overall analysis examines and confirms the suitability of the HKB hybrid oscillator to describe the dynamics of a rhythmically moving effector, as well as the intrinsic properties of the coordination dynamics of two interactively moving effectors (as we consider in chapter 4).

In the second section, we consider the dynamics of the JK-excitator. Again using bifurcation analysis, we identify the parameter regimes for which the JKE model supports dynamics of various movement classes (such as mono- and bistability of fixed points, in addition to periodic stability dynamics describing, respectively, discrete and rhythmical motor behaviours). Furthermore, we review the equivalence of dynamics in the JKE and FHN models for finite separation of time scales establishing the invariance in the pure dynamics and the distinction in the physical meaning of the dynamical variable shared between the two models. Moreover, we propose a rescaled representation of the JKE system, in addition to an approximated model, that exhibits explicit separation of time-scales allowing for a direct comparison of the nonequivalent slow-fast dynamics of the JKE and FHN models in the singular case of infinite separation of time-scales (as we carry out in the next chapter).

Chapter 3

Canards in the JK-excitator model

In this chapter, we investigate the canard phenomena in the Jirsa-Kelso excitator (JKE) model. We discuss the canard explosion and perform slow-fast analysis to understand the dynamical mechanisms organising the canard cycles in the JKE model and to compare these mechanisms to the corresponding ones organising the classical canards in the FitzHugh-Nagumo (FHN) model. We apply a combination of dynamical techniques (see Appendix B) to understand the local and global behaviour of singular canard cycles that differ from the classical canard cycles organised by an N shaped critical manifold. Moreover, we discuss various approaches to define and compute the maximal canard cycle.

3.1 Singular Hopf and canard explosion

Equivalent to FHN model (2.30), the existence of canard solutions in the JKE model (2.29) is associated with a canard explosion, a rapid growth of periodic orbits' amplitude that happens in an a range of the bifurcation parameter values of length $\mathcal{O}(\exp(-\frac{K}{\varepsilon}))$, for some constant $K > 0$ independent of ε. The canard explosion exists at an $\mathcal{O}(\varepsilon)$ distance from a singular Hopf bifurcation in the control parameter range [50, 62, 63]. The parameter values corresponding to the singular Hopf bifurcation of the JKE model are $a = \pm a_H$ where

$$a_H := \sqrt{1-\varepsilon b}\left(1 - \frac{2}{3}b - \varepsilon\frac{b^2}{3}\right) \tag{3.1}$$

for which the x-coordinate of the equilibrium are $x = \pm x_H$, respectively, where

$$x_H := \sqrt{1 - \varepsilon b} \tag{3.2}$$

(see (2.40) and (2.39)).

Notice that for the singular limit $\varepsilon \to 0$, a_H and x_H have, respectively, the values

$$a_{H_0} = \left(1 - \frac{2}{3}b\right), \tag{3.3}$$

$$x_{H_0} = 1. \tag{3.4}$$

Figure 3.1 illustrates the singular Hopf bifurcation and canard explosion in the excitator model (2.29). Panel **(a)** shows the bifurcation diagram of the steady state and periodic solution in the parameter a. The canard explosion exists within an exponentially small range of the control parameter a at a distance of $\mathcal{O}(\varepsilon)$ from the singular Hopf bifurcation. Panel **(b)** illustrates the (x, y)-phase portraits. The canard periodic orbits are coloured corresponding to the length (Δa) of the range in the parameter a within which the family of solutions exists. For instance, the periodic orbits coloured in dark blue exist within a range of length $\Delta a = 0.1$. While the periodic orbits coloured in dark red exist within a range of length $\Delta a = 10^{-13}$.

However, in contrast to the FHN model, in the JKE the canard explosion is organised by a *non-generic branching point* at the y-nullcline [56], rather than by a fold point [50, 62] (as we discuss in the next section).

3.2 Slow-fast analysis

In this section, we analyse the fast and slow flow of the JKE system (2.29) in the singular limit $\varepsilon = 0$, which provides us with an insight into how the canard solutions are organised for the non-singular case $\varepsilon > 0$. Furthermore, it might be helpful to compare this organisation to the corresponding one known for the well-studied canard phenomena in the FHN model [41, 50]. To this end, we present a slow-fast analysis of the FHN system (2.30) and the JKE system (2.29). We also compare and discuss the different features of canard solutions in the two systems, which can be attributed to the breach of equivalence transformation (2.31) at the singular case

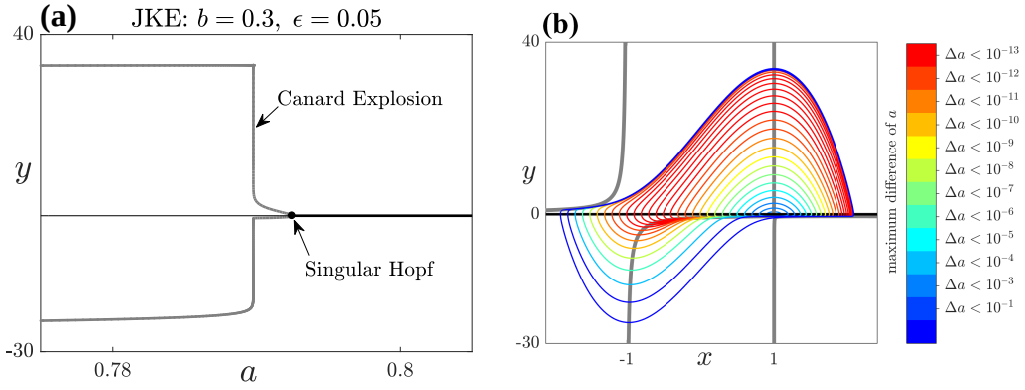

Figure 3.1: Canard explosion in the JKE model. Panel (**a**): bifurcation diagram in the parameter a. *Thick black line* indicates stable branch of equilibria; *thin black line* indicates unstable branch of equilibria; *black circle* indicates the singular Hopf point; *grey line* indicates the max and min values of the variable y along the periodic orbits. Panel (**b**): phase portraits of canard periodic orbits corresponding to panel (**a**). *Black line* for x-nullcline and *grey lines* for y-nullcline; *coloured curves* for canard periodic orbits. The orbit colour is corresponding to the length Δa of range in the control parameter a within which the family of periodic orbits exists.

$\varepsilon = 0$.

3.2.1 Fast subsystem

We first analyse the fast flow by considering the singular limit $\varepsilon = 0$ in the JKE system (2.29) and FHN system (2.30), which are governed by the fast time scales. Beginning with the FHN system (2.30), setting $\varepsilon = 0$ leads to the FHN fast subsystem given by

$$\begin{aligned} x' &= \left(z + x - \frac{x^3}{3} \right) \\ z' &= 0 \end{aligned} \tag{3.5}$$

Since $z' = 0$, we can treat z as a constant parameter and consider (3.5) as a one dimensional system with flow in horizontal direction. Hence, each value of z defines flow of (3.5) along 1D invariant manifold (layer) in the (x, z)-plane. The critical manifold of the FHN model, corresponding to the set of equilibria of system (3.5)

as z changes, is given by

$$S_0 = \left\{ (x,z) \in \mathbb{R}^2 |\, z = f(x) := \frac{x^3}{3} - x \right\} \tag{3.6}$$

the curve S_0 has N shape and represents the nullcline of the fast variable x. Furthermore, the hyperbolicity of the equilibria along S_0 is determined by the sign of the nontrivial eigenvalue of (3.5) given by $\lambda_f = \partial_x \left(z - f(x)\right) = 1 - x^2$. Therefore, the critical manifold has two stable branches over $x \in (-\infty, -1) \cup (1, \infty)$ and one unstable branch over $x \in (-1, 1)$ connected by two nonhyperbolic points $(x,z) = \left(\pm 1, \mp \frac{2}{3}\right)$, for which the FHN fast subsystem (3.5) undergoes saddle-node (fold) bifurcation as z changes.

Similarly, setting $\varepsilon = 0$ in the JKE system (2.29) leads to the JKE fast subsystem (layer problem):

$$\begin{aligned} x' &= 0 \\ y' &= \left(-\frac{b}{3}x^3 + (b-1)x + a \right) - \left(x^2 - 1\right) y \end{aligned} \tag{3.7}$$

Since $x' = 0$, we can treat x as a constant parameter and consider (3.7) as a one dimensional system with flow in vertical direction. Hence, each value of x defines flow of (3.7) along 1D invariant manifold (layer) in the (x,y)-plane. Furthermore, as we consider x as a constant, the system (3.7) is linear and the explicit form of the fast flow is straightforward. For $x = \pm 1$, the flow is given by $y(t; \pm 1) = p(\pm 1)\, t$, where p is the polynomial

$$p(x) := -\frac{b}{3}x^3 + (b-1)x + a. \tag{3.8}$$

For $x \neq \pm 1$, the flow of the fast JKE subsystem can be described by:

$$y(t; x) = A e^{-(x^2-1)t} + \varphi(x) \tag{3.9}$$

where $A \in \mathbb{R}$ is an arbitrary constant and $\varphi(x)$ is defined by

$$\varphi(x) := \frac{p(x)}{(x^2-1)} = \frac{\left(-\frac{b}{3}x^3 + (b-1)x + a\right)}{(x^2-1)} \tag{3.10}$$

Consider now the special parameter values $a = \pm a_{H_0} = \pm\left(1 - \frac{2}{3}b\right)$, where a_{H_0} is defined in (3.3) corresponding to the singular limit of the Hopf parameter value. For $a = a_{H_0}$ (similarly $a = -a_{H_0}$), the polynomial $p(x)$ (3.8) has a root at $x = 1$ (respectively $x = -1$), and by eliminating the term $(x - 1)$ (respectively $(x + 1)$) from the numerator and denominator of $\varphi(x)$ in (3.10), we can define

$$\varphi_{\pm H_0}(x) := -\frac{b}{3}x \mp \frac{a_{H_0}}{(x+1)} \tag{3.11}$$

as a reformulation of $\varphi(x)$ for $a = \pm a_{H_0}$, respectively. Notice that $\varphi_{+H_0}(x)$ (similarly $\varphi_{-H_0}(x)$) is defined for $x = 1$ (respectively $x = -1$).

For $a \neq \pm a_{H_0}$, the critical manifold of the JKE model, corresponding to the set of equilibria of (3.7), is given by

$$C_0 = \left\{(x, y) \in \mathbb{R}^2 : y = \varphi(x) = \frac{\left(-\frac{b}{3}x^3 + (b-1)x + a\right)}{(x^2 - 1)}\right\} \tag{3.12}$$

Since, the function φ has a pole at $x = \pm 1$, the curve C_0 has two vertical asymptotes given by $L_\pm = \{(x, y) \in \mathbb{R} | x = \pm 1\}$. Furthermore, the hyperbolicity of the equilibria along C_0 is determined by the sign of the nontrivial eigenvalue of (3.7) given by $\lambda_f = \partial_y \left(p(x) - (x^2 - 1)y\right) = 1 - x^2$. Hence, similar to the FHN model, the critical manifold of the JKE system has two stable branches over $x \in (-\infty, -1) \cup (1, \infty)$ and one unstable branch over $x \in (-1, 1)$. The three branches are separated by the two vertical lines $L_\pm$ corresponding to the non hyperbolicity of the critical manifold (since $\lim_{x \to \pm 1} \lambda_f = 0$).

Consider now the case $a = a_{H_0}$, since $p(1) = 0$, there is no vertical flow along the vertical line $L_+ = \{(x, y) \in \mathbb{R} | x = 1\}$ and all the points of L_+ are steady states in the JKE fast subsystem (3.7) with 0 eigenvalues (similar conclusion holds for $a = -a_{H_0}$ at $x = -1$). Therefore, the line L_+ becomes a part of the critical manifold C_0, which is non hyperbolic since $\lambda_f = 1 - x^2 = 0$. Furthermore, instead of being separated by the nonhyperbolicity asymptote L_+ for $a \neq a_{H_0}$, the right stable part and the unstable part of the critical manifold C_0 become connected via the point $(x_*, y_*) := (1, -\frac{1}{2}) \in L_+$. The point (x_*, y_*), corresponding to the intersection events of the hyperbolic and nonhyperbolic branches of the critical manifold for the spacial parameter value $a = a_{H_0}$, is described as a *non-generic branching point* [56]. Thus,

the critical manifold C_0 of the JKE system can be defined for $a = a_{H_0}$ as:

$$C_0 = \left\{(x, y) \in \mathbb{R}^2 : y = \varphi_{+H_0}(x)\right\} \cup L_+ \tag{3.13}$$

3.2.2 Slow subsystem

To analyse the slow flow of the FHN and JKE model, we rescale (2.30) and (2.29), respectively, by switching to the slow time scale $\tau = \varepsilon\, t$:

$$\begin{aligned} \varepsilon\, \dot{x} &= \left(z + x - \frac{x^3}{3}\right) \\ \dot{z} &= -\left(x - a + bz\right) \end{aligned} \tag{3.14}$$

$$\begin{aligned} \dot{x} &= y \\ \varepsilon\, \dot{y} &= \left(-\frac{b}{3}x^3 + (b-1)x + a\right) - \left(x^2 - 1 + \varepsilon b\right) y \end{aligned} \tag{3.15}$$

Setting $\varepsilon = 0$ in systems (3.14) and (3.15) leads to the FHN and JKE slow subsystems (reduced problems) given, respectively, by:

$$\begin{aligned} z - \left(\frac{x^3}{3} - x\right) &= 0 \\ \dot{z} &= a - x - bz \end{aligned} \tag{3.16}$$

$$\begin{aligned} \dot{x} &= y \\ \left(-\frac{b}{3}x^3 + (b-1)x + a\right) - \left(x^2 - 1\right) y &= 0 \end{aligned} \tag{3.17}$$

The algebraic equations in (3.16) and (3.17) are constrains determining the phase space of the FHN and JKE slow subsystems in the (x, z)- and (x, y)-planes, respectively. Since the algebraic equations in (3.16) and (3.17) lead to the critical manifolds S_0 and C_0, the differential equations in the FHN and JKE slow subsystems describe the flow on the critical manifolds S_0 and C_0, respectively. Furthermore, the flow of systems (3.16) and (3.17) can be parametrised by the variable x by combining the algebraic and differential equations in the slow subsystems. The combination eliminates the variables z and y from systems (3.16) and (3.17), respectively, and

leads to the one dimensional system:

$$\dot{x} = \varphi(x) = \frac{\left(-\frac{b}{3}x^3 + (b-1)x + a\right)}{(x^2-1)} \tag{3.18}$$

which describes the slow flow on both critical manifolds S_0 and C_0. To analyse the steady state of (3.18), we consider the case $0 < b < 1$ corresponding to a unique equilibrium for the FHN and JKE models (see the discussion in 2.2.1.1). The polynomial p has only one root [41], therefore, system (3.18) (and hence the FHN and JKE slow subsystems) has a unique equilibrium of stability determined by the eigenvalue $\lambda_s = \partial_x\varphi(x) = \frac{1}{(1-x^2)} - b$. Hence, the stability depends on the part of the critical manifold (S_0 or C_0) to which the equilibrium belongs.

In the parameter range $a \in (-a_{H_0}, a_{H_0})$, the equilibrium lies in the middle part of the critical manifold defined on $x \in (-1, 1)$. Since $0 < b < 1$, the corresponding eigenvalue is positive ($\lambda_s > 0$), hence, the equilibrium is unstable. Whereas, for $a < -a_{H_0}$ and $a > a_{H_0}$, the x-coordinate of the equilibrium satisfy $x < -1$ and $x > 1$ corresponding to the left and right parts of the critical manifold, respectively. The equilibrium is stable since the corresponding eigenvalue is negative ($\lambda_s < 0$). Moreover, for all cases $a \neq \pm a_{H_0}$, equation (3.18) has singularity at $x = \pm 1$ (corresponding to the fold points of S_0 and the asymptotes of C_0), for which the flow is undefined. Hence, we conclude that the FHN and JKE slow subsystems share the same flow properties along the three hyperbolic branches of the critical manifolds for $a \neq \pm a_{H_0}$.

However, differences can be noticed for the cases $a = \pm a_{H_0}$. Consider $a = a_{H_0} = \left(1 - \frac{2}{3}b\right)$ (similar result holds for $a = -a_{H_0}$), the root of the polynomial $p(x)$ is $x = 1$. Therefore, by eliminating the term $(x-1)$ from the numerator and denominator of $\varphi(x)$ in (3.18), the slow flow can be reformulated as:

$$\dot{x} = \varphi_{H_0}(x) = \frac{\left(-\frac{b}{3}x^2 - \frac{b}{3}x - a_{H_0}\right)}{(x+1)} \tag{3.19}$$

which has singularity only at $x = -1$. Hence, for $a = a_{H_0}$ and $0 < b < 1$, the system (3.18) is desingularized at $x = 1$ since the equilibrium collides with the singularity and disappears giving existence to a special solution of (3.18) defined for $x \in (-1, \infty)$ that passes through $x = 1$ with a non-trivial flow given by $\varphi_{H_0}(1) = -\frac{1}{2}$.

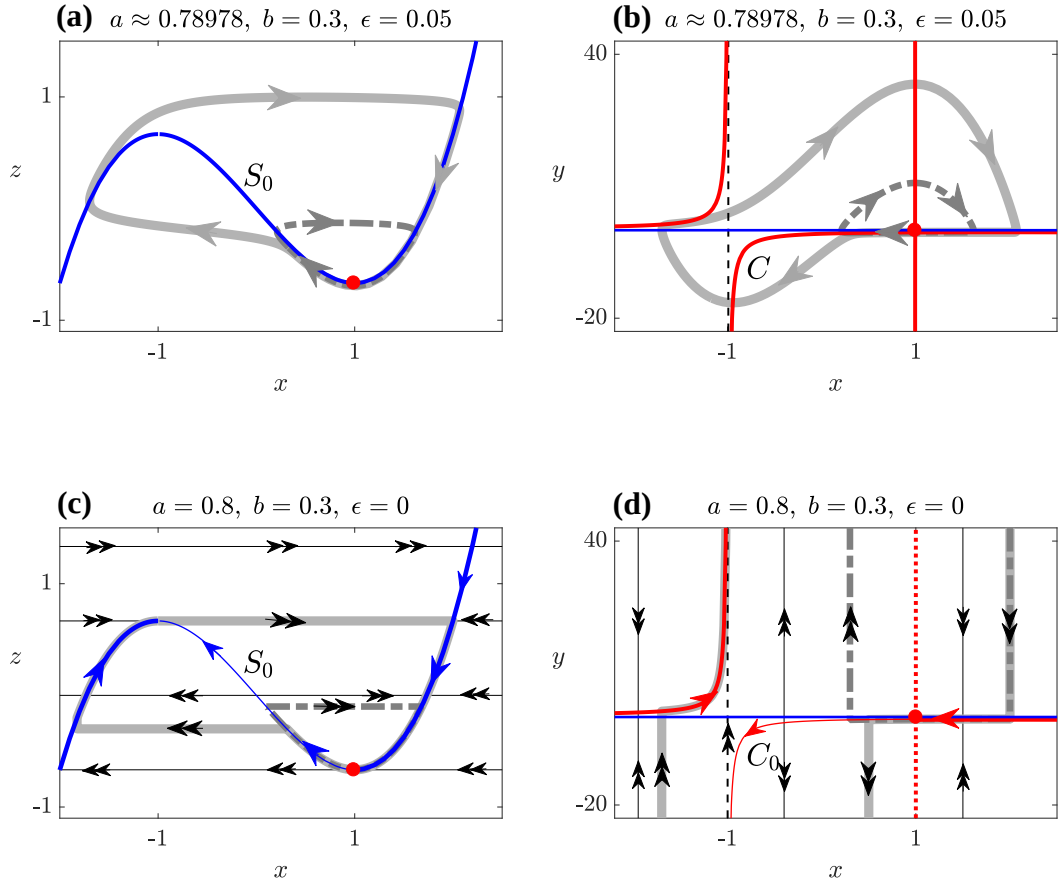

Figure 3.2: Canard and singular canard cycles of the FHN and JKE models. Panels **a**) and **b**): small and large canard cycles for $\varepsilon = 0.05$ of the FHN and JKE systems, respectively. Panels **c**) and **d**): singular canard cycles in the singular limit $\varepsilon = 0$ defined as a connection of solution segments of the slow and fast subsystems of the FHN and JKE, respectively, for $a = a_{H_0}$. (*Dark/light gray line* for small/large canard and singular canard cycles, respectively; *blue/red lines* indicate the critical manifold of the FHN/JKE systems, respectively, (*thick* attractive branch, *thin* repelling branch); *red dotted line* for nonhyperbolic branch L_+ of C_0 with no vertical flow; *solid black lines* indicate the layers of the fast subsystems; *dashed black lines* for asymptotes of the critical manifold C_0 of the JKE system; ; *single/double arrows* describe the flow of the slow/fast subsystems, respectively; *red dot* for the unstable equilibrium of the full system ($\varepsilon > 0$) and the desingularized point of the slow subsystem ($\varepsilon = 0$), respectively.

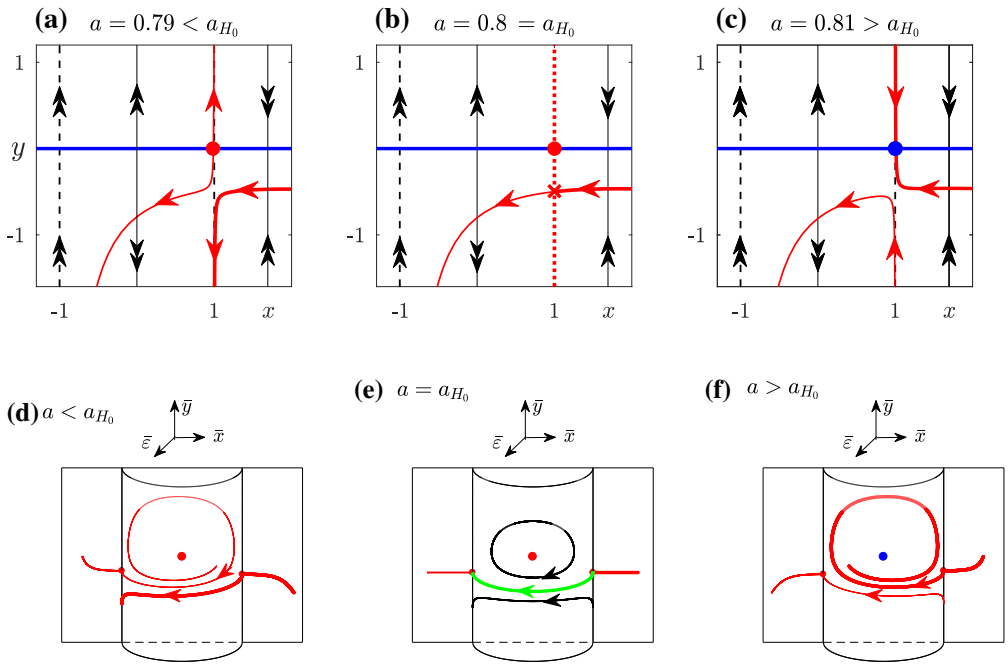

Figure 3.3: Blowing-up of the non-generic branching point of C_0. Panels **a-c** the local dynamics of the JKE system (3.15) near the equilibrium; Panels **d-f** the local dynamics after blowing-up the nonhyperbolic branch L_+ to the cylinder $\mathcal{C}$. For all panels $b = 0.3$. *Red lines* the critical manifold C_0 (*thick* attractive branch, *thin* repelling branch and *dotted* for L_+); *blue line* the x-nullcline; *thick black lines* transient solutions; *single arrow* slow flow on the critical manifold C_0 and *double arrow* fast flow on the layers; *blue/red dots* for stable/unstable node; *red cross* the non-generic branching point $(x, y) = (1, -1/2)$; *green curve* for the special solution γ_c connecting the slow flow from the attracting to the repelling parts of C_0 at $a = a_{H_0} = 0.8$.

The geometric mechanisms in the state space leading to the desingularization of the critical manifold of FHN and JKE slow subsystem at the nonhyperbolicity are different. While the equilibrium of the FHN slow subsystem (3.16) collides with and desingularizes the fold point $(x, z) = (1, -\frac{2}{3})$ of the critical manifold S_0 as $a \to a_{H_0}$, the equilibrium of the JKE slow subsystem (3.17) collides with and desingularizes the non-generic branching point $(x, y) = (1, -\frac{1}{2})$ of the critical manifold C_0 as $a \to a_{H_0}$. Thus, the special solution connecting the right part of the critical manifold to the middle part passes through the desingularized fold point of S_0 in the FHN slow subsystem (3.16) and through the non-generic branching point of C_0 in the JKE slow

subsystem (3.17) with nontrivial flow. Figure 3.3 illustrates the desingularization mechanism of the JKE slow flow for $a = a_{H_0}$, which is one of the features organising canard solutions in the JKE system that are different from the classical FHN system.

3.2.3 Singular canard cycles

Fenichel's Theorem A.1 guarantees that for sufficiently small ε, normally hyperbolic parts of the critical manifold (S_0 or C_0) perturb to nearby invariant slow manifolds (S_ε or C_ε) of the FHN (3.14) and JKE (3.15) systems, respectively, with slow flow that can be approximately described by (3.18) [50, 62, 65–67]. In addition, if the Fenichel's Theorem fails due to nonhyperbolicity on the critical manifold, the blow-up technique might be used to regain sufficient local hyperbolicity that allows Fenichel's Theorem to be applied.

Furthermore, by combining solutions of the fast and slow subsystems, the canard cycles in the FHN (3.14) and JKE (3.15) systems can be considered as a perturbation of the so-called *singular canard cycles*. A singular canard cycle is a sequence of trajectory solutions of the fast and slow subsystems that collectively form a singular approximation of a canard cycle in the phase space. The singular canard cycles have to contain partially the special solution (defined for $a = a_{H_0}$) which passes through the desingularized point connecting the stable and unstable parts of the critical manifold [50, 64]. Hence, for sufficiently small $\varepsilon > 0$, the canard cycles are perturbations of singular canard cycles defined at $\varepsilon = 0$, as they both exist within $\mathcal{O}(\varepsilon)$ Hausdorff distance in the phase space according to Fenichel's Theorem [50, 64].

Moreover, a canard cycle of the FHN system (3.14) are commonly classified as canard without head (small canard) and canard with head (large canard) if, after leaving the vicinity of the unstable slow manifold in the (x, z)-plane, it jumps to the right, respectively the left, as it becomes attracted to the right, respectively the left, stable slow manifold [50, 51, 64]. Similarly, we can classify the canard cycles of the JKE system (3.14). We refer to a canard cycle as small, respectively large, if, after leaving the vicinity of the unstable slow manifold in the (x, y)-plane, it jumps up, respectively down, then returns towards the right, respectively the left, stable slow manifold.

The dynamics of fast and slow subsystems and the properties of singular canard

orbits explain the different organisation and features of canard solutions between the FHN and JKE models. Furthermore, for $\varepsilon > 0$, the canard cycles follow a slow manifold that perturbs from the critical manifold, according to Fenichel's Theorem. Therefore, the vital role in organising canard cycles of the FHN and JKE systems via the singular canard cycles is played by the critical manifolds.

In Figure 3.2, we illustrate examples of canard and singular canard cycles of the FHN (3.14) and JKE (3.15) systems. Panels (**a**) and (**b**) show examples of small and large canard cycles of the FHN and JKE models, respectively, for $\varepsilon = 0.05$. Panels (**c**) and (**d**) illustrate the corresponding singular canard cycles in addition to the fast and slow flow of the FHN and JKE subsystems at $\varepsilon = 0$. The fast flow of the layer problem follows the direction of the fast variable, which is x in the FHN system (3.14) and y in the JKE system (3.15). The fast flow is tangent to the nonhyperbolic fold points of the critical manifold S_0 of the FHN system, while for the JKE system, the tangency of the fast flow to the critical manifold C_0 occurs at infinity.

Considering the singular canard cycles attracted, via fast layer flow, to the right stable part of the critical manifold, the cycle then follows the slow flow until passing from the right stable part to the middle unstable part via the desingularized point (fold for the FHN system and non-generic branching for the JKE system). Then the singular canard cycle follows the slow flow on the unstable part of the critical manifold before being repelled to follow fast flow along an invariant layer; In the FHN system, the singular canard cycle is small if it is repelled toward and ends in the right stable part of the critical manifold; and it is large if it is repelled to the left and follow the slow flow on the left stable part until reaching the nonhyperbolic fold of the critical manifold at $x = -1$, then follows fast flow along the layer that is tangent to the nonhyperbolic fold and ends in the right stable part (see Figure 3.2 panel (**c**)); For the JKE system, however, the singular canard cycle is small if it is repelled up along fast flow layer toward $y = +\infty$, then returns back along another layer to end in the right stable part of the critical manifold; and it is large if it is repelled down along fast flow layer toward $y = -\infty$, then returns back along another layer toward the left stable part of the critical manifold, then follows the slow flow on the stable part until becoming tangent to the nonhyperbolic asymptote $x = -1$ of C_0 at $y = \infty$, then returns back along fast flow layer to end in the right stable

part of the critical manifold (see Figure 3.2 panel (**d**)). By comparing the singular canards of the JKE system (panel **d**) to the corresponding singular canard cycles of the FHN system (panel **c**), we can conclude that the small singular canard cycles returns to the right stable part of the critical manifold for $1 < x < 2$. Whereas, the large singular canard cycles returns to the left stable part for $-2 < x < -1$ and to the right stable part at $x = 2$. The returning mechanism from infinity is discussed in 3.2.5.

From the previous discussion, we can observe two key features that characterise the singular canard cycles of the JKE system (3.15) and lead to the different organisation of canard cycles, compared to the FHN system (3.14). The first feature is the flat slow flow of the JKE system through the desingularized non-generic branching point of the critical manifold C_0, which is perpendicular to the layer of the fast system, unlike the slow flow through the desingularized fold of the FHN system which is parallel to the fast layers. The other characteristic feature is the departure of the fast flow of the JKE system to and the returning from infinity along vertical layers. In the following, we analyse further these two features using blow-up technique and projection on Poincaré sphere.

3.2.4 Behaviour of canard solutions near the nonhyperbolicity

In this part, we analyse the behaviour of canard cycles near the self-intersection nonhyperbolicity of the critical manifold C_0 of the JKE system (3.15). It follows from Fenichel's Theorem A.1 that the attracting and repelling branches of the critical manifold C_0 of the JKE system perturb smoothly to locally invariant manifolds C_ε for sufficiently small $0 < \varepsilon \ll 0$. However, in a small neighbourhood of the nonhyperbolic branching point of C_0, Fenichel's theory can no longer be applied. In this case, we can use the blow-up technique to insert a suitable cylindrical manifold at the singularity to restore enough hyperbolicity and allow for a complete analysis of the local dynamics by standard dynamical systems techniques.

To this end, we follow [66] and consider the extended system:

$$\begin{aligned} x' &= \varepsilon\, y \\ y' &= \left(-\frac{b}{3}x^3 + (b-1)x + a\right) - \left(x^2 - 1 + \varepsilon b\right) y \\ a' &= 0 \\ \varepsilon' &= 0 \end{aligned} \tag{3.20}$$

System (3.20) has Hopf bifurcation point at $(x, y, a, \varepsilon) = (1, 0, a_{H_0}, 0)$. Using the change of variable $x_{old} \to x_{new}+1$ and introducing the control parameter $\lambda = a - a_{H_0}$ lead to the system

$$\begin{aligned} x' &= \varepsilon\, y \\ y' &= \lambda - \left(x + bx^2 + \frac{b}{3}x^3\right) - (b\varepsilon + 2x + x^2)y \\ \lambda' &= 0 \\ \varepsilon' &= 0 \end{aligned} \tag{3.21}$$

which has Hopf bifurcation point at $(x, y, \lambda, \varepsilon) = (0, 0, 0, 0)$. The right hand side of (3.21) is *quasihomogeneous* of type $(1, 0, 1, 2)$ (see B.1.3), which allows us to define the cylindrical blow-up transformation $\Phi_{\mathcal{C}} : B_{\mathcal{C}} \to \mathbb{R}^4$:

$$\Phi_{\mathcal{C}}(\bar{x}, \bar{y}, \bar{\lambda}, \bar{\varepsilon}, \bar{r}) = (\bar{r}\bar{x}, \bar{y}, \bar{r}\bar{\lambda}, \bar{r}^2\bar{\varepsilon}) = (x, y, \lambda, \varepsilon) \tag{3.22}$$

with weights $(1, 0, 1, 2)$, where $B_{\mathcal{C}} = \mathcal{C}^4 \times [0, \rho]$. Here the y-axis is blown-up by $\Phi_{\mathcal{C}}$ to a 4-cylinder $\mathcal{C}^4 = \mathcal{S}^3 \times \mathbb{R}$, where $\mathcal{S}^3$ is determined by

$$\bar{x}^2 + \bar{\lambda}^2 + \bar{\varepsilon}^2 = 1, \qquad \bar{\varepsilon} \geq 0 \tag{3.23}$$

To have a complete picture of the local dynamics on the blown-up cylinder, we consider three charts K_1, K_2 and K_3. The dynamics on the charts K_1, K_2 and K_3 are projection of the local dynamics of the blown-up cylinder $\mathcal{C}^4$ onto the three tangent hyperplanes at $\bar{x} = 1$, $\bar{\varepsilon} = 1$ and $\bar{x} = -1$, respectively. The dynamics on charts K_1 and K_3 can be defined by setting $\bar{x} = x_1 = 1$ and $\bar{x} = x_3 = -1$,

respectively, in (3.21). The dynamics of these two charts give information about the flow-in and -out from the blown-up cylinder $\mathcal{C}^4$ to the local neighborhood of the y-axis. For chart K_2, we set $\bar{\varepsilon} = \varepsilon_2 = 1$ in (3.21). The phase plane for K_2 describes the intermediate flow on the blown-up cylinder $\mathcal{C}^4$.

Chart K_2

We begin with the dynamics on chart K_2, for which we set $\varepsilon_2 = 1$:

$$K_2 : \quad x = r_2 x_2, \quad y = y_2, \quad \lambda = r_2 \lambda_2, \quad \varepsilon = r_2^2 \tag{3.24}$$

Since $r_2 = \sqrt{\varepsilon}$, the blow-up transformation on chart K_2 is just a rescaling of (3.21). Substituting (3.24) and desingularising the vector field by the time-rescaling $t_2 = r_2 t$ leads to the system:

$$\begin{aligned} \frac{dx_2}{dt_2} &= y_2 \\ \frac{dy_2}{dt_2} &= \lambda_2 - x_2(1 + 2y_2) + \mathcal{O}(r_3) \\ \frac{d\lambda_2}{dt_2} &= 0 \end{aligned} \tag{3.25}$$

Considering $r_2 = 0$, the system takes the form

$$\begin{aligned} \frac{dx_2}{dt_2} &= y_2 \\ \frac{dy_2}{dt_2} &= \lambda_2 - x_2(1 + 2y_2) \end{aligned} \tag{3.26}$$

which has an equilibrium at $(x_2, y_2) = (\lambda_2, 0)$. The linearisation of (3.26) at the equilibrium has the eigenvalues $-\lambda_2 \pm i\sqrt{1 - \lambda_2^2}$, therefore, the equilibrium is stable for $\lambda_2 \in (0, 1)$ and unstable for $\lambda_2 \in (-1, 0)$ [Notice that following the results of TheoremsA.2-A.3 and the transformation (3.24), we are interested in a parameter neighborhood of $\lambda_2 = 0$ of order $\mathcal{O}(\sqrt{\varepsilon})$]. For $\lambda_2 = 0$, the system (3.26) is integrable with a constant of motion given by:

$$H(x_2, y_2) = \frac{1}{2}\left(x^2 + y - \ln(|1 + 2y|)\right) \tag{3.27}$$

Four types of phase portraits exists on chart K_2 for $\lambda_2 = 0$, the equilibrium $(0, 0)$ of center type, a family of bounded periodic orbits surrounding the equilibrium in the half plane $y > -\frac{1}{2}$, a family of unbounded trajectories in the half plane $y < -\frac{1}{2}$ and a special solution:

$$\gamma_c\left(x_2(t_2), y_2(t_2)\right) = \left(-\frac{t_2}{2}, -\frac{1}{2}\right) \tag{3.28}$$

that separates the family of bounded periodic orbits from the family of unbounded trajectories. The strait line trajectory γ_c, defined for $\lambda_2 = 0$, is of special importance for our analysis as it connects the three charts together (as we will discuss later). For $\lambda_2 \neq 0$, the special solution and the periodic orbits break as the equilibrium becomes node and all the trajectories in the phase space of chart K_2 become unbounded.

Chart K_1

For chart K_1, we set:

$$K_1: \quad x = r_1, \quad y = y_1, \quad \lambda = r_1\lambda_1, \quad \varepsilon = r_1^2\varepsilon_1 \tag{3.29}$$

We substitut (3.29) in (3.21) and desingularise the vector field by dividing the equations by r_1 and rescale the time variable. This will lead to the system:

$$\begin{aligned}
\frac{dr_1}{dt_1} &= r_1\varepsilon_1\, y_1 \\
\frac{dy_1}{dt_1} &= \lambda_1 - (1 + 2y_1) + \mathcal{O}(r_1) \\
\frac{d\lambda_1}{dt_1} &= -\lambda_1\varepsilon_1 y_1 \\
\frac{d\varepsilon_1}{dt_1} &= -2\varepsilon_1^2 y_1
\end{aligned} \tag{3.30}$$

Where t_1 denotes to the rescaled time variable. System (3.30) has the invariant subspaces $r_1 = 0$ and $\lambda_1 = 0$. In the invariant plane $r_1 = \lambda_1 = 0$ system (3.30) reduces to

$$\begin{aligned}
\frac{dy_1}{dt_1} &= (1 + 2y_1) \\
\frac{d\varepsilon_1}{dt_1} &= -2\varepsilon_1^2 y_1
\end{aligned} \tag{3.31}$$

which has an equilibrium at $(y_1, \varepsilon_1) = \left(-\frac{1}{2}, 0\right)$. The linearisation of (3.31) at the equilibrium has the eigenvalues -2 and 0, therefore, the equilibrium is of saddle-node type. Furthermore, in a small neighborhood of the equilibrium, the flow in the y_1 direction is $\frac{dy_1}{dt_1} < 0$ for $y > -\frac{1}{2}$ and $\frac{dy_1}{dt_1} > 0$ for $y < -\frac{1}{2}$, hence, the equilibrium is attracting at the y_1-axis. In addition, the flow in the ε_1 direction is $\frac{d\varepsilon_1}{dt_1} > 0$ for $\varepsilon_1 > 0$. Whereas, there is no flow in the ε_1 direction along the y_1-axis, which means that the slow flow can only inter to chart K_1 and the blown up cylinder via the equilibrium $(y_1, \varepsilon_1) = \left(-\frac{1}{2}, 0\right)$.

Moreover, the equilibrium $(y_1, \varepsilon_1) = (-\frac{1}{2}, 0)$ corresponds to the intersection of the attracting branch of the critical manifold C_0 to the blown-up cylinder (corresponding to the nonhyperbolic branch L_+) at the non-generic branching point.

Chart K_3

Similarly, for chart K_3, we set:

$$K_3 : \quad x = -r_3, \quad y = y_3, \quad \lambda = r_3\lambda_3, \quad \varepsilon = r_3^2\varepsilon_3 \tag{3.32}$$

We substitut (3.32) in (3.21) and desingularise the vector field by dividing the equations by r_3 and rescale the time variable. This will lead to the system:

$$\begin{aligned} \frac{dr_3}{dt_3} &= -r_3\varepsilon_3\, y_3 \\ \frac{dy_3}{dt_3} &= \lambda_3 + (1 + 2y_3) + \mathcal{O}(r_3) \\ \frac{d\lambda_3}{dt_3} &= \lambda_3\varepsilon_3 y_3 \\ \frac{d\varepsilon_3}{dt_3} &= 2\varepsilon_3^2 y_3 \end{aligned} \tag{3.33}$$

Where t_3 denotes to the rescaled time variable. System (3.33) has the invariant subspaces $r_3 = 0$ and $\lambda_3 = 0$. In the invariant plane $r_3 = \lambda_3 = 0$ system (3.33) reduces to

$$\begin{aligned} \frac{dy_3}{dt_3} &= (1 + 2y_3) \\ \frac{d\varepsilon_3}{dt_3} &= 2\varepsilon_3^2 y_3 \end{aligned} \tag{3.34}$$

which has an equilibrium at $(y_3, \varepsilon_3) = \left(-\frac{1}{2}, 0\right)$. The linearisation of (3.34) at the equilibrium has the eigenvalues 2 and 0, therefore, the equilibrium is of saddle-node type. Furthermore, in a small neighbourhood of the equilibrium, the flow in the y_1 direction is $\frac{dy_3}{dt_3} > 0$ for $y > -\frac{1}{2}$ and $\frac{dy_3}{dt_3} < 0$ for $y < -\frac{1}{2}$, hence, the equilibrium is repelling at the y_1-axis. In addition, the flow in the ε_3 direction is $\frac{d\varepsilon_3}{dt_3} < 0$ for $\varepsilon_3 > 0$. Whereas, there is no flow in the ε_3 direction along the y_3-axis, which means that the slow flow can only exit from chart K_3 and the blown up cylinder via the equilibrium $(y_3, \varepsilon_3) = \left(-\frac{1+\lambda_3}{2}, 0\right)$.

Moreover, the equilibrium $(y_3, \varepsilon_3) = (-\frac{1}{2}, 0)$ corresponds to the intersection of the repelling branch of the critical manifold C_0 to the blown-up cylinder (corresponding to the nonhyperbolic branch L_+) at the non-generic branching point.

Combining information from the charts

The slow flow on the blown-up manifold and its connection to the cylinder neighborhood can be understood from combining the information about the dynamics on the charts K_1, K_2 and K_3 as illustrated in Figure 3.3.

The change of coordinates from K_1 to K_2 is given by:

$$x_2 = \varepsilon_1^{-\frac{1}{2}}, \quad y_2 = y_1, \quad r_2 = \varepsilon_1^{\frac{1}{2}} r_1, \quad \lambda_2 = \varepsilon_1^{-\frac{1}{2}} \lambda_1, \qquad \text{for } \varepsilon_1 > 0 \tag{3.35}$$

Similarly, the change of coordinates from K_3 to K_2 is given by:

$$x_2 = -\varepsilon_3^{-\frac{1}{2}}, \quad y_2 = y_3, \quad r_2 = \varepsilon_3^{\frac{1}{2}} r_3, \quad \lambda_2 = \varepsilon_3^{-\frac{1}{2}} \lambda_3, \qquad \text{for } \varepsilon_3 > 0 \tag{3.36}$$

The slow flow can only enter and exit the blown-up cylinder via the equilibria of the the charts K_1 and K_3 which connect the blown-up cylinder to the attracting and repelling parts of the critical manifold C_0. For $\lambda = 0$ ($a = a_{H_0}$), the inter equilibrium of chart K_1 is connected to the exit equilibrium of chart K_3 by the special solution γ_c in the chart K_2 (see Figure 3.3 **e**). This connection breaks for $\lambda \neq 0$ ($a \neq a_{H_0}$) as the slow flow entering via the chart K_1 diverges to $y_2 = -\infty$ or converges to the equilibrium of chart K_2. (see Figure 3.3 **d** and **f**). Therefore, the trajectory γ_c, depicted in green line in Figure 3.3 **e**, can be considered as an extension of the non-generic branching point of C_0 along the blown-up cylinder which connects the

attracting and repelling parts of the critical manifold. This connection explains the local behaviour of the canard cycles of the JKE system near the nonhyperbolicity of the critical manifold C_0.

3.2.5 Behaviour of canard solutions near infinity

In this part, we investigate the global behaviour of canard cycles of the JKE model in the singular case $\varepsilon = 0$. By projecting the flow of the JKE fast and slow subsystems on the Poincaré sphere and applying the blow-up technique, we offer an explanation of the return mechanism organising the singular canard cycles near infinity. The results of this part have been submitted and accepted for publication [60].

We follow [54] and apply the definitions and theorems in B.2. Let:

$$\begin{aligned} P(x,y) &= \epsilon y \\ Q(x,y) &= \left(-\frac{b}{3}x^3 + (b-1)x + a\right) - \left(x^2 - 1 + \epsilon b\right) y \end{aligned} \tag{3.37}$$

Since P and Q are polynomials of degrees 1 and 3, respectively, the leading homogeneous polynomials have to be of degree $m = 3$. Using the transformation of variables $(x,y) \to \left(\frac{X}{Z}, \frac{Y}{Z}\right)$ the the leading homogeneous polynomials are:

$$\begin{aligned} P_*(X,Y,Z) &= Z^3\, P_*(X/Z, Y/Z) = \epsilon Y Z^2 \\ Q_*(X,Y,Z) &= Z^3\, Q_*(X/Z, Y/Z) \\ &= \left(-\frac{b}{3}X^3 + (b-1)XZ^2 + aZ^3\right) - \left[X^2 - (1-\epsilon b)Z^2\right] Y \\ &= -X^2\left(\frac{b}{3}X + Y\right) + Z^2\left[(b-1)X + (1-\epsilon b)Y\right] + aZ^3 \end{aligned} \tag{3.38}$$

The projection of the critical manifold is given by:

$$\frac{Y}{Z} = \varphi\left(\frac{X}{Z}\right) := \frac{\left(-\frac{b}{3}\left(\frac{X}{Z}\right)^3 + (b-1)\left(\frac{X}{Z}\right) + a\right)}{\left(\left(\frac{X}{Z}\right)^2 - 1 + \epsilon b\right)} \tag{3.39}$$

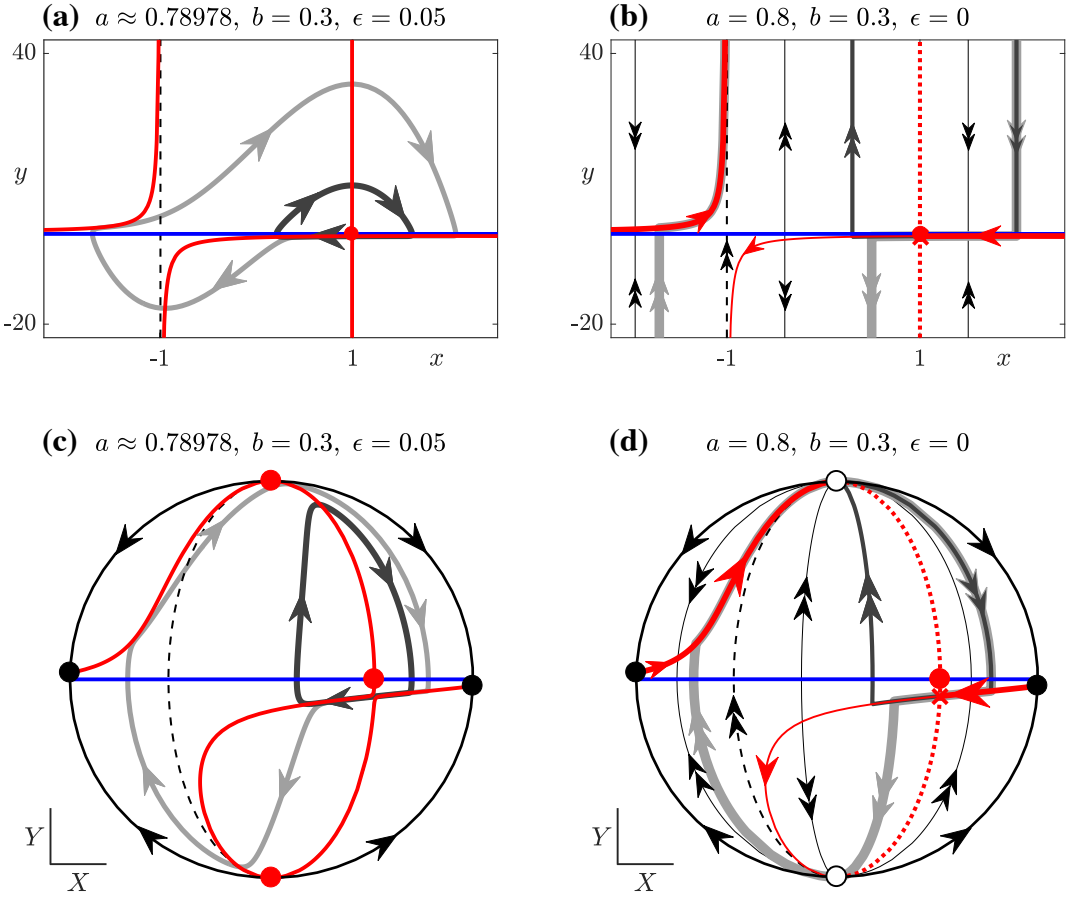

Figure 3.4: Global phase portraits of the JKE system (3.7)**.** Panel(**a**) shows the phase portraits for $\varepsilon > 0$; panel(**b**) Slow and fast flow for $\varepsilon = 0$. panel(**c**) and (**d**) illustrate projections of the phase space shown in panels (**a**) and (**b**), respectively, onto the upper Poincré hemisphere ($Z \geq 0$). *Red* indicate the y-nullcline in panels(**a**) and (**c**), and the critical manifold C_0 in panels(**b**) and (**d**) (*thick* for attracting branch, *thin* for repelling branch and *dotted* for zero vertical flow on the nonhyperbolic branch L_+); *blue* the x-nullcline; *dark/light grey* for small/large canard cycles, respectively, for $\varepsilon > 0$ or small/large singular canard cycles, respectively, for $\varepsilon = 0$; *thin black* for the layers of the fast subsystem; *single arrow* slow flow on the critical manifold C_0 and *double arrow* fast flow on the layers; *black dashed* asymptotes of the critical manifold C_0; *thick black* indicates the equator of the Poincaré sphere; *red dot* for unstable node; *black dot* for saddle point; *black and white dot* non-hyperbolic node; *red cross* for the non-generic branching point.

Hence, by Theorem B.1, the flow on the equator (for $Z = 0$) is determined by:

$$G(X, Y) = X\, Q_*(X, Y, 0) - Y\, P_*(X, Y, 0) = -X^3 \left(\frac{b}{3} X + Y\right) \tag{3.40}$$

Solving $G(X,Y)=0, X^2+Y^2=1$ on the equator $Z=0$ leads to the four critical points

$$\begin{aligned} X &= 0, & Y &= \pm 1; \\ X &= \pm\frac{3}{\sqrt{9+b^2}}, & Y &= \mp\frac{b}{\sqrt{9+b^2}}, \end{aligned}$$

the flow between the critical points is determined by the sign of (3.40). For $\varepsilon > 0$, the two points $X = 0$ are unstable nodes, and the two points $X \neq 0$ are saddles. However, in the singular case $\varepsilon = 0$ and for $a = a_{H_0}$, the two points at $X = 0$ become non-hyperbolic nodes; these two nodes on the equator, namely, $(0, \pm 1)$, provide return mechanism for the unbounded segments of the singular canards. The projection of JKE flow on the Poincaré hemisphere $Z \geq 0$ is shown in Figure 3.4. The phase portrait on the lower hemisphere, for $Z \leq 0$, are symmetric to the upper hemisphere across the centre of the sphere. However, the flow on the upper hemisphere $Z \geq 0$ is sufficient for our analysis. We investigate the local dynamic near the nonhyperbolic points $(0, \pm 1, 0)$ in order to understand the return mechanism of the singular canard cycles for $\varepsilon = 0$. To this end, we project the flow on the hemisphere $Z > 0$ onto the plane tangent to the sphere at the points $(X, \pm 1, Z)$.

Fast flow

From Theorem B.2, the flow behaviour of the JKE model in the neighbourhood of $(0, \pm 1, 0)$ is equivalent to the behaviour of the system:

$$\begin{aligned} \pm X' &= -XQ_*(X, \pm 1, Z) + P_*(X, \pm 1, Z), \\ \pm Z' &= -ZQ_*(X, \pm 1, Z) \end{aligned} \tag{3.41}$$

or

$$\begin{aligned} \pm X' &= -X\left[\left(-\frac{b}{3}X^3 + (b-1)XZ^2 + aZ^3\right) \mp \left[X^2 - (1-\epsilon b)Z^2\right]\right] \pm \epsilon Z^2 \\ \pm Z' &= -Z\left[\left(-\frac{b}{3}X^3 + (b-1)XZ^2 + aZ^3\right) \mp \left[X^2 - (1-\epsilon b)Z^2\right]\right] \end{aligned} \tag{3.42}$$

with respective sign determined by the flow on the equator, described by (3.40). Since for the fast subsystem we have $\varepsilon = 0$ and $P_* = 0$, system (3.41) is separable, and leads to the equation $dZ/dX = Z/X$ with solution $Z = CX$ for $C \in \mathbb{R}$.

Therefore, the flow in the neighbourhood of the non-hyperbolic nodes $(0, \pm 1, 0)$ has only radial direction.

To investigate further the dynamics near the projected nonhyperbolic nodes $(0, \pm 1, 0)$, and to understand how they can be attracting and repelling at the same time we use polar blow-up transformation [68].

$$\Phi : (X, Z) \to (r\bar{X}, r\bar{Z}) = (r\cos(\theta), r\sin(\theta)) \tag{3.43}$$

where $(\theta, r) \in [0, 2\pi) \times [0, r_0]$ for some $r_0 > 0$, which replaces the nonhyperbolic equilibrium $(X, Z) = (0, 0)$ with a unit circle $\mathcal{S}^1 \times \{r = 0\}$, where

$$\mathcal{S}^1 := \{(\bar{X}, \bar{Z}) \in \mathbb{R}^2 : \bar{X}^2 + \bar{Y}^2 = 1\}$$

and topologically conjugates the dynamics between

$$\mathbb{R}^2 \backslash (0, 0) \qquad \text{and} \qquad \mathcal{S}^1 \times (0, r_0]$$

The transformation Φ leads to:

$$\begin{aligned} X' &= \bar{X}\ r' - \bar{Z}\ r\theta' \\ Z' &= \bar{Z}\ r' + \bar{X}\ r\theta' \end{aligned} \tag{3.44}$$

which can be solved for r' and θ' to obtain the dynamics in $\bar{X}\bar{Z}$-plane as:

$$\begin{aligned} r' &= \ \ \bar{X}\ \dot{X} + \bar{Z}\ \dot{Z} \\ r\ \theta' &= -\bar{Z}\ \dot{X} + \bar{X}\ \dot{Z} \end{aligned} \tag{3.45}$$

and from (3.41) we have

$$\begin{aligned} r' &= \ \ \bar{X}\left[-XQ_*(X, 1, Z)\right] + \bar{Z}\left[-ZQ_*(X, 1, Z)\right] \\ r\ \theta' &= -\bar{Z}\left[-XQ_*(X, 1, Z)\right] + \bar{X}\left[-ZQ_*(X, 1, Z)\right] \end{aligned} \tag{3.46}$$

or

$$\begin{aligned} r' &= \ -\left(\bar{X}^2 + \bar{Z}^2\right) rQ_*(X, 1, Z) \\ r\ \theta' &= \left(-\bar{X}\bar{Z} + \bar{X}\bar{Z}\right) rQ_*(X, 1, Z) \end{aligned} \tag{3.47}$$

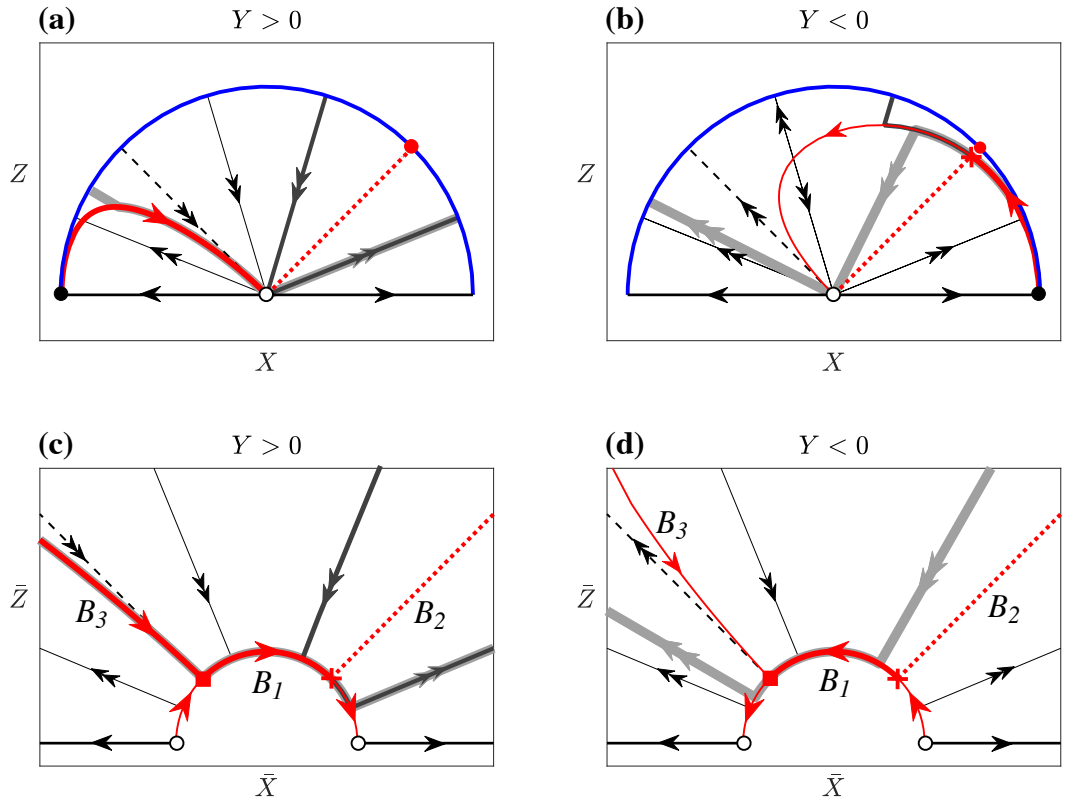

Figure 3.5: Projection and blow-up of the JKE dynamics near infinity for $a = a_{H_0}$, $b = 0.3$ and $\varepsilon = 0$. **a**) and **b**) the flow projected on $(X, 1, Z)$ and $(X, -1, Z)$, respectively. **c**) and **d**) dynamics near the blown-up circle for $(0, 1, 0)$ and $(0, -1, 0)$, respectively. Color coding as in Fig. 3.4.

Hence

$$\begin{aligned} r' &= -rQ_*(X, 1, Z) \\ r\,\theta' &= 0 \end{aligned} \tag{3.48}$$

$$\begin{aligned} r' &= \left(\bar{X}^2 - \bar{Z}^2\right) r^3 - \left(-\frac{b}{3}\bar{X}^3 + (b-1)\bar{X}\bar{Z}^2 + a_{H_0}\bar{Z}^3\right) r^4 \\ \theta' &= 0 \end{aligned} \tag{3.49}$$

System (3.49) has an entire circle of nonhyperbolic steady states given by $\mathcal{S}^1 \times \{r = 0\}$, see panels (**c-d**) in Figure 3.5. The hyperbolicity of the steady states can be regained, without changing the the qualitative structure of the vector field on the set $\mathcal{S}^1 \times (0, r_0])$, by dividing the equations by r^2 and rescale the time variable.

The resulting system is

$$\begin{aligned} r' &= \left(\bar{X}^2 - \bar{Z}^2\right) r - \left(-\frac{b}{3}\bar{X}^3 + (b-1)\bar{X}\bar{Z}^2 + a_{H_0}\bar{Z}^3\right) r^2 \\ \theta' &= \qquad 0 \end{aligned} \tag{3.50}$$

which has two equilibria for each angle θ; the first is $r = 0$, corresponding to the points on the blown-up circle $\bar{X}^2 + \bar{Z}^2 = 1$; while, the second equilibrium is given by:

$$\begin{aligned} r &= \frac{\left(\bar{X}^2 - \bar{Z}^2\right)}{\left(-\frac{b}{3}\bar{X}^3 + (b-1)\bar{X}\bar{Z}^2 + a_{H_0}\bar{Z}^3\right)} \\ &= \frac{\bar{Z}^2\left(\left(\frac{\bar{X}}{\bar{Z}}\right)^2 - 1\right)}{\bar{Z}^3\left(-\frac{b}{3}\left(\frac{\bar{X}}{\bar{Z}}\right)^3 + (b-1)\left(\frac{\bar{X}}{\bar{Z}}\right) + a_{H_0}\right)} \\ &= \frac{1}{\bar{Z}\varphi_{H_0}(\frac{r\bar{X}}{r\bar{Z}})} \end{aligned} \tag{3.51}$$

where φ_{H_0} is defined by 3.11. Considering the transformation Φ, the last equation can written as:

$$Z = \frac{1}{\varphi_{H_0}(\frac{X}{Z})}$$

Hence, this equilibrium is corresponding to the local projection of the critical manifold, near $(X, Y, Z) = (0, 1, 0)$, which approaches to infinity at $X = \pm Z$.
In polar coordinates system (3.50) can be written as

$$\begin{aligned} r' &= F(r,\theta) := r(\sigma(\theta) - \mu(\theta)r), \\ \theta' &= 0. \end{aligned} \tag{3.52}$$

with,

$$\begin{aligned} \sigma(\theta) &= \cos^2(\theta) - \sin^2(\theta), \\ \mu(\theta) &= -\frac{b}{3}\cos^3(\theta) + (b-1)\cos(\theta)\sin^2(\theta) + a_{H_0}\sin^3(\theta). \end{aligned}$$

Since $\theta' = 0$, we can consider system (3.52) as a one dimensional system with constant parameter θ. The set of equilibria defined by $F(r,\theta) = r[\sigma(\theta) - \mu(\theta)r]r = 0$

consists of three branches:

$$B_1 = \{(\theta, r) : \theta \in [0, \pi), r = 0\},$$

$$B_2 = \{(\theta, r) : \theta = \pi/4, r \geq 0\}, \quad \text{and}$$

$$B_3 = \{(\theta, r) : \theta \in [3\pi/4, \pi), r = \sigma(\theta)/\mu(\theta) > 0\}.$$

Branch B_1 corresponds to the blown-up circle from the nonhyperbolic node at infinity, and it can be interpreted as an additional part of the critical manifold C_0, while, branches B_2 and B_3 correspond to the projected critical manifold.

Figure 3.5 illustrates the extended critical manifold near infinity. Panel (**a**) shows qualitative phase portraits of the JKE slow and fast subsystems projected on the (X, Z)-plane near the nonhyperbolic equilibrium $(X, Y, Z) = (0, 1, 0)$; and panel(**c**) illustrates the dynamic near the blown-up circle in the $(\bar{X}, \bar{Z})$-plane.

The branch B_1 has stability determined by the eigenvalue $\lambda = \sigma(\theta)$. Hence, the equilibria along B_1 are radially attracting for $\theta \in (\pi/4, 3\pi/4)$, radially repelling for $\theta \in (0, \pi/4) \cup (3\pi/4, \pi)$, and nonhyperbolic at $\theta = \pi/4,\ 3\pi/4$ since $\sigma(\theta) = 0$. Furthermore, the stability of the branch B_3 is determined by the eigenvalue $\lambda = \sigma(\theta) - 2\mu(\theta)\Big(\sigma(\theta)/\mu(\theta)\Big) = -\sigma(\theta)$. Hence, the equilibria along B_3 are radially repelling for $\theta \in (\pi/4, 3\pi/4)$ and radially attracting for $\theta \in (3\pi/4, \pi)$. Whereas, there is no radial flow along the B_2.

The stability of B_1 changes via transcritical bifurcation at $(r, \theta) = (0, 3\pi/4)$ [corresponding to the point of intersection between B_1 and B_3, depicted as red square in Figure 3.5 panel(**c**)]. Whereas, the stability of B_1 changes via degenerate transcritical bifurcation at $(r, \theta) = (0, \pi/4)$ [corresponding to the point of intersection between B_1 and B_2, depicted as red cross in Figure 3.5 panels(**c**)]. The dynamics near the degenerate bifurcation point $(r_*, \theta_*) := (0, \pi/4)$ has similar nature to that near the non-generic branching point $(x_*, y_*) = (1, -1/2)$ discussed earlier [see panel(**b**) in Figure 3.3].

Slow flow

Next, we discuss the slow flow along the extension branch B_1 of the critical manifold C_0. To this end, we follow the same steps in the analysis of fast flow to project the

flow of the slow subsystem (3.17) on the Poincaré sphere. Setting $P(x, y) = y$ and $Q(x, y) = 0$ in system (3.41) yields that the slow flow projection on the tangent plane to the nonhyperbolic node $(X, Y, Z) = (0, 1, 0)$ is given by:

$$\begin{aligned} \dot{X} &= P_*(X, 1, Z) = Z^3\, P(X/Z, 1/Z) = Z^2, \\ \dot{Z} &= 0. \end{aligned} \tag{3.53}$$

Using the polar blow-up transformation Φ (3.43), and after dividing the equations by r and rescaling the time variable, the flow along the branch B_1 can be described by the system,

$$\begin{aligned} \dot{r} &= \cos(\theta)\sin^2(\theta) r, \\ \dot{\theta} &= -\sin^3(\theta). \end{aligned} \tag{3.54}$$

Hence, the slow flow on the branch B_1 has two non-hyperbolic nodes; $(r, \theta) = (0, 0)$ and $(r, \theta) = (0, \pi)$, and the flow between the two nodes is clockwise.

Similar to $(X, Y, Z) = (0, -1, 0)$, we can obtain projection of the JKE flow on the tangent plane to the point $(X, Y, Z) = (0, -1, 0)$, and regain hyperbolicity by blowing-up the node to unit cycle. The fast flow near the blown-up cycle is described by:

$$\begin{aligned} r' &= r(\sigma(\theta) + \mu(\theta) r), \\ \theta' &= 0, \end{aligned} \tag{3.55}$$

while the slow flow on the blown-up circle is given by,

$$\begin{aligned} \dot{r} &= -\cos(\theta)\sin^2(\theta) r, \\ \dot{\theta} &= \sin^3(\theta). \end{aligned} \tag{3.56}$$

The fast subsystem at infinity (3.55) defines three branches of equilibria.

$$B_1 = \{(\theta, r) : \theta \in [0, \pi), r = 0\},$$

$$B_2 = \{(\theta, r) : \theta = \pi/4, r \geq 0\}, \quad \text{and}$$

$$B_3 = \{(\theta, r) : \theta \in [0, 3\pi/4), r = -\sigma(\theta)/\mu(\theta) > 0\},$$

see Figure 3.3 panel(**d**).

Stability and interpretation of branches B_1 and B_2 are the same as the equiv-

alent branches near the node $(X, Y, Z) = (0, 1, 0)$. Furthermore, branch B_3 also corresponds to the projected critical manifold and has the eigenvalue $\lambda = -\sigma(\theta)$, however, it is defined over $\theta \in [0, 3\pi/4]$ and the equilibria on B_3 are radially repelling. The branch B_1 exchange stability twice; first, via transcritical bifurcation at $(r, \theta) = (0, 3\pi/4)$ (red square in Figure 3.3 panel(**d**)) and second, via degenerate transcritical bifurcation at $(r, \theta) = (0, \pi/4)$ (red cross in Figure 3.3 panel(**d**)). The flow of the slow subsystem near infinity described by (3.56) has two non-hyperbolic nodes on the blown-up circle, $(r, \theta) = (0, 0)$ and $(r, \theta) = (0, \pi)$, with counterclockwise slow flow between them.

Hence, the flow of the unbounded singular canard cycles is attracted to the stable parts of the blown-up circle, then following the slow flow on the branch B_1, crossing the nonhyperbolic point of the critical manifold C_0 and repelled back along fast layer toward a stable part of the critical manifold. The hyperbolicity of B_1 and the slow flow on the blown-up circle from the points $(X, Y, Z) = (0, \pm 1, 0)$ provide explanation of the return mechanism connecting the unbounded layer flow near infinity. Furthermore, the singular canard cycles is small (respectively large) if the orbit is connected to one equilibrium (respectively two equilibria) at infinity [see Figure 3.4 panel(**d**)]. The question remaining to be answered is how to match the coming layer to infinity at angle $\theta \in (\pi/4, 3\pi/4)$ to the outgoing layer at angle $\theta \in (0, \pi/4)$ for the small singular canard and at $\theta \in (3\pi/4, \pi)$ for the large singular canard. A possible answer is to match the coming and outgoing equilibria by comparing the corresponding eigenvalues, however, this would also require considering the global behaviour of the canard cycles. Therefore, we will leaved the discussion of this question at this point.

The unbounded singular canard cycles can also be observed in other models (*e.g.* the aircraft ground dynamics model [69] and the earthquake faulting model [70, 71]) where the amplitude of canard cycles grows to infinity and whose critical manifold has asymptotic nonhyperbolicity a tangency with the layer flow at infinity. Similar to the JKE model, projection on the Poincaré sphere and blow-up method can be combined to provide an explanation of the return mechanism from infinity in the aircraft ground dynamics, which is a subject left for future studies.

3.3 The maximal canard in the JKE

The canard explosion in slow-fast planar systems, such as the JKE and FHN systems, occurs as one-dimensional attracting and repelling slow manifolds exchange their positions, upon small parameter change, near a nonhyperbolic bifurcation point of the critical manifold [50, 72]. The exchange of slow manifolds positions results in a rapid transition of periodic solutions from small limit cycle, originating from a singular Hopf bifurcation, to large relaxation oscillation orbit via a family of canard cycles [50, 67]. The intersection event of the attracting and repelling slow manifolds near the nonhyperbolic point defines the maximal canard solution, which follows an unstable branch of the critical manifold for a longer time [50, 67, 72]. Furthermore, the maximal canard differentiates the family of small canard cycle from the large canard orbits developing relaxation oscillation in the phase space [51, 72, 73].

It is known from Fenichels Theorem that the invariant slow manifolds perturbed from normally hyperbolic part of the critical manifold are generally not unique for a fixed ε, but lie at a distance $\mathcal{O}(e^{-k/\varepsilon})$ away from each other for some $k > 0$ [72, 74, 75]. Hence, the term "the slow manifold", associated with a hyperbolic part of the critical manifold, is to be understood unique up to an exponentially small error [66, 74]. However, two different trajectory representations of the slow manifold, which are exponentially-close in a small neighborhood of the nonhyperbolic bifurcation point of the critical manifold, might exhibit different geometrical properties after leaving the $\mathcal{O}(\varepsilon)$ neighborhood of the critical manifold [see for instance Figure 3.2 panels (**a-b**)]. Therefore, the trajectory representations of the attracting and repelling slow manifolds should be carefully chosen near the nonhyperbolic bifurcation point of the critical manifold as their intersection might lead to maximal canard candidates of different global behaviour (*e.g.* being a part of a periodic orbit or a transient solution). In this work, we will focus on the maximal canard cycle, *i.e.* when the attracting and repelling slow manifolds intersect along a periodic orbit (see Definition A.2.2).

In this section, we review different approaches to define candidates of the maximal canard. Furthermore, we discuss and compare the suitability of these approaches to the FHN and JKE models.

3.3.1 Parameter estimation approach

The first approach to define the maximal canard is by estimating a value for the parameter controlling the canard explosion at which the intersection of the attracting and repelling slow manifolds happens. The canard cycle associated with this parameter value, then, represents the candidate for the maximal canard. Theorem A.2 suggests an $\mathcal{O}\left(\varepsilon^{3/2}\right)$ estimation of the parameter value at which attracting and repelling slow manifolds intersect near a generic fold singularity of the critical manifold. This estimation is applicable to the FHN system since the critical manifold S_0 loses its hyperbolicity via fold singularity. To apply Theorem A.2 to FHN system (2.30), we shift the fold point to the origin and reverse the time by the change of variables $(t, x, z) \to \left(-t_1, x_1 + 1, z_1 - \frac{2}{3}\right)$. We also use the notation $\lambda = a - a_{H_0}$ for the control parameter. This leads to the system:

$$\begin{aligned} x_1' &= -\, z_1 + x_1^2 \left(1 + \frac{x_1}{3}\right) \\ z_1' &= \varepsilon \left(x_1 - \lambda + b\, z_1\right) \end{aligned} \tag{3.57}$$

which has fold singularity at $(x_1, z_1, a, \varepsilon) = (0, 0, 0, 0)$. Comparing the system (3.57) to (A.10), we obtain the functions:

$$h_1 = h_4 = h_5 = 1, \qquad h_2 = 1 + \frac{x_1}{3}, \qquad h_3 = 0, \qquad h_6 = b. \tag{3.58}$$

and the constants,

$$\begin{aligned} a_1 =& \frac{\partial}{\partial x_1} h_3(0,0,0,0) = 0, \qquad a_2 = \frac{\partial}{\partial x_1} h_1(0,0,0,0) = 0, \\ a_3 =& \frac{\partial}{\partial x_1} h_2(0,0,0,0) = \frac{1}{3}, \qquad a_4 = \frac{\partial}{\partial x_1} h_4(0,0,0,0) = 0, \\ a_5 =& \, h_6(0,0,0,0) = b, \qquad A = -a_2 + 3a_3 - 2a_4 + 2a_5 = 1 - 2b. \end{aligned} \tag{3.59}$$

Hence, by Theorem A.2, the parameter estimation corresponding to the slow manifolds intersection along the maximal canard is:

$$\lambda_c = -\left(\frac{a_1 + a_5}{2} + \frac{A}{8}\right)\varepsilon + \mathcal{O}(\varepsilon^{3/2}) = -\left(\frac{1 + 2b}{8}\right)\varepsilon + \mathcal{O}(\varepsilon^{3/2}); \tag{3.60}$$

Hence, after truncating the unknown terms, we obtain the estimated parameter value of Theorems A.2 corresponding to the maximal canards:

$$\lambda_{c_0} = -\left(\frac{1+2b}{8}\right)\varepsilon \tag{3.61}$$

which corresponds to

$$a_{c_0} = \lambda_{c_0} + a_{H_0} = \left(1 - \frac{2}{3}b\right) - \left(\frac{1+2b}{8}\right)\varepsilon \tag{3.62}$$

However, truncating $\mathcal{O}(\varepsilon^{3/2})$ unknown terms from the parameter estimations λ_{c_0} could shift the parameter value to the margin of the exponentially small parameter range of the canard explosion (see Figure 3.1 **a**), resulting in a periodic orbit that can be obviously classified as a small or large amplitude canard cycle. Higher precision approximations of the parameter value of the canard explosion and the local slow manifold can be computed using asymptotic analysis [76, 77] of system (3.57), however, that would rather require lengthy analysis for small $\varepsilon \ll 1$ and still does not provide any information about the global geometric behaviour of the slow manifold. For these reasons, we will not apply this analysis to the JKE system. Furthermore, since the estimated parameter value λ_{c_0} of the FHN system is invariant under the equivalence transformation (2.31), we adopt this value for the JKE system and consider, for comparison reasons, the transformed slow manifold, and hence the canard cycle, as a candidate for the maximal canard of the JKE according to this approach.

Next, we proceed to other approaches that consider the maximal canard candidate based on the geometric properties of the slow manifold and canard cycles.

3.3.2 Inflection points approach

The set of inflection points has been suggested to distinguish between small and large canard cycles organised by an N shaped critical manifold in planer slow-fast systems, such as Van der Pole and FitzHugh-Nagumo models [51, 72, 73]. In FHN model, small amplitude cycles (canards without head) enclose a convex area in state space, whereas, large amplitude cycles (canards with head) enclose a non-convex area as

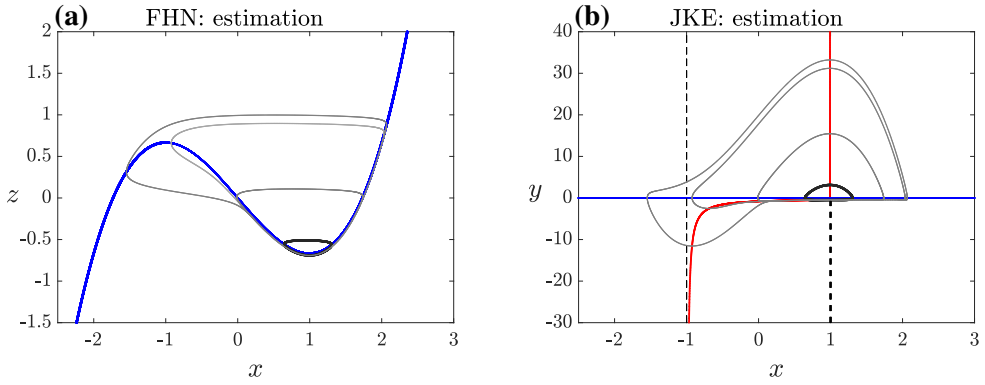

Figure 3.6: Maximal canard candidate: parameter estimation. Panels (**a**) and (**b**) for FHN and JKE, respectively. The orbits are computed for the parameter setting $b = 0.3$ and $\varepsilon = 0.05$. The black cycle, corresponding to the maximal canard candidate, is computed at $a = a_c = 0.79$, which lies in the margin of the canard explosion range because of the truncation. All other grey cycles are for $a \approx 0.789784543$. Similar example can be found in [74].

they intersect inflection curve near the repelling part of the critical manifold before being repelled to the left and following the left attracting branch [see Figure 3.2 panel(**a**)].

Furthermore, the existence of inflection curve in the neighbourhood of the repelling slow manifold determines the presence of non-convexity distinction between the periodic orbits that can be described as small or large canard cycles for sufficiently large separation of time scale. If the inflection curve disappears after increasing the time-scale separation parameter ε, there is no distinction between the small and large cycles so they might not be described as canard cycles due to non sufficient separation of time-scales. Therefore, the existence of inflection curve can provide a criterion on the smallness of the time-scale separation parameter ε that can be associated with the existence of canard phenomenon [51].

Hence, in the sense of convexity criterion, the maximal canard might be described as the first limit cycle that intersects the inflection curve, which characterises the transition between small (convex) and large (non-convex) canard cycles.

To discuss the suitability of this approach to the FHN and JKE systems, we follow [51] to obtain the inflection curve of the systems.

Consider the FHN system (2.30), which can be written as:

$$\begin{aligned} x' &= z - f(x) \\ z' &= \varepsilon\ (g(x) - bz)\,, \end{aligned} \tag{3.63}$$

where $f(x) = \left(\frac{x^3}{3} - x\right)$ and $g(x) = (a - x)$. The inflection curve is defined by the set of zero-curvature in the state space:

$$\mathbb{I} = \left\{(x, z(x)) \in \mathbb{R}^2 : \kappa(x) = 0\right\} \tag{3.64}$$

where

$$\kappa(x) = \frac{z''(x)}{\left(1 + z'^2(x)\right)^{3/2}} \tag{3.65}$$

Hence, the set $\mathbb{I}$ is determined by the condition $z''(x) = 0$. The trajectories of (3.63) satisfy

$$(z - f(x))\,\frac{dz}{dx} = \varepsilon\ (g(x) - bz)\,, \tag{3.66}$$

Differentiating (3.66) with respect to x leads to:

$$\left(\frac{dz}{dx} - f'\right)\frac{dz}{dx} + (z - f)\frac{d^2z}{dx^2} = \varepsilon\ \left(g' - b\frac{dz}{dx}\right), \tag{3.67}$$

Setting $\frac{d^2z}{dx^2} = 0$ leads to

$$\left(\frac{dz}{dx}\right)^2 - (f' - \varepsilon b)\frac{dz}{dx} - \varepsilon g' = 0 \tag{3.68}$$

This quadratic equation has, depending on ε, two solution branches defined as

$$\frac{dz}{dx} = \frac{1}{2}\left[(f' - \varepsilon b) \pm \sqrt{(f' - \varepsilon b)^2 + 4\varepsilon g'}\right] \tag{3.69}$$

or

$$\frac{dz}{dx} = h_\pm(x) := \frac{1}{2}\left[(x^2 - 1 - \varepsilon b) \pm \sqrt{(x^2 - 1 - \varepsilon b)^2 - 4\varepsilon}\right] \tag{3.70}$$

The function $h_\pm(x)$ has real values only if

$$(x^2 - 1 - \varepsilon b)^2 > 4\varepsilon \tag{3.71}$$

We focus now on the inflection curve branches near the repelling part of critical manifold (*i.e.* in the region $-1 < x < 1$), the condition (3.71) leads to

$$0 < x^2 < 1 + \varepsilon b - 2\sqrt{\varepsilon} \tag{3.72}$$

which can be analysed to

$$\left(\sqrt{\varepsilon} - \frac{1}{b}(1 - \sqrt{1-b})\right)\left(\sqrt{\varepsilon} - \frac{1}{b}(1 + \sqrt{1-b})\right) > 0 \tag{3.73}$$

The only case leading to an upper bound of the parameter ε is

$$\sqrt{\varepsilon} < \frac{1}{b}(1 - \sqrt{1-b}) \tag{3.74}$$

which leads to the critical value

$$\varepsilon_0 = \frac{1}{b^2}(1 - \sqrt{1-b})^2 = \frac{1}{(1 + \sqrt{1-b})^2} \tag{3.75}$$

Hence, the set of inflection points is not empty near the repelling part of S_0, defined over $-1 < x < 1$, for the parameter range $0 < \varepsilon \leq \varepsilon_0$. Combining (3.66) and (3.75) defines branches of inflection curve as:

$$z(x) = \frac{f(x)h_{\pm}(x) + \varepsilon g(x)}{h_{\pm}(x) + \varepsilon b} \tag{3.76}$$

Observe that, for $b = 0$, system (3.66) is the Van der Pol system, which has critical parameter value $\varepsilon_0 = \frac{1}{4}$ [51].

Consider now the JKE system (2.29), which can be written as:

$$\begin{aligned} x' &= \varepsilon\, y \\ y' &= p(x) - q(x)y \end{aligned} \tag{3.77}$$

where $p(x) := \left(-\frac{b}{3}x^3 + (b-1)x + a\right)$ and $q(x) := (x^2 - 1 + \varepsilon b)$. The inflection curve is defined by the set of zero-curvature in the state space:

$$\mathbb{I} = \left\{(x, y(x)) \in \mathbb{R}^2 : \kappa(x) = 0\right\} \tag{3.78}$$

where

$$\kappa(x) = \frac{y''(x)}{(1 + y'^2(x))^{3/2}} \tag{3.79}$$

Hence, the set $\mathbb{I}$ is determined by the condition $y''(x) = 0$. The trajectories of (3.77) satisfy

$$\varepsilon y \frac{dy}{dx} = p(x) - q(x)y, \tag{3.80}$$

Differentiating (3.80) with respect to x leads to:

$$\varepsilon y \frac{d^2y}{dx^2} + \varepsilon \left(\frac{dy}{dx}\right)^2 = p' - q'y - q\frac{dy}{dx}, \tag{3.81}$$

Setting $\frac{d^2y}{dx^2} = 0$ leads to

$$\varepsilon \left(\frac{dy}{dx}\right)^2 + q\frac{dy}{dx} + q'y - p' = 0 \tag{3.82}$$

Substituting $\frac{dy}{dx}$ from (3.80) in (3.82) leads to

$$\varepsilon \left(\frac{p - qy}{\varepsilon y}\right)^2 + q\left(\frac{p - qy}{\varepsilon y}\right) + q'y - p' = 0 \tag{3.83}$$

After simplifications, we end up with the algebraic equation describing the zero-curvature set:

$$\varepsilon q'y^3 - \varepsilon p'y^2 - pqy + p^2 = 0 \tag{3.84}$$

Since the algebraic equation (3.84) is cubic in the variable y, at least one branch of the inflection curve always exists close to the unstable slow manifold for some values of $-1 < x < 0$, which leads to inflection even in the small canard cycles. Furthermore, from (3.80), it is obvious that for $p(x) \neq 0$ and $q(x) \neq 0$ the inflection curve approaches the critical manifold in the singular limit $\varepsilon \to 0$ yielding that a branch of the inflection curve exists close to the repelling part of the critical manifold for all values of $\epsilon > 0$.

In Figure 3.7, we illustrate the inflection curves of the FHN and JKE systems in addition to representative small and large amplitude cycles. Panel (**a**), for $\varepsilon = 0.05$, shows that the large amplitude limit cycle crosses an inflection branch once near the

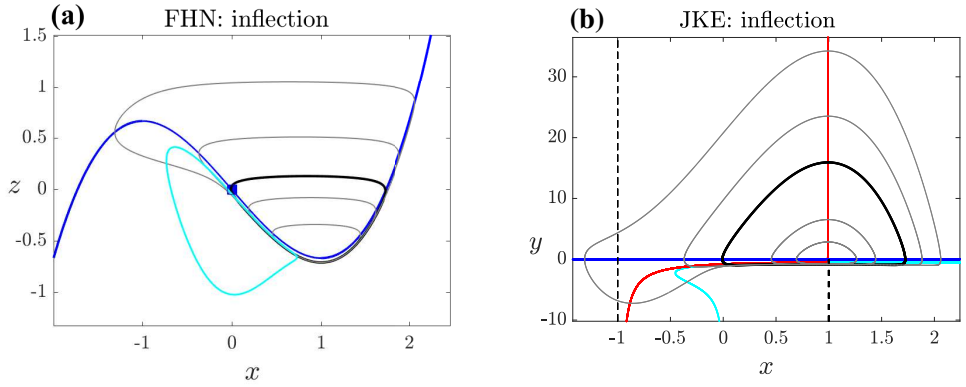

Figure 3.7: Maximal canard candidate: inflection curve. Panels (**a**) and (**b**) for FHN and JKE, respectively. Orbits are computed for $b = 0.3$ and $\varepsilon = 0.05$. The black cycle represents convex small canard cycle which can follow the critical manifold up to the inflection point of the critical manifold plotted in blu square.

repelling slow manifold before jumping to the left, then crosses another inflection branch before following the right attracting slow manifold. Whereas, the small amplitude cycle jumps to the right without intersecting the inflection curves, which is what keeps the small cycles convex. The limit cycle plotted in black represents the maximal canard candidate which intersects the inflection curve (depicted in cyan), tangentially, at only on point, and hence it represents the extinction between convex and non-convex canard cycles. However, the maximal canard candidate might be considered as small canard since it does not follow the repelling slow manifold for the greater time. Instead, it jumps early to the right. The reason of this behavior of the convex cycle of the largest possible amplitude is that the inflection curve converges to the critical manifold as $\varepsilon \to 0$ [51], and since the critical manifold S_0 itself has an inflection point at $(x, z) = (0, 0)$, therefore, for sufficiently small $\varepsilon \ll 1$, any convex canard cycle can follow the critical manifold up to small neighbor of $(x, z) = (0, 0)$, approximately half the length of the repelling part of S_0. Therefore, the "convex" maximal canard candidate does not have the maximal following of the repelling slow manifold between the two folds.

On the other hand, panels (**b**) illustrates the presence of inflection branch close to repelling part of stable manifold for different values of ε, which suggests that this approach is not applicable to the JKE system (3.77), since relatively small amplitude cycles are non-convex even for relatively large values of ε.

3.3.3 Boundary value problem approach

In order to determine the maximal canard cycle lying in the intersection of attracting and repelling slow manifolds near a nonhyperbolicity of the critical manifold, it is natural to ask about which trajectory segments represent the attracting and repelling slow manifolds in the state space? If segment-representations of the slow manifolds are determined, the maximal canard cycle can be numerically obtained as a solution of multi-segments boundary value problem MSBVP. In this part, we discuss possible criteria to specify the segment representation of the slow manifolds for the FHN and JKE models. In addition, we present general BVP formulations to compute the canard periodic orbit and the maximal canard corresponding to each criterion. More details on using BVP approaches in slow-fast problems can be found, for example, in [78–80].

To determine the segment-representation of the repelling slow manifold, we consider two approaches; the first is the trajectory following the unstable part of the critical manifold and passing through the nonhyperbolicity. In the case of FHN system, the segment starts on a section near the nonhyperbolic fold, where the attracting and repelling slow manifolds intersect, and passes through the other fold, corresponding to the end of the unstable part of the critical manifold S_0. Whereas, for the JKE system, the segment starts on a section near the perturbed branching point, where the attracting and repelling slow manifolds intersect, then continue following the unstable critical manifold until intersecting tangentially (non-transversally) with the nonhyperbolicity asymptote, corresponding to the end of the unstable part of the critical manifold C_0. The second case is the trajectory segment that follows the unstable part of the critical manifold for the maximal period of time before intersecting the critical manifold near the nonhyperbolicity. So, the trajectory starts close to the first nonhyperbolic bifurcation point where the attracting and repelling slow manifolds intersect, and ends simply at the critical manifold.

Next, we present general formulations of a multi-segment boundary value problem that is suitable for our problems. The solution of the MSBVP is a sequence of segments that collectively form the periodic orbit given specific constraints (e.g. passing through specific point or computed at a specific parameter value). Then we apply this approach to compute the maximal canard candidates of JKE and FHN systems.

Consider a planar system of the form:

$$\dot{\mathbf{x}} = \mathbf{f}(\mathbf{x}, \lambda) \tag{3.85}$$

where $\mathbf{x} = \left[\begin{smallmatrix} x \\ y \end{smallmatrix}\right] \in R^2$, λ is a parameter and the dot denotes the derivative with respect to time $\left(\frac{d}{dt}\right)$. Assume that there exists a solution segment $x(t)$ of equation (3.85) defined on the interval $[0, T]$ and satisfying the boundary conditions:

$$\mathbf{x}(0) = \mathbf{x}_a,\ \mathbf{x}(T) = \mathbf{x}_b \tag{3.86}$$

In order to compute the solution segment of this BVP we first normalize the time interval to $[0, 1]$ by $t' = \dfrac{t}{T}$, and equation (3.85) will take the form:

$$\dot{\mathbf{x}} = T\ \mathbf{f}(\mathbf{x}, \lambda) \tag{3.87}$$

Then we extend system (3.87) by including the trivial dynamics of the unknowns T and λ. Therefore, the BVP will be in the form:

$$\begin{aligned} \dot{\mathbf{x}} &= T\ \mathbf{f}(\mathbf{x}, \lambda) \\ \dot{T} &= 0 \\ \dot{\lambda} &= 0 \\ \mathbf{x}(0) = \mathbf{x}_a,\ &\mathbf{x}(1) = \mathbf{x}_b \end{aligned} \tag{3.88}$$

Now assume there exists a periodic solution of system (3.85) of period T for some (possible unknown) value of the parameter λ that passed through the point $\mathbf{x} = \mathbf{x}_* = \left[\begin{smallmatrix} x_* \\ y_* \end{smallmatrix}\right]$ in the phase space, then the periodic solution can be represented by closed orbit in the phase space and satisfies the following BVP:

$$\begin{aligned} \dot{\mathbf{x}} &= T\ \mathbf{f}(\mathbf{x}, \lambda) \\ \dot{T} &= 0 \\ \dot{\lambda} &= 0 \\ \mathbf{x}(0) - \mathbf{x}_* = 0,\ &\mathbf{x}(1) - \mathbf{x}_* = 0 \end{aligned} \tag{3.89}$$

the number of constraints in BVP (3.89) is four (two components x and y in each

boundary conditions) which equals to the number of unknowns which are the two components of the dynamic variable $\mathbf{x}$ and the two parameters T and λ. Such BVP can be solved using the Matlab solver `bvp5c`.

If the closed orbit intersects transversally the sections Σ_i in the phase space at the points $\mathbf{x} = \mathbf{x}_{\Sigma_i}$, respectively, where $i = 1, ..., n$ and $\mathbf{x}_* = \mathbf{x}_j$ for some j, then each segment S_i of the orbit connects two adjacent sections Σ_i and Σ_j is a solution of the segment BVP:

$$\begin{aligned} \dot{\mathbf{x}}_i &= T_i\, \mathbf{f}(\mathbf{x}_i, \lambda) \\ \dot{T}_i &= 0 \\ \dot{\lambda}_i &= 0 \\ \mathbf{x}_i(0) = \mathbf{x}_{\Sigma_i},\ \mathbf{x}_i(1) &= \mathbf{x}_{\Sigma_j} \end{aligned} \tag{3.90}$$

where $j = i + 1$ for $i = 1, ..., n - 1$ and $j = 1$ for $i = n$. Here the constant T_i is the time of the segment S_i which varies for different segments and collectively equal the period of the closed orbit *i.e.* $\sum_{i=1}^{n} T_i = T$. However, the constant values λ_i has to be the same for all the segments and equal to the parameter value λ of the closed orbit. To this end, we introduce continuity conditions of the segments through the sections to guarantee the equality of the parameter values λ_i without increasing the number of constraints in the boundary conditions.

We basically choose the known point $\mathbf{x}_* \in \Sigma_1$ as a starting point of the first segment, constrain the end point to belong to the second section Σ_2, without specifying the point, and leave the parameter value λ_i unspecified to be computed by the solver. This results in three constraints for the first segment which are:

$$\mathbf{x}_1(0) = \mathbf{x}_*,\ \mathbf{x}_1(1) \in \Sigma_2$$

For the following segments except the last one we specify the starting point on the section Σ_i and the parameter value of the segment to be equal to the end point and the parameter value of the preceding segment, respectively, and we constrain the end point to belong to the following section Σ_{i+1}, without specifying the point. Hence, we associate four constraints with these segments, namely:

$$\mathbf{x}_i(0) = \mathbf{x}_{i-1}(1),\ \mathbf{x}_i(1) \in \Sigma_{i+1},\ \lambda_i = \lambda_{i-1}$$

where $i = 2, ..., n-1$. The last segment is forced to start from the last section Σ_n at the end point of the preceding segment and to end on the first section at the starting point of the first segment, or more precisely at $\mathbf{x}_*$, in addition, the parameter value λ_n has to be equal to the parameter value of the previous segment. This leads to five constraints for the last segment *i.e.*

$$\mathbf{x}_n(0) = \mathbf{x}_{n-1}(1),\ \mathbf{x}_n(1) = \mathbf{x}_1(0),\ \lambda_n = \lambda_{n-1}$$

Thus, the MSBVP involves $4n$ unknowns and $4n$ constraints in the boundary conditions and can be written in the form:

$$\begin{gathered}
\dot{\mathbf{x}}_i = T_i\ \mathbf{f}(\mathbf{x}_i, \lambda) \\
\dot{T}_i = 0 \\
\dot{\lambda}_i = 0 \\
\mathbf{x}_1(0) - \mathbf{x}_* = 0,\ \mathbf{x}_1(1) \in \Sigma_2 \\
\mathbf{x}_i(0) - \mathbf{x}_{i-1}(1) = 0,\ \mathbf{x}_i(1) \in \Sigma_{i+1},\ \lambda_i - \lambda_{i-1} = 0, \quad \text{for } i = 2, ..., n-1 \\
\mathbf{x}_n(0) - \mathbf{x}_{n-1}(1) = 0,\ \mathbf{x}_n(1) - \mathbf{x}_1(0) = 0,\ \lambda_n - \lambda_{n-1} = 0
\end{gathered} \tag{3.91}$$

The solution of the MSBVP (3.91) is a sequence of n segments which forms a closed orbit starting and ending at the point $\mathbf{x} = \mathbf{x}_*$ in the phase space. If the closed orbit is not constrained to pass through a specific point in the plane, then we can compute the periodic solution for a given parameter value, say λ_*, if such solution exists, and the only changes we need to do on the problem (3.91) is the boundary conditions of the first segment. We no more specify the starting point of the first segment on the first section, instead, we specify the parameter value of the first segment to be λ_* and the continuity conditions of the parameter through the sections guarantees that this value will be the same for all the segments. The number of constraints in the boundary conditions of the first segment remains three and the multi-segment

BVP for the parameter value λ_* is given by:

$$\begin{gathered}
\dot{\mathbf{x}}_i = T_i\, \mathbf{f}(\mathbf{x}_i, \lambda) \\
\dot{T}_i = 0 \\
\dot{\lambda}_i = 0 \\
\mathbf{x}_1(0) \in \Sigma_1,\ \mathbf{x}_1(1) \in \Sigma_2,\ \lambda_1 - \lambda_* = 0 \\
\mathbf{x}_i(0) - \mathbf{x}_{i-1}(1) = 0,\ \mathbf{x}_i(1) \in \Sigma_{i+1},\ \lambda_i - \lambda_{i-1} = 0, \quad \text{for } i = 2, ..., n-1 \\
\mathbf{x}_n(0) - \mathbf{x}_{n-1}(1) = 0,\ \mathbf{x}_n(1) - \mathbf{x}_1(0) = 0,\ \lambda_n - \lambda_{n-1} = 0
\end{gathered} \tag{3.92}$$

In practice, the number and choice of the sections and segments required to compute

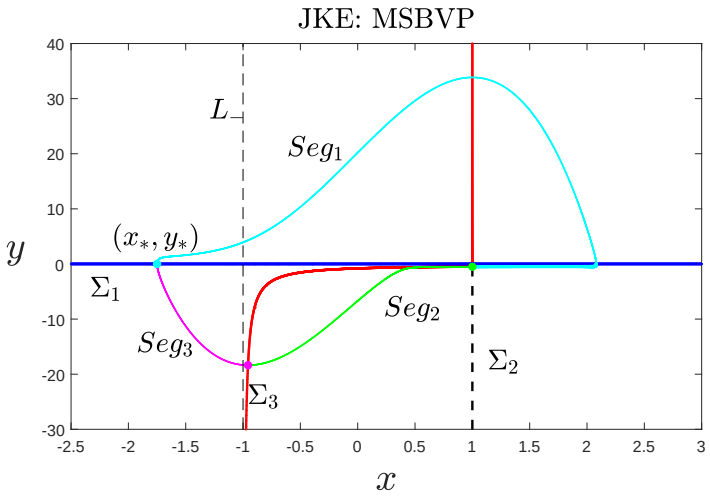

Figure 3.8: MSBVP of periodic solution of the JKE (14) computed for $b = 0.3$, and $\varepsilon = 0.05$. The solution segments are labeled as Seg_i and the sections as Σ_i for $i = 1, 2, 3$. The red solid line is the repelling part of the critical manifold C_0. The closed orbit starts and ends at the point (x_*, y_*).

canard cycles of different systems are problem dependent. For our purpose, a three segments BVP is sufficient to computing the canard cycles of the JKE and FHN systems as we explain in the following:

Recall the JKE system (3.15):

$$\begin{aligned} \dot{x} &= y \\ \varepsilon\, \dot{y} &= \left(-\frac{b}{3}\, x^3 + (b-1)x + a \right) - \left(x^2 - 1 + \varepsilon b \right) y \end{aligned} \tag{3.93}$$

where a is the control parameter. The critical manifold of the system is given by:

$$C_0 = \left\{ (x, y) \mid y = \frac{-\frac{b}{3}\, x^3 + (b-1)x + a}{(x^2 - 1)} \right\}$$

and the x-nullcline is the line $y = 0$. In order to formulate a MSBVP of system (3.93), we define three sections in the phase space as:

$$\Sigma_1 = \{(x, y) \mid x < 1,\ y = 0\}$$

$$\Sigma_2 = \{(x, y) \mid x = 1,\ y < 0\}$$

$$\Sigma_3 = \{(x, y) \in C_0 \mid\ -1 < x < 1,\ y < 0\}$$

All the periodic of the JKE system (3.93) intersect the sections: Σ_1 (a part of the x-axis to the left of the equilibrium), Σ_2 (the part of the asymptote below the equilibrium) and Σ_3 (the unstable part of the critical manifold C_0 to the left of the equilibrium). Although the sections Σ_1 and Σ_3 are very close for near the equilibrium, this choice helps us to compare the flow time from section Σ_2 until intersecting the unstable critical manifold of the JKE and FHN systems (recall that section Σ_1 is the transformation of the critical manifold S_0 of the FHN system to the JKE phase space). Now we can define a MSBVP of system (3.93) that is suitable for both FHN and JKE systems. Recall that the solutions of the FHN system can be obtained from the solution of JKE system for $\varepsilon > 0$ by the transformation:

$$z = \left(\varepsilon y - x + \frac{x^3}{3} \right) \tag{3.94}$$

Let $(x_*, y_*) \in \Sigma_1$ be the intersection point of the periodic orbit with the first section Σ_1. Since Σ_1 is a part of the x-nullcline of the JKE system, the point (x_*, y_*) has

the minimum x-coordinate along the periodic orbit (*i.e.* $x_* = x_{min}$). Considering (x_*, y_*) as starting point of the orbit, the formulation of the MSBVP of system (3.93) can be given by:

$$\begin{gathered}
x_i' = T_i\, y_i \\
y_i' = \frac{T_i}{\varepsilon}\left[\left(-\frac{b}{3}\, x_i^3 + (b-1)x_i + a_i\right) - \left(x_i^2 - 1 + \varepsilon b\right) y_i\right] \\
T_i' = 0 \\
a_i' = 0 \\
x_1(0) = x_*,\ y_1(0) = y_*,\ (x_1(1), y_1(1)) \in \Sigma_2 \\
x_2(0) = x_1(1),\ y_2(0) = y_1(1),\ a_2(0) = a_1(1),\ (x_2(1), y_2(1)) \in \Sigma_3 \\
x_3(0) = x_2(1),\ y_3(0) = y_2(1),\ a_3(0) = a_2(1),\ x_3(1) = x_1(0),\ y_3(1) = y_1(0)
\end{gathered} \tag{14}$$

The solution of (3.93) determines three segments Seg_1, Seg_2 and Seg_3 that are connected at the sections Σ_1, Σ_2 and Σ_3 forming the canard periodic orbit of the JKE system [see Figure 3.8]. The first orbit segment Seg_1 starts from the point (x_*, y_*) and ends at the second section Σ_2, which is the lower part of the asymptote L_+ of the critical manifold C_0. The second segment Seg_2 of the canard orbit starts from the last point of the first segment Seg_1 and ends at the third section Σ_3, which is the lower part of the repelling middle part of the critical manifold C_0. The last segment Seg_3 starting from last point of the second segment Seg_2 and ends at the starting point (x_*, y_*) of the first segment Seg_1. Hence, the three segments form a closed orbit representing the canard cycle of the system (3.93) [see Figure 3.8].

Notice that the canard orbit segment Seg_1 to the right of section Σ_2 follows the attracting part of the critical manifold, while the segment Seg_2 to the left of section Σ_2 follows the repelling part of the critical manifold until they intersect. Therefore, the intersection of the maximal canard orbit with the section Σ_2 represents the intersection of the attracting and repelling slow manifolds. According to the approaches we described above, the maximal canard candidates of the JKE and FHN systems can be computed as follows:

The canard cycle through the nonhyperbolicity of the critical manifold: This orbit is determined by setting the starting point of the orbit on Σ_1 to be $(x_*, y_*) = (-1, 0)$. For the JKE system, the section Σ_1 is a part of the x-nullcline

(where the flow is vertical), therefore, the canard orbit perpendicularly intersects the x-nullcline at the point $(x_*, y_*) = (-1, 0)$ and hence, it non-transversally intersects the nonhyperbolicity asymptote L_- [see the green curve in Figure 3.9 (**a**)]. The uniqueness of this candidate follows from the fact that any other canard orbit with $x_{min} > -1$ does not intersect the nonhyperbolicity asymptote L_-, and any orbit with $x_{min} < -1$ intersects the L_- transversely at two points. For the FHN system (3.14), the x-nullcline can be transformed by (3.94) into the critical manifold S_0 of the FHN system, and the point $(x_*, y_*) = (-1, 0)$ is transformed into $(x_*, z_*) = (-1, \frac{2}{3})$ corresponding to a nonhyperbolic fold of the critical manifold S_0 [see the green curve in Figure 3.9 (**b**)]. Hence, the maximal canard candidate through nonhyperbolicity for the FHN system is just a transformation of the corresponding maximal canard candidate through nonhyperbolicity for the JKE system under (3.94).

Next we consider the following time of the canard orbits to the repelling critical manifold to define a candidate of the maximal canard:

The canard cycle of maximal following time We define the following time of a canard orbit of the JKE system to the repelling part of the critical manifold C_0 to be $T = T_2$, where T_2 is the time of the second segment Seg_2, which follows the unstable part of the critical manifold C_0 until they intersect [see the green curve in Figure 3.9 (**a**)]. While, for the FHN system, we define the following time of a canard orbit (transformed from the corresponding JKE orbit by (3.94)) to be $\tilde{T} = T_2 + T_3$ (the sum of the times of Seg_2 and Seg_3), which is the time of the canard orbit part (defined as the union of the transformed Seg_2 and Seg_3) following the unstable part of the critical manifold S_0 until they intersect [see the green curve in Figure 3.9 (**b**)]. Recall that the x-nullcline of the JKE system corresponds to the critical manifold S_0 of the FHN system. Given that a representative family of small and large canard orbits of the JKE system has been computed, the maximal canard candidate of maximal following time for the JKE and FHN systems are the orbits of maximal values of T and $\tilde{T}$, respectively.

To compute the maximal canard candidates of the JKE and FHN systems using the MSBVP (14), we used the Matlab BVP solver `bvpc5`. The BVP solver `bvpc5` uses the collocation points method to solve the entire BVP at once (after converting it into algebraic equations) which is more efficient than using time-stepping integrators which might cause a significant accumulated errors in the numerical

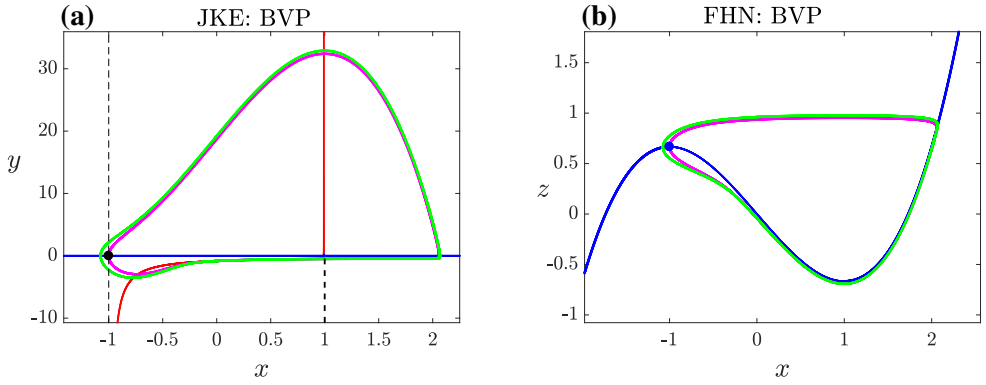

Figure 3.9: Maximal canard candidate: BVP. Panels (**a**) and (**b**) for JKE and FHN, respectively. The fixed parameter setting is $b = 0.3$ and $\varepsilon = 0.05$. A family of periodic orbits has been computed over a range of the parameter a and the plotted orbits are of the maximum following time T and $\tilde{T}$. Depending on how close the orbits are, the numerical computed values of the parameter a can agree in precision up to 10^{-13} (see also Figure 3.1). The green periodic orbit spends longer time than other nearby trajectory from the nonhyperbolic bifurcation point to a neighborhood of other nonhyperbolic point. The magenta orbit crossing through the nonhyperbolicity on the left. The difference of the two candidates is relatively small comparing to the other approaches.

computation of canard periodic orbits. Other possible tools that can also be used are numerical continuation software, *e.g.* `AUTO` [57], which also uses the collocation points method. For the initial guess we used the forward and backward time integration form the initial point $(x_*, y_*) = (x_{min}, 0)$. Figure 3.9 shows the computed maximal canard candidates of the JKE and FHN systems for the parameter setting ($b = 0.3,$ and $\varepsilon = 0.05$). This figure shows that the maximal canard candidate computed using the two BVP approaches (maximal following time and nonhyperbolicity crossing) are quite similar and well representing the maximal canard cycle comparing to the corresponding candidates computed using the parameter-estimation and inflection-points approaches.

We also remark here that the repelling slow manifold in the phase space can also be represented by the trajectory segment of the JKE system starting at section Σ_2 and ends at the nonhyperbolicity point $(-1, 0)$ or that follows the unstable part of the critical manifold for maximal time. The repelling slow manifold provides a threshold property in the state space of the JK-excitator which has been proposed to explain perturbation-induced movement behaviours such as the false

starts phenomenon [9, 13].

3.4 Summary

In this chapter, we explored the canard phenomena in the JKE system and compared it to the classical canard of the FHN model. We performed a slow-fast analysis and discussed the local canard behaviour organised by a non-generic branching point at the y-nullcline of the system. Furthermore, we used a combination of projection onto the Poincaré sphere and the blow-up technique to explain the return mechanism of the singular canard cycles from infinity. Moreover, we discussed different approaches to define and compute the maximal canard. The results of our analysis show that although the JKE model is topologically equivalent to the FHN model (for $\varepsilon > 0$), the different critical manifolds the two models have lead to different global behaviour of the canard orbits revealing dissimilarity in the dynamical properties of the two models (for $\varepsilon = 0$). Hence, the analysis we present in this chapter provides a complement to the analysis of the JKE discussed in the previous chapter. Furthermore, the BVP approach we reviewed for computing the maximal canards can also be applied to compute the repelling slow manifold in the state space of the JKE system, which provides an explanation of some of perturbation-induced movement behaviours (*e.g.* false starts [13]) via threshold property of the model. Moreover, the approach we propose to explain the dynamical mechanisms organising the canard phenomena in the JKE system might also be applied to other real-life models undergoing similar canard phenomena that exhibit an infinitely large growth of oscillation amplitude (*e.g.* the aircraft ground dynamics model [69].

Chapter 4

Dynamical Systems Analysis of The Coupled HKB Oscillators

Empirical movement studies [2, 19, 30] has observed a transition of bimanual movement coordination from an antisymmetrical to a symmetrical pattern as the movement pacing increases. No similar transition has been observed when the movement is initiated in the symmetric coordination mode [19]. This transition has been attributed to the loss of stability of the asymmetric coordination pattern as the movement pacing rate increases [8]. This suggests that the movement pattern transition is associated with switching of the coordination dynamics from bistable in-phase and anti-phase oscillations (characterised by relative phase between the two oscillators equals to 0° and 180°, respectively) to monostable in-phase periodic regime as the frequency of oscillation increases [8, 19]. The transition in the stability of different coordination patterns has inspired the development of the HKB model [2, 8]. In this chapter, we investigate the stability of in-phase and anti-phase coordination patterns in the HKB model, considering the effects of time-delay in the coupling. The full HKB model consisting of two coupled hybrid oscillators is given [8] by:

$$\begin{aligned} \ddot{x}_1 + \omega^2 x_1 - \gamma \dot{x}_1 + \alpha x_1^2 \dot{x}_1 + \beta \dot{x}_1^3 =& I(x_1, \dot{x}_1, x_{1\tau}, \dot{x}_{1\tau}, x_2, \dot{x}_2, x_{2\tau}, \dot{x}_{2\tau}) \\ \ddot{x}_2 + \omega^2 x_2 - \gamma \dot{x}_2 + \alpha x_2^2 \dot{x}_2 + \beta \dot{x}_2^3 =& I(x_2, \dot{x}_2, x_{2\tau}, \dot{x}_{2\tau}, x_1, \dot{x}_1, x_{1\tau}, \dot{x}_{1\tau}) \end{aligned} \tag{4.1}$$

where $I(x_i, \dot{x}_i, x_{i\tau}, \dot{x}_{i\tau}, x_j, \dot{x}_j, x_{j\tau}, \dot{x}_{j\tau})$ represents the coupling function with time-delay τ. The time delay incorporated in the coupling (4.1) may reflect delays asso-

ciated with the information exchange and signal processing in the brain and neural system [29, 44]. The time delay influences the stability properties of the dynamical systems, as we will demonstrate in the next sections.

Previous studies have studied the phase-approximation dynamics in the HKB model for weak coupling [48, 49]. Here we follow different approach and systematically investigate the behaviour of the HKB model in the full four-dimensional state space considering general coupling strengths. We investigate the influence of the coupling function formula and parameters, in addition to the contribution of time-delay on the presence and stability of in-phase and anti-phase coordination patterns. The computation of this chapter were performed with the continuation package DDE-Biftool (v3.1.1) [81] under Matlab.

4.1 Comparison of different coupling terms with time-delay

In this section, we discuss the influence of coupling formulation on the stability of in-phase and anti-phase coordination patterns in the coupled HKB oscillators (4.1) as the frequency parameter ω increases, which is commonly interpreted as increasing in pacing frequency during an experiment [8, 47]. More precisely, we compare the influence of the neurologically motivated coupling proposed in [44], which is given by:

$$G(x_i, x_j) = \varepsilon \left((x_i - (1-r)x_{i\tau} - r x_{j\tau}) - \frac{\delta}{3}(x_i - (1-r)x_{i\tau} - r x_{j\tau})^3 \right), \qquad (4.2)$$

on the dynamics of coordination patterns to that of the phenomenological motivated coupling suggested in [16], which has the form:

$$F_{i,j} = (\dot{x_i} - \dot{x_{j\tau}}) \left(a + b(x_i - x_{j\tau})^2 \right) \qquad (4.3)$$

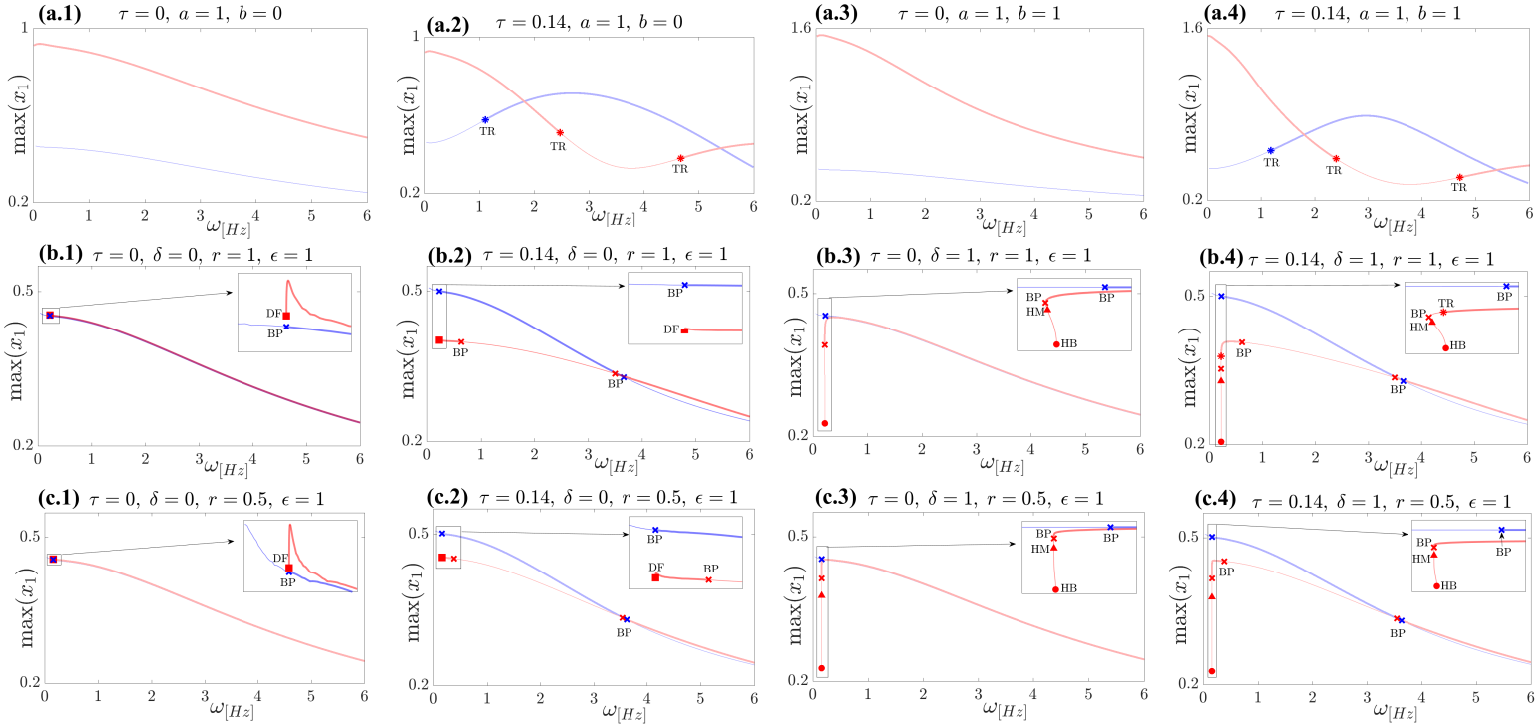

Figure 4.1: Influence of coupling on the stability of in-phase and anti-phase oscillations. Bifurcation diagrams of the in-phase and anti-phase periodic solutions in the parameter ω; panels**(a.1-4)** for system (4.5) of phenomenological coupling; panels(**b.1-4**) and (**c.1-4**) for system (4.4) of neurological coupling with $r = 1$ and $r = 0.5$, respectively; panels (**a-c.1**) and (**a-c.2**) for linear coupling ($b = 0$, $\delta = 0$) with zero ($\tau = 0$) and nonzero ($\tau = 0.14$) time-delay, respectively; panels (**a-c.3**) and (**a-c.4**) for nonlinear coupling ($b = 1$, $\delta = 1$) with zero ($\tau = 0$) and nonzero ($\tau = 0.14$) time-delay, respectively; *blue/red line* for $\max x(t)$ of the in-phase/anti-phase periodic solutions, respectively, (*thick* for stable *thin* for unstable); the labels $\bullet$, $*$, $\times$, $\blacktriangle$ and $\blacksquare$, indicate Hopf (HB), torus (TR), branching point (BP), homoclinic (HM) and degenerate family of equilibria (DF), respectively. For all panels, $\alpha = 12.457$, $\beta = 0.007095$ and $\gamma = 0.641$.

To this end, we performed numerical continuation (in the parameter ω) of the in-phase and anti-phase periodic solutions of system

$$\begin{aligned}
\dot{x_1} =& y_1, \\
\dot{x_2} =& y_2, \\
\dot{y_1} =& -\left(y_1(\alpha x_1^2 + \beta y_1^2 - \gamma) + \omega^2 x_1\right) \\
&+ \epsilon\left((x_1 - (1-r)x_{1\tau} - r x_{2\tau}) - \frac{\delta}{3}\left(x_1 - (1-r)x_{1\tau} - r x_{2\tau}\right)^3\right) \\
\dot{y_2} =& -\left(y_2(\alpha x_2^2 + \beta y_2^2 - \gamma) + \omega^2 x_2\right) \\
&+ \epsilon\left((x_2 - (1-r)x_{2\tau} - r x_{1\tau}) - \frac{\delta}{3}(x_2 - (1-r)x_{2\tau} - r x_{1\tau})^3\right),
\end{aligned} \tag{4.4}$$

corresponding to the neurological (4.5) coupling, and to the system

$$\begin{aligned}
\dot{x_1} =& y_1, \\
\dot{x_2} =& y_2, \\
\dot{y_1} =& -\left(y_1(\alpha x_1^2 + \beta y_1^2 - \gamma) + \omega^2 x_1\right) + (y_1 - y_{2\tau})\left(a + b(x_1 - x_{2\tau})^2\right) \\
\dot{y_2} =& -\left(y_2(\alpha x_2^2 + \beta y_2^2 - \gamma) + \omega^2 x_2\right) + (y_2 - y_{1\tau})\left(a + b(x_2 - x_{1\tau})^2\right),
\end{aligned} \tag{4.5}$$

corresponding to phenomenological (4.4) coupling. Figure 4.1 shows the bifurcation diagrams of in-phase and anti-phase periodic solutions; panels**(a.1-4)** for system (4.5) of phenomenological coupling; panels(**b.1-4**) and (**c.1-4**) for system (4.4) of neurological coupling with parameter values $r = 1$ and $r = 0.5$, respectively. For all panels, the intrinsic parameters values are $\alpha = 12.457$, $\beta = 0.007095$ and $\gamma = 0.641$, which have been estimated directly from experimental data [6]. The cases of linear coupling, corresponding to the parameter values $b = 0$ and $\delta = 0$, are depicted in panels (**a-c.1**) and (**a-c.3**); while the non-linear coupling cases, represented by the parameter setting $b = 1$ and $\delta = 1$, are illustrated in panels (**a-c.2**) and (**a-c.4**). Panels (**a-c.1-2**) correspond to the no-delay cases ($\tau = 0$), whereas, the non zero time-delay cases, represented by $\tau = 0.14$, are shown in panels (**a-d.3-4**). The delay $\tau = 0.14$ was chosen because it is well within the range $70 - 150$ ms that was reported for responses to continuous stimuli [47, 82]. We also refer the reader to [47] for more details regarding the influence of time-delay on the dynamics of system (4.5). The in-phase and anti-phase oscillations gain or lose stability via Hopf, torus,

branching point, homoclinic and degenerate family of equilibria which are labelled as $\bullet$, $*$, $\times$, $\blacktriangle$ and $\blacksquare$, respectively. In the branching point bifurcation, a single real Floquet multiplier crosses through 1 leading to a branch of periodic phase-locked solutions characterised by relative phase in the interval $(0, \pi)$. The degenerate family of equilibria is discussed in the next section.

Firstly, we comment on the stability of the in-phase and anti-phase periodic solutions. Considering the case of no delay, the bifurcation diagrams presented in Figure 4.1 panels (**a.1**) and (**a.3**) show that for the phenomenologically motivated coupling F there is a dominant state of anti-phase monostability in the parameter range $0 < \omega \leq 6$[Hz]. Whereas, for the neurologically motivated coupling G, shown in panels (**b-c.1**) and (**b-c.3**), bistability of both in-phase and anti-phase solutions is present on the same range. Under the effect of a non-zero time-delay, the dominant states of both couplings are broken into alternating regions of monostability and bistability of the in-phase and anti-phase solutions. The analysis shows that the neurologically motivated coupling is more consistent with the experimental findings (bistability for low frequencies) than the phenomenologically motivated coupling. The observation also affirms the importance of considering the effect of time-delay in the system in order to induce transitions of stability state that leads to the experimentally observed switch between the two states (0° and 180°) of the relative phase, as suggested in related dynamical and experimental studies [8, 18, 44, 47].

Furthermore, the in-phase and anti-phase periodic solutions of the neurologically motivated coupling exhibit monotonically decreasing amplitude as the natural frequency parameter ω increases. This behaviour can be observed for the linear and nonlinear coupling cases, with and without time-delay. Whereas, no such monotonicity can be noticed for the amplitude of the two coordination patterns of the phenomenologically motivated coupling. Whereas, the amplitude monotonicity doesn't persist for the in-phase and anti-phase solutions of the phenomenologically motivated coupling.

Moreover, there exists a dynamic of stationary stability with no stable periodic regime (see the discussion in the next section), that can also be noticed at small values, albeit for a narrow range, of the parameter ω, see the zoomed regions in panels (**c-d**) in Figure 4.1. The existence of stable stationery but not periodic regime demonstrates that system (4.4) with the neurological coupling might be used

to describe the dynamic of discrete movement behaviour in addition to rhythmic movement coordination.

The effect of time-delay on the regions of bistability between in-phase and anti-phase periodic solutions of system (4.5) with phenomenological coupling (4.3) has been discussed in [47]. It can be noticed from Figure 4.1 panels **(a.1-4)** (see also **Fig.1.** in [47]) that introducing non-zero delay into the phenomenological coupling (4.3) can result in non-monotonic amplitude behaviour for the in-phase and anti-phase oscillations. Whereas, for the neurologically motivated coupling (4.2), the in-phase and anti-phase coordination patterns consistently exhibit drop of oscillation amplitude as the frequency parameter ω increases for zero and non-zero delay [Figure 4.1 panels **(a.1-4)**]. The inverse amplitude-frequency relation is a typical feature of oscillatory movements that has been confirmed experimentally in various movement tasks with non-constrained amplitude [6, 12]. Based on this key feature, we focus in the following on the neurologically motivated coupling (4.2) and discuss the stability of in-phase and anti-phase coordination patterns that system (4.4) supports.

4.2 Dynamics of in-phase and anti-phase coordination patterns in the HKB model with neurologically motivated coupling coupled HKB system

In this section, we discuss the existence of in-phase and anti-phase periodic solutions of the system (4.4) with the neurologically motivated coupling and explore the dependence of stability of the two coordination patterns on the coupling parameters and time-delay. The coupling parameters in system (4.4) has the interpretations: ϵ is the strength of coupling, $r \in [0, 1]$ is the degree of crosstalk feedback and δ controls the nonlinearity of the coupling. The latter parameter was originally set to the value $\delta = 1$ [44], however, as we will demonstrate, varying this value provides more control on the desired properties of the in-phase and anti-phase stability. For the numerical computation, we consider the parameter setting fitted to the experimental

data, namely, $\alpha = 12.457$, $\beta = 0.007095$ and $\gamma = 0.641$.

4.2.1 Existence of anti-phase solutions

As it can be noticed in Figure 4.1 panels (**b-c**), the in-phase coordination pattern exists, but it is not always stable, for all values of the natural frequency parameter ω. However, there exists a small critical value ω_* such that the anti-phase periodic solution exists only within the parameter range $\omega \in [\omega_*, \infty)$. In this section, we give an explanation of the bifurcation mechanism leading to the occurrence of anti-phase periodic solutions of system (4.4). We present a theoretical analysis of the steady state of system (4.4) and numerical bifurcation analysis of the anti-phase periodic solution. We discuss the linear and nonlinear coupling cases separately as the bifurcation mechanisms underlying them are rather different.

4.2.1.1 The linear coupling

The linear coupling case is associated with parameter value $\delta = 0$, for which the system (4.4) takes the form:

$$\begin{aligned}
\dot{x_1} =& y_1, \\
\dot{x_2} =& y_2, \\
\dot{y_1} =& -\left[y_1(\alpha x_1^2 + \beta y_1^2 - \gamma) + \omega^2 x_1\right) + \epsilon\left(x_1 - (1-r)x_{1\tau} - r x_{2\tau})\right] \\
\dot{y_2} =& -\left[y_2(\alpha x_2^2 + \beta y_2^2 - \gamma) + \omega^2 x_2\right) + \epsilon\left(x_2 - (1-r)x_{2\tau} - r x_{1\tau})\right]
\end{aligned} \tag{4.6}$$

The steady state is determined by equating the right hand side of (4.6) to 0 (recall that for the steady state that $x_{1\tau} = x_1$ and $x_{2\tau} = x_2$) which leads to the system of linear equations :

$$\begin{aligned}
y_1 &= 0 \\
y_2 &= 0 \\
-\omega^2 x_1 + \epsilon r\left(x_1 - x_2\right)) &= 0 \\
-\omega^2 x_2 + \epsilon r\left(x_2 - x_1\right)) &= 0
\end{aligned} \tag{4.7}$$

The solution of this system satisfies the following relations

$$y_1 = y_2 = 0, \quad x_1 + x_2 = 0, \quad (2\epsilon r - \omega^2)(x_1 - x_2) = 0$$

Therefore, the steady state of the system is either only the trivial equilibrium $(0,0,0,0)$ for $(2\epsilon r - \omega^2) \neq 0$, or it consists of a family of non-isolated fixed points defined by the line

$$L = \{(x_1, x_2, y_1, y_2) \in \mathbb{R}^4 |\ x_1 + x_2 = 0,\ y_1 = 0,\ y_2 = 0\}$$

for $(2\epsilon r - \omega^2) = 0$. The degenerate case determines a barrier for the region of existence of the anti-phase solution in the parameter space.

The stability of the equilibrium $(0,0)$ for the delayed case can be concluded [81] from the roots of the characteristic equation

$$det(\Delta(\lambda)) = 0 \tag{4.8}$$

where $\Delta(\lambda)$ is the 4×4 matrix

$$\Delta(\lambda) = \lambda I_4 - \begin{bmatrix} 0 & 0 & 1 & 0 \\ 0 & 0 & 0 & 1 \\ -(\omega^2+\epsilon) & 0 & \gamma & 0 \\ 0 & -(\omega^2+\epsilon) & 0 & \gamma \end{bmatrix} - \begin{bmatrix} 0 & 0 & 0 & 0 \\ 0 & 0 & 0 & 0 \\ \epsilon(1-r) & \epsilon r & 0 & 0 \\ \epsilon r & \epsilon(1-r) & 0 & 0 \end{bmatrix} e^{-\lambda\tau} \tag{4.9}$$

due to the transcendental nature of (4.8) there are infinitely many eigenvalues. This may make the stability analysis of the DDEs much harder than that of ODEs [83].

On the other hand, an easier approach to explain the dynamics pre and post the degenerate case is to consider the dynamics in the finite dimensional case associated with zero delay ($\tau = 0$). We also focus on the dynamics defined on the the anti-phase plane:

$$P = \{(x_1, x_2, y_1, y_2) \in \mathbb{R}^4 |\ x_1 = -x_2,\ y_1 = -y_2\}, \tag{4.10}$$

which can be described by:

$$\begin{aligned} \dot{x_1} =& y_1, \\ \dot{y_1} =& -\left[y_1(\alpha x_1^2 + \beta y_1^2 - \gamma) + \omega^2 x_1\right] + \epsilon\left(x_1 - (1-r)x_1 + r x_1\right)) \end{aligned} \tag{4.11}$$

or

$$\begin{aligned} \dot{x_1} &= y_1, \\ \dot{y_1} &= -y_1(\alpha x_1^2 + \beta y_1^2 - \gamma) + (2\epsilon r - \omega^2)x_1 \end{aligned} \tag{4.12}$$

The resulting two-dimensional dynamics is easier to analyse and visualise compared to the dynamics in the full four-dimensional dynamics. The linearisation of system (4.12) at the equilibrium $(x_1, y_1) = (0, 0)$ has the Jacobean:

$$J_0 = \begin{bmatrix} 0 & 1 \\ (2\epsilon r - \omega^2) & \gamma \end{bmatrix} \tag{4.13}$$

with the eigenvalues:

$$\lambda_0 = \frac{\gamma \mp \sqrt{\gamma^2 + 4(2\epsilon r - \omega^2)}}{2} \tag{4.14}$$

Hence, depending on the sign of $(\omega^2 - 2\epsilon r)$, we can distinguish three different dynamics:

- $(\omega^2 > 2\epsilon r)$, for $\gamma > 0$ [as in our setting $\gamma = 0.641$] the trivial equilibrium $(0, 0)$ of (4.12) is unstable and surrounded by a stable limit cycle (as shown by the numerical continuation in Figure 4.2a), which represents the anti-phase solution. The phase portraits of the dynamics for this case is illustrated in figure Figure 4.2b. For $\gamma < 0$ the equilibrium is stable.

- $(\omega^2 = 2\epsilon r)$, in this case, there is no flow through the line $y_1 = 0$, which consists of a family of non-isolated equilibria. The phase portraits of the dynamics of this degenerate case are illustrated in figure Figure 4.2c.

- $(\omega^2 < 2\epsilon r)$, the trivial equilibrium $(0, 0)$ is of saddle type, and no limit cycle exists in the anti-phase plane. Therefore, the dynamic is not oscillatory in this case. The phase portraits of the dynamics of this case are illustrated in Figure 4.2d.

To explore further the degenerate case, where the system (4.12) is given by:

$$\begin{aligned} \dot{x_1} &= y_1, \\ \dot{y_1} &= -y_1(\alpha x_1^2 + \beta y_1^2 - \gamma), \end{aligned} \tag{4.15}$$

we analyse the stability of the degenerate family of non-isolated equilibria $\{(x_1, y_1) \in \mathbb{R}^2 : y_1 = 0\}$. The Jacobian matrix of system (4.15) at the degenerate equilibria is given by:

$$J = \begin{bmatrix} 0 & 1 \\ 0 & -(\alpha x_1^2 - \gamma) \end{bmatrix}$$

which has the eigenvalues:

$$\lambda_1 = 0, \quad \lambda_2 = \gamma - \alpha x_1^2$$

For $\alpha\,\gamma > 0$ (including the choice $\alpha = 12.457$ and $\gamma = 0.641$), the non-isolated equilibrium on $y_1 = 0$ is stable if $x_1 \in \left(\infty, -\sqrt{\frac{\gamma}{\alpha}}\right) \cup \left(\sqrt{\frac{\gamma}{\alpha}}, \infty\right)$; and unstable if $x_1 \in \left(-\sqrt{\frac{\gamma}{\alpha}}, \sqrt{\frac{\gamma}{\alpha}}\right)$.

The nullclines for this case are given by

$$\begin{aligned} &x\text{-nullcline:} \quad y_1 = 0 \\ &y\text{-nullcline:} \quad y_1 = 0 \quad \cup \quad \frac{\alpha}{\gamma} x_1^2 + \frac{\beta}{\gamma} y_1^2 = 1 \end{aligned}$$

The self intersections of the y-nullcline, corresponding to the intersection between the line $y_1 = 0$ and the ellipse $\frac{\alpha}{\gamma}x_1^2 + \frac{\beta}{\gamma}y_1^2 = 1$, are situated at $x_1 = \pm\sqrt{\frac{\gamma}{\alpha}}$, through which the family of the degenerate equilibria switches its stability.

The flow of system (4.15) is defined on the one-dimensional manifolds, in the anti-phase plane (4.10), determined by the system:

$$\frac{dy}{dx} = -\left(\alpha x_1^2 + \beta y_1^2 - \gamma\right) \tag{4.16}$$

Figure 4.2 illustrates the disappearance of anti-phase periodic orbit in the linear coupling case; panel(**a**) shows the bifurcation diagram of in-phase and anti-phase periodic solutions of the system (4.6) for representative parameter setting and zero time-delay; panels (**c-d**) illustrate representative phase portraits of the system (4.12) (corresponding to the dynamics on the anti-phase plane (4.10)) pre, at and post the critical frequency $\omega_* := \sqrt{2\epsilon r}$. For $\omega > \omega_*$, there exists a unique unstable equilibrium at $(0, 0)$ surrounded by a stable limit cycle representing the anti-phase periodic solution (see Figure 4.2(**b**)). As $\omega \to \omega_*^+$, the period of the anti-phase orbit increases to infinity and parts of the periodic orbit become closer to the x_1-nullcline

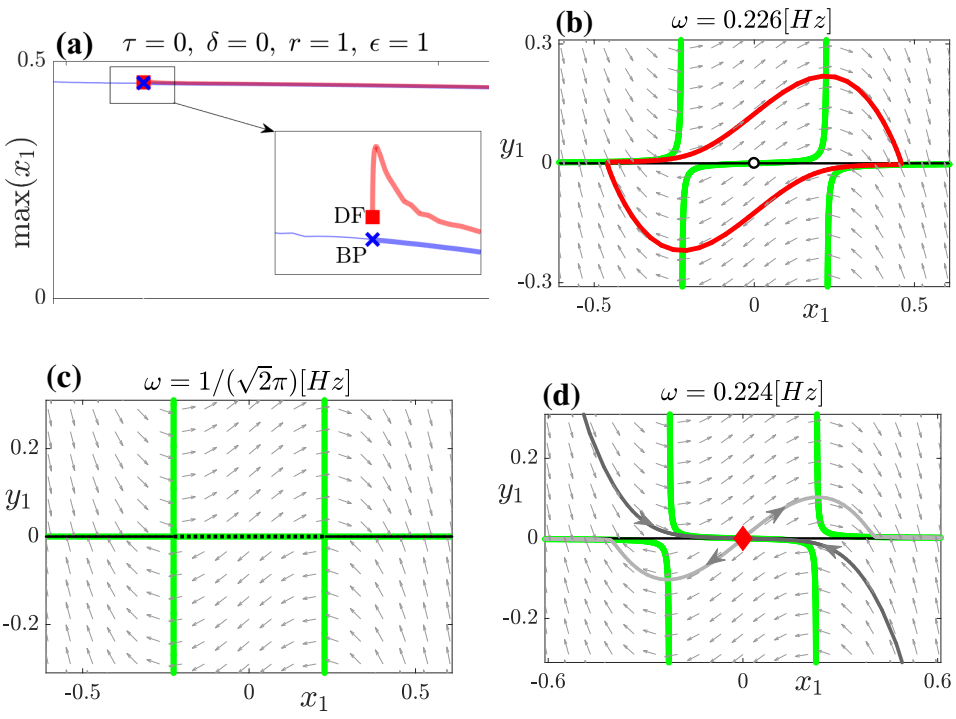

Figure 4.2: Existence of anti-phase periodic solution (linear coupling). Panel (**a**): Bifurcation diagram of in-phase and anti-phase periodic solutions ($\max x_1(t)$ against ω) for the linear coupling described by (4.6) and a representative parameter setting with no delay $\tau = 0$; *blue/red line* for in-phase/anti-phase periodic solutions, respectively, (*thick* for stable and *thin* for unstable); the labels $\times$ and $\blacksquare$ indicate branching point bifurcation and degenerate family of equilibria, respectively. Panels (**b-d**): phase portraits (y_1 against x_1) of the dynamics described by (4.12) on the anti-phase plane (4.10); (**b**) ($\omega > \omega_* = \sqrt{2\epsilon r}$) existence of anti-phase periodic orbit, (**c**) ($\omega = \omega_*$) the degenerate case of non-isolated equilibria, (**d**) ($\omega < \omega_*$) disappearance of anti-phase periodic orbit; *black/blue line* for x_1-nullcline and y_1-nullcline, respectively; *black empty dot* for unstable focus; *red cross* for saddle equilibria; *red line* for stable anti-phase periodic solution; *dark/light grey lines* for stable/unstable manifolds of the saddle point; *gray arrows* indicate the directional field of the dynamics. In the degenerate case, panel(**c**), a part of y_1-nullcline overlaps x_1-nullcline resulting in a family of non-isolated equilibria depicted in *solid/dashed black line*, corresponding to stable/unstable equilibria, respectively. The figure illustrates the disappearance of the anti-phase periodic solution, as the frequency parameter ω decreases, via a degenerate bifurcation of non-isolated equilibria along the line $y_1 = 0$.

and have flow that is slower in the x_1 direction than the other parts of the orbits. The anti-phase periodic orbit then disappears at the critical frequency $\omega = \omega_*$ since

the dynamics becomes one-dimensional having a family of non-isolated equilibria $y_1 = 0$ (at this value parts of the orbit become parts of the family of non-isolated equilibria, therefore, the anti-phase periodic orbit disappears). As the parameter ω decreases below the critical frequency (*i.e.* $\omega < \omega_*$), the one-dimensional dynamics near the degenerate non-isolated equilibria breaks into two-dimensional saddle point dynamics (as illustrated in Figure 4.2(**d**)). This explains the dynamic mechanism leading to the disappearance of anti-phase periodic oscillation for $\omega \in (0, \omega_*)$ in the linear coupling case.

4.2.1.2 The non-linear coupling

In this part, we discuss the existence of the anti-phase periodic solutions of the system (4.4), which is associated with the values $\delta \neq 0$. In fact, the proposed coupling function G has been suggested [44] to be nonlinear so that increasing the difference $(x_1 - (1-r)x_{1\tau} - rx_{2\tau})$ results in switching the sign of the coupling function G in (4.2). The different signs of G control the convergent and divergent properties of the flow in the state space and provide the possibility for multistable regimes [44]. This property requires that $\delta > 0$ to guarantee the change of the sign of G.

Again we present theoretical and numerical analysis of the steady state and anti-phase periodic solution for $\delta \neq 0$. The steady states of (4.4) is determined by the system of nonlinear equations

$$\begin{aligned} y_1 &= 0 \\ y_2 &= 0 \\ -\omega^2 x_1 + \epsilon\left(r(x_1 - x_2) - \frac{\delta}{3} r^3 (x_1 - x_2)^3\right) &= 0 \\ -\omega^2 x_2 + \epsilon\left(r(x_2 - x_1) - \frac{\delta}{3} r^3 (x_2 - x_1)^3\right) &= 0 \end{aligned} \tag{4.17}$$

addition and subtraction of last two equations lead to the following relations

$$y_1 = y_2 = 0, \quad x_1 + x_2 = 0, \quad (x_1 - x_2)\left((2\epsilon r - \omega^2) - \frac{2}{3}\epsilon\delta r^3 (x_1 - x_2)^2\right) = 0$$

Hence, the steady state of system (4.4) is either the trivial equilibrium $(0, 0, 0, 0)$ for $\frac{2\epsilon r - \omega^2}{\epsilon\delta r^3} \leq 0$, or consists of the trivial $(0, 0, 0, 0)$ in addition to two non-trivial

equilibria given by $(\pm x_e, \mp x_e, 0, 0)$ where

$$x_e = \sqrt{\frac{3}{8}\frac{(2\epsilon r - \omega^2)}{\epsilon\delta r^3}}$$

provided that $\frac{2\epsilon r-\omega^2}{\epsilon\delta r^3} > 0$. For $\epsilon, \delta > 0$ the non-trivial equilibria are defined in the range $0 < \omega < \omega_* = \sqrt{2\epsilon r}$ (corresponding to $\sqrt{\frac{3}{4\delta r^2}} > x_e > 0$). The steady-state undergoes a pitchfork bifurcation as the parameter ω varies and crosses the critical value $\omega_* = \sqrt{2\epsilon r}$ (corresponding to $x_e = 0$). At this parameter value, the non-trivial equilibria approach and merge in the trivial equilibrium. The pitchfork bifurcation for the nonlinear coupling in (4.4) can be considered as an unfolding of the degenerate bifurcation of non-isolated equilibria at $\omega = \omega_*$ for the linear coupling in (4.6).

Now, similar to the linear coupling case, we consider the finite dimensional dynamics associated with zero delay ($\tau = 0$) and focus on the dynamics on the anti-phase plane (4.10), which can be described by the system:

$$\begin{aligned} \dot{x_1} &= y_1, \\ \dot{y_1} &= -y_1(\alpha x_1^2 + \beta y_1^2 - \gamma) + (2\epsilon r - \omega^2)x_1 - \frac{8}{3}\epsilon\delta r^3 x_1^3 \end{aligned} \tag{4.18}$$

The linearisation of system (4.18) at the trivial equilibrium $(x_1, y_1) = (0, 0)$ has the same Jacobean and eigenvalues as in the linear case, given by (4.13) and (4.14), respectively. The pitchfork bifurcation occurs due to zero eigenvalue at $\omega = \sqrt{2\epsilon r}$ where the trivial equilibrium switches type from saddle to unstable node. On the other hand, the Jacobean of (4.18) at the non trivial equilibrium $(x_e, 0)$ is given by:

$$\begin{aligned} J_{x_1=x_e} &= \begin{bmatrix} 0 & 1 \\ (2\epsilon r - \omega^2) - 8\epsilon\delta r^3\left(\frac{3}{8}\frac{(2\epsilon r-\omega^2)}{\epsilon\delta r^3}\right) & \gamma - \alpha x_e^2 \end{bmatrix} \\ &= \begin{bmatrix} 0 & 1 \\ -2(2\epsilon r - \omega^2) & \gamma - \alpha x_e^2 \end{bmatrix} \end{aligned}$$

$$J_{x_1=x_e} = \begin{bmatrix} 0 & 1 \\ -2(2\epsilon r - \omega^2) & \gamma - \alpha x_e^2 \end{bmatrix} \tag{4.19}$$

and the eigenvalues are:

$$\lambda_{x_e} = \frac{(\gamma - \alpha x_e^2) \mp \sqrt{(\gamma - \alpha x_e^2)^2 - 8(2\epsilon r - \omega^2)}}{2} \tag{4.20}$$

The pair of complex eigenvalues becomes pure imaginary if $x_e = \sqrt{\frac{\gamma}{\alpha}}$. Recall that for $\epsilon, \delta > 0$ the non-trivial equilibria $(\pm x_e, 0)$ satisfy $x_e \in \left(0, \sqrt{\frac{3}{4\delta r^2}}\right)$. Therefore, if $\frac{\gamma}{\alpha} \in \left(0, \sqrt{\frac{3}{4\delta r^2}}\right)$, a Hopf bifurcation occurs along the branches of non-trivial equilibria at the parameter values $\omega_H = \sqrt{2\epsilon r}\sqrt{\left(1 - \frac{4}{3}\frac{\delta r^2 \gamma}{\alpha}\right)}$.

Since for $r \in [0, 1]$

$$\sqrt{\frac{3}{4\delta r^2}} > \sqrt{\frac{3}{4\delta}}$$

Therefore, the condition $\delta < \frac{3\alpha^2}{4\gamma^2}$ is sufficient to have $\frac{\gamma}{\alpha} \in \left(0, \sqrt{\frac{3}{4\delta r^2}}\right)$ and $\omega_0 \in (0, \sqrt{2\epsilon r})$, and hence, guarantees the occurrence of Hopf bifurcation at $\omega = \omega_H$ along the non-trivial equilibria branches. For our fix parameter setting the sufficient condition is $\delta < \frac{3}{4}\frac{\alpha^2}{\gamma^2} = \frac{3}{4}\left(\frac{12.457}{0.641}\right)^2 \approx 283$.

Numerical continuation analysis reveals that stable anti-phase periodic oscillation exists for some values of ω smaller than the critical value ω_*. Figure 4.3 illustrates the bifurcation diagram of the in-phase and anti-phase periodic solutions of system (4.4) for the same parameter setting in Figure 4.2 with nonlinearity $\delta = 1$, in addition to a number of phase portraits of the flow on the anti-phase plane (described by system (4.18)) corresponding to representative values of the parameter ω from panel (**a**). For $\omega > \omega_*$, stable periodic solution exists that is surrounding unstable focus at the origin $(0, 0)$ [panel (**c**)]. As the parameter ω decreases, the system undergoes pitch fork bifurcation at $\omega = \omega_*$, where two extra unstable nodes bifurcate from the trivial equilibrium which changes from focus to saddle point. Hence, for $\omega_H < \omega < \omega_*$, stable anti-phase periodic orbit surrounds a saddle and two unstable nodes [panel (**d**)]. As the parameter ω crosses the value ω_H, two small unstable periodic orbits (depicted in thin magenta) emanate from the two nodes which regain stability via Hopf bifurcation at $\omega = \omega_H$ [panel (**e**)]. As ω decreases, the small unstable periodic orbits expand and end at double homoclinic trajectory connected to the saddle point [panel (**f**)]. The homoclinic trajectory then breaks into another branch of large unstable periodic orbit (depicted in thin red line) surrounding the

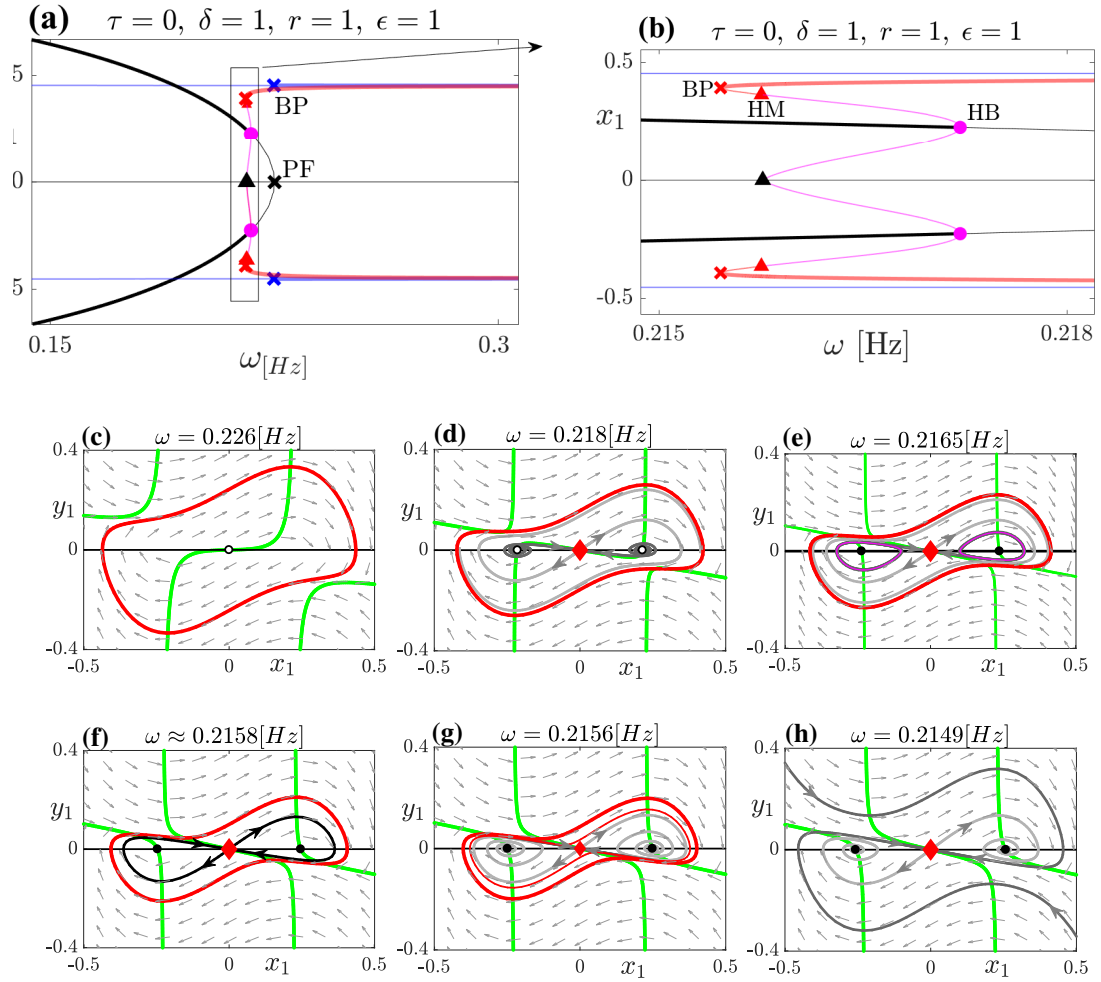

Figure 4.3: Existence of anti-phase periodic solution (nonlinear coupling). Panel (**a**): Bifurcation diagram of in-phase and anti-phase periodic solutions of system (4.4) ($\max x_1(t)$ and $\min x_1(t)$ against ω) for the representative parameters setting in Figure 4.2 with nonlinearity $\delta = 1$; *blue/red line* for in-phase/anti-phase periodic solutions, respectively, (*thick* for stable and *thin* for unstable); the labels •, × and ▲ indicate Hopf, branching point, and homoclinic bifurcation, respectively. Panels (**c-h**): phase portraits (y_1 against x_1) of system (4.18) on the anti-phase plane (4.10) as the frequency parameter ω decreases in panels (**a-b**); *black/blue line* for x_1-nullcline and y_1-nullcline, respectively; labels •/∘ indicate stable/unstable focus; × for saddle equilibrim; *red line* for anti-phase orbits (*thick* for stable and *thin* for unstable); *dark/light grey lines* for stable/unstable manifolds of the saddle point; *gray arrows* indicate the directional field of the dynamics.

three equilibria and enclosed by the stable periodic orbit [panel (**g**)]. Finally, the stable and unstable periodic orbits merge and collide in a saddle-node bifurcation

of limit cycles leaving only three equilibria with no periodic orbits in the anti-phase plane. Similar scenarios can be observed in the dynamics on the anti-phase plane for non-zero delay $\tau > 0$, which explains the disappearance of anti-phase oscillations for small values of ω in the non-linear case.

The dynamics observed in system (4.4) at small values of ω, albeit there is no stable periodic regime exists, could also be interesting from an application perspective. In fact, the nonlinearity of the coupling (4.2) provides global boundedness and convergence properties of the dynamics towards the stable steady regimes [44]. Furthermore, the basins of attraction of the two stable nodes regimes in the state space are separated by the stable manifold of the saddle point [see Figure 4.3 panel(**h**)]. This dynamic is suitable to describe discrete movement behaviours exhibiting threshold properties [9].

4.2.2 Influence of coupling parameters and time-delay on the stability of in-phase and anti-phase oscillations

In this part, we investigate the stability of in-phase and anti-phase coordination patterns and its dependence on the coupling parameters and time-delay. We present two-parameter continuation of the bifurcations of in-phase and anti-phase periodic solutions of system (4.4). We discuss the influence of time-delay and coupling parameters on the regions of bistability and monostability in the parameter space. Our aim is to identify the regions in parameter space that support the transition from bistable dynamics of in-phase and anti-phase periodic regimes to monostable in-phase oscillation.

4.2.2.1 The influence of time-delay

To explore the influence of time-delay on the stability, we performed two-parameter continuation of the bifurcations of in-phase and anti-phase periodic solutions in the time-delay and the strength and nonlinearity parameters of the coupling. The two-parameter bifurcation diagrams of the in-phase and anti-phase stability of system (4.4) is illustrated in Figure 4.4. Panel(**a**) shows the stability bifurcation diagram in the (τ, ϵ)-plane for $\delta = 0$, which illustrates the dependence of stability on the time-delay and coupling strength in the linear coupling case; while the dependence

of stability on time-delay and nonlinearity of the coupling is illustrated in panel(**b**), where the bifurcation diagram in the (τ, δ)-plane is depicted for $\epsilon = 1$. We only consider the half plane $\delta \geq 0$ to guarantee reversibility of the sign of the coupling function G as suggested in [44]. The other parameter setting is $\alpha = 12.457, \beta = 0.007095$, $\gamma = 0.641$, $\omega = 1$[Hz] and $r = 1$. The different stability regions of the periodic solutions are bounded by curves representing the loci of torus and branching point bifurcations in the parameter plane.

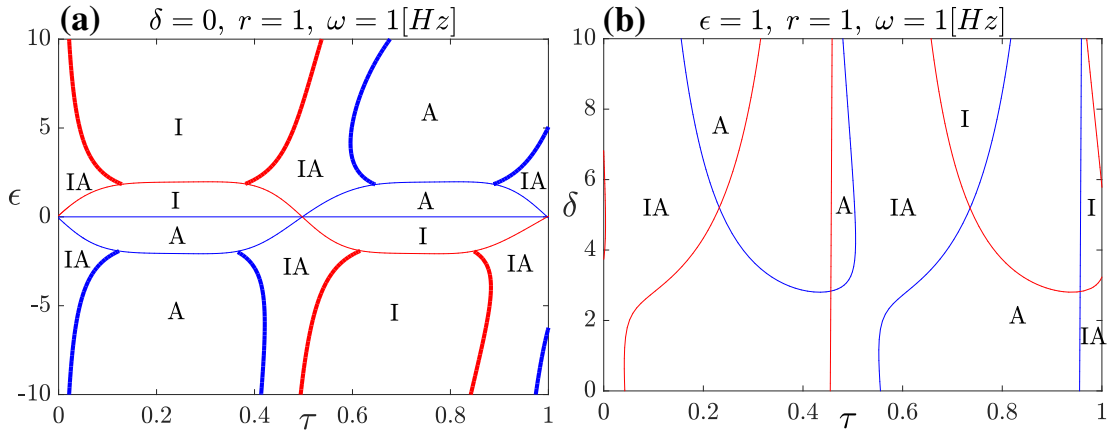

Figure 4.4: Influence of time-delay on stability of the in-phase and anti-phase oscillations. Two parameter bifurcation diagrams of the stability of in-phase and anti-phase oscillations of system (4.4) in the (τ, ϵ)-plane for $\delta = 0$ (**a**); and in the (τ, δ)-plane for $\epsilon = 1$ (**b**). The other parameter setting is $\alpha = 12.457, \beta = 0.007095$, $\gamma = 0.641$, $\omega = 1$[Hz] and $r = 1$. The labels (I and A) indicate, respectively, the existence of stable in-phase and anti-phase oscillations in the corresponding region. The *thick/thin lines* represent, respectively, the loci of torus and branching point bifurcations of in-phase (*blue*) and anti-phase (*red*) periodic solutions. Crossing these lines leads the corresponding periodic solution to loose or gain stability as Floquet multipliers crosses the unit circle. For torus bifurcation a pair of complex conjugated Floquet multipliers crosses the unit circle. While, for branching point bifurcation a single real Floquet multiplier crosses the unit circle through 1.

The bifurcation diagrams presented in Figure 4.4 show that for sufficiently small time-delay, bistability dynamic of in-phase and anti-phase periodic regimes exists for wide ranges of the coupling parameters ϵ and δ. For larger values of τ, torus or branching point bifurcation results in the existence of regions of monostable in-phase or anti-phase coordination pattern. As the time-delay increases, the regions of bistability and monostability alternate. It can also be noticed that the bifurcations

of in-phase and anti-phase coordination patterns alternate in the range of τ, which can be considered related to the relationship between the time-delay τ and the frequency ω [47].

4.2.2.2 The influence of coupling parameters

The bifurcation analysis in (τ, ϵ) and (τ, δ) parameter planes shows that for sufficiently small time-delay, the dynamics of the HKB system (4.4) at small frequency parameter value $\omega = 1$[Hz] supports bistable in-phase and anti-phase oscillations. The next step is exploring the ranges of the coupling parameters that support the transition from bistability dynamics to monostable in-phase periodic regime as the frequency parameter ω increases, which is commonly interpreted as increasing in pacing frequency during an experiment [8, 47].

Coupling nonlinearity

First, we consider the influence of coupling nonlinearity on the stability. To this end, we performed two-parameter continuation of the bifurcations of in-phase and anti-phase periodic solutions in the nonlinearity parameter δ and the natural frequency parameter ω.

Figure 4.5 illustrates two-parameter bifurcation diagrams of the stability of in-phase and anti-phase oscillations in the (ω, δ)-plane for $\delta \geq 0$. The computation was performed for the choices of time-delays $\tau = 0.08$[s] and $\tau = 0.14$[s] (representing the range $70 - 150$[ms] that was reported for responses to continuous stimuli [47, 82]) in addition to the two crosstalk degree values: $r = 0.5$ representing equally self- and mutual-feedback (corresponding to a moving effector equally influenced by the feedback of its own and the other effector positions); and $r = 1$ representing pure mutual- (with no self) feedback (corresponding to moving effector that is influenced only by the position of the other effector) [44]. The range of natural frequency parameter is $0 < \omega < 6Hz$, which is the frequency range explored in the related experimental studies [6, 12]. The other parameters setting is $\alpha = 12.457, \beta = 0.007095$, $\gamma = 0.641$ and $\epsilon = 1$.

The bifurcation diagrams in Figure 4.5 demonstrate that bistable regimes of in-phase and anti-phase oscillations exist for a small value of the frequency parameter ω

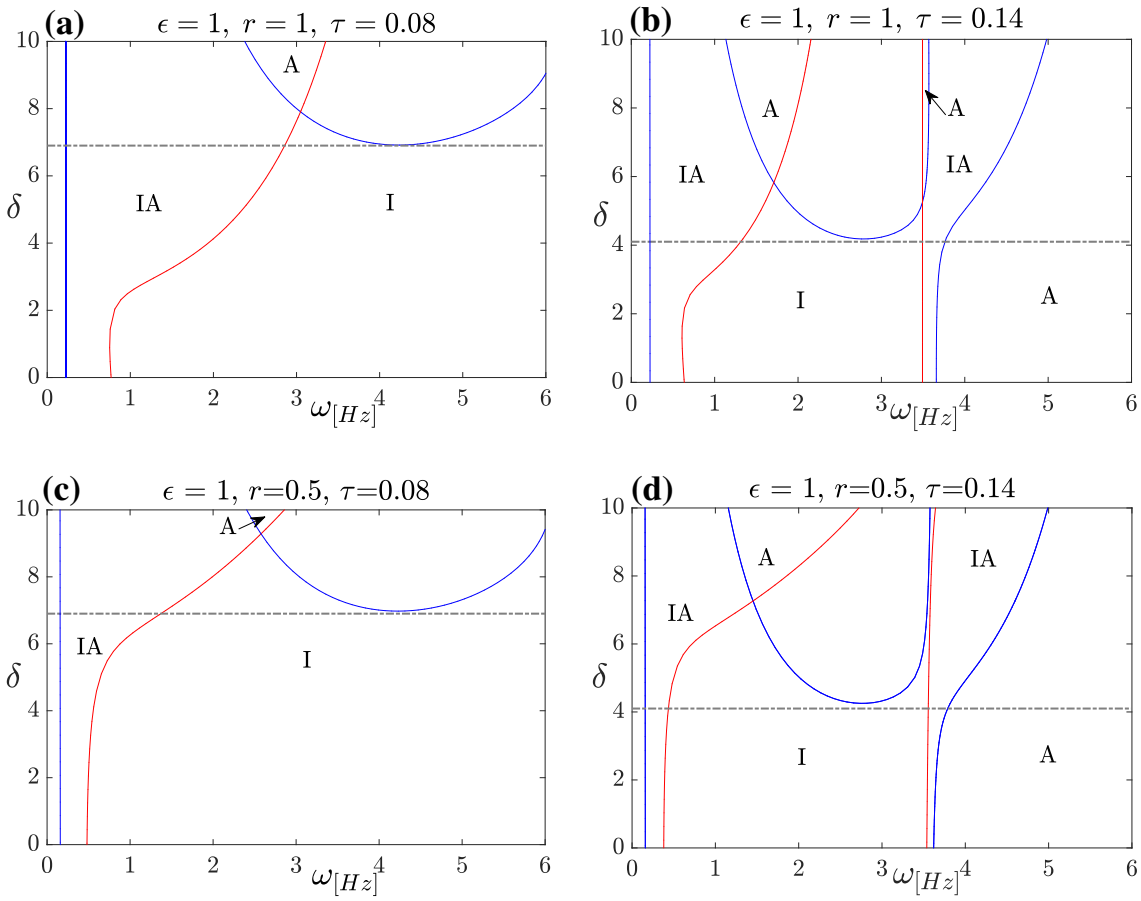

Figure 4.5: Influence of coupling nonlinearity on stability of the in-phase and anti-phase oscillations. Two parameter bifurcation diagrams of the stability of in-phase and anti-phase oscillations of system (4.4) in the (ω, δ) plane for $\tau = 0.08, 0.14$, $r = 1, 0.5$, $\epsilon = 1$, $\alpha = 12.457, \beta = 0.007095$ and $\gamma = 0.641$. The labels (I and A) indicate, respectively, the existence of stable in-phase and anti-phase oscillations in the corresponding region; The *solid curves* represent the loci of branching point bifurcation of in-phase (*blue*) and anti-phase (*red*) periodic solutions; *grey dashed line* indicates the critical nonlinearity level δ_* below which there is a transition from in-phase and anti-phase bistability dynamics to monostable in-phase periodic regimes as the frequency parameter ω increases.

in the regions labelled as (IA). As the parameter ω increases, the bistability regions are replaced by monostability regions via branching point bifurcation. For wide ranges of the nonlinearity parameter δ [in the regions labelled as (I)], the monostability is for in-phase oscillation. Hence, for sizable ranges of the parameter space,

the dynamics of system (4.4) supports the transition observed in the experiments from bistable to monostable coordination pattern. Furthermore, it can be noticed [panels (**a-c**)] that increasing the nonlinearity parameter δ, up to the critical nonlinearity level $\delta = \delta_*$ depicted in grey dashed line, results in a larger value of the critical frequency value at which the anti-phase oscillation loses its stability and the transition in coordination pattern happens. Above the critical nonlinearity value δ_*, the in-phase periodic solution loses its stability, as ω increases, via branching point bifurcation leading to stability transitions that were not observed in experiments. It can also be noticed that for long time-delay $\tau = 0.14$ [panels (**b**) and (**d**)] other stability transitions occur for $\omega > 3.5$[Hz] as the stability regions alter.

Coupling strength

In order to gain insight into the influence of the coupling strength parameter ϵ on the transition of stability described in Figure 4.5, we present one-parameter bifurcation diagrams in the frequency parameter ω. The bifurcation diagrams are depicted in Figure 4.6 for weak, moderate and large coupling strengths $\epsilon = 0.2$, 1 and 5. The values of nonlinearity parameter δ is chosen to be close to the critical level δ_* ($\delta = 6$ for $\tau = 0.08$ and $\delta = 4$ for $\tau = 0.14$) to monitor the influence of ϵ on the wide range of bistability before the critical transition to monostable anti-phase oscillation occurs. The figure shows that increasing the strength of the coupling leads to an increase in the difference between oscillation amplitude of the in-phase and anti-phase periodic solutions. Furthermore, [apart from Figure 4.6b for $\epsilon = 5$ where the anti-phase solution emanates from Hopf bifurcation and the in-phase solution loses and regains stability before the anti-phase coordination pattern loses stability], the bifurcation diagrams for $r = 1$ show that changing the strength parameter ϵ does not significantly change the range of bistability or the critical transition of stability. Whereas, for $r = 0.5$ increasing the strength parameter ϵ leads to delay in the critical transition frequency as the parameter ω increases.

4.3 Summary

In this chapter, we investigated analytically and numerically the dynamics of two coupled HKB oscillators that can be used to model movement coordination be-

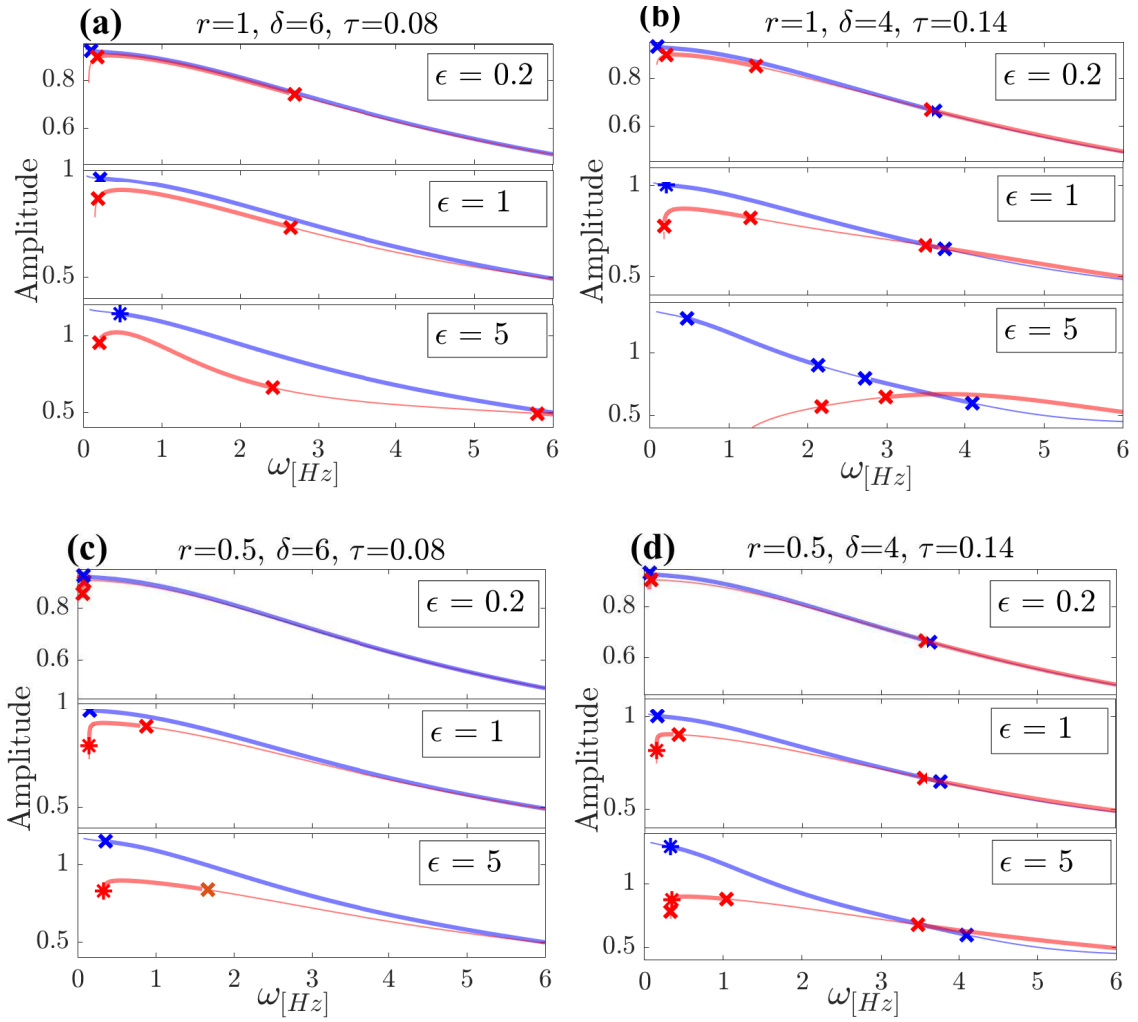

Figure 4.6: Influence of coupling strength on stability of the in-phase and anti-phase oscillations. Bifurcation diagram of stability of the in-phase and anti-phase oscillations of system (4.4) in the frequency parameter ω for the coupling strength values $\epsilon = 0.2$, 1, 5 and nonlinearity close to the critical level δ_* shown in Figure 4.5. *Blue/red line* for $\max x(t)$ of the in-phase/anti-phase periodic solutions, respectively, (*thick* for stable *thin* for unstable); the labels $*$ and $\times$ indicate torus and branching point bifurcations, respectively. For all panels, $\alpha = 12.457$, $\beta = 0.007095$ and $\gamma = 0.641$.

haviour, considering physically relevant intrinsic parameter setting that is consistent with experimental data [6].

Comparing two different coupling formulations involving the effect of time-delay,

namely the phenomenologically motivated coupling (4.3) and the neurologically motivated coupling (4.2), our analysis shows that the latter coupling seems to demonstrate more consistency with the empirical observations in terms of exhibiting the desired amplitude-frequency relation observed in many oscillatory movements experiments [6]. The drop of oscillation amplitude of the in-phase and anti-phase periodic solutions of system (4.4) is shown to be persistent in most of the explored parameter space (see Figure 4.1 and Figure 4.6).

In addition, numerical bifurcation analysis of the in-phase and anti-phase periodic solutions reveals that the stability transition of the coordination dynamics (from bistable in-phase and anti-phase oscillations to monostable in-phase periodic regime) as the natural frequency parameter ω increases is well captured by the HKB system (4.4) with neurologically motivated coupling (see Figure 4.1 and Figure 4.6). This change in the stability provides an explanation to the frequency-induced transition of the movement coordination from antisymmetrical to symmetrical pattern, which has been observed experimentally in rhythmic movements behaviour [19]. The numerical bifurcation analysis shows that considering the time-delay in the coupling function have significant effects on altering the regions of bistability and monostability in the parameter space. Our analysis also shows that reducing the time delay (*e.g.* by increasing the perceptual intention) can lead to increase in the frequency range of bistability.

Furthermore, varying the nonlinearity of the coupling (instead of fixing it as it was originally proposed in [44]) has shown an effect on extending the ranges of bistability in the natural frequency parameter space (see Figure 4.5). The effect of coupling strength, on the other hand, on the bistability regions is almost modest for the pure mutual-feedback case $r = 1$. However, coupling strength effect becomes more pronounced as the self-feedback is involved: the larger the coupling strength, the wider the range of bistability (see Figure 4.6). A possible interpretation for the effect of coupling strength of the different degree of cross-talk is that as the moving effector in a joint action task becomes more relying on the self-position feedback, a stronger degree of coupling is required to maintain stable anti-phase synchronisation pattern of the movement coordination at higher frequencies. Overall, our analysis shows that varying the strength, nonlinearity and cross-talk degree of the coupling can control the relative ranges of bistability and monostability of the coordination

patterns of the HKB system, which is essential for comparison purposes to the experimental observations of rhythmic movement coordination.

Finally, our analysis also reveals that, for sufficiently small values of the parameter ω, the HKB system (4.4) of neurologically motivated coupling supports stationary bistability with no stable periodic regimes (see Figure 4.3). This dynamic might be used to provide descriptions to the coordination dynamics of some discrete bimanual movements and joint-actions [9].

Chapter 5

Discussion

In this chapter, we discuss the results of our analysis of the dynamics of the Haken-Kelso-Bunz (HKB) model and the Jirsa-Kelso excitator (JKE) highlighting the contribution of these results to the movement coordination field.

The HKB hybrid oscillator has been shown to have periodic regimes that arise from Hopf bifurcation, as the damping (γ) of the oscillation switches sign, and they disappear at a saddle-node bifurcation of limit cycles or via a heteroclinic cycle of infinite magnitude [46]. To identify the stability boundaries of the steady state and periodic regimes in the parameter space, we use numerical continuation in chapter 2 to follow the loci of the reported bifurcations in the single HKB oscillator in different two-parameter planes. The bifurcation diagrams presented in Figures 2.2 - 2.4 show the different types and stability of the model solutions. Hence, all possible dynamic states that the single HKB oscillator model supports has been characterised and associated with the corresponding parameter regime.

In addition, the possible periodic regime of the HKB single oscillator can be approximated by an oscillatory solution of constant amplitude (*e.g.* by averaging the slowly varying amplitude of the oscillation over time) [8, 48]. In chapter 2, we analyse the dynamics of the approximating oscillatory solution obtained from averaging the amplitude-phase dynamics of the single HKB oscillator over $T = \frac{2\pi}{\omega}$. The analysis shows that the averaged amplitude-phase system can capture the dynamics of the single HKB system near a generic Hopf bifurcation via pitchfork bifurcation of the amplitude steady state. Furthermore, Figure 2.5 illustrates that the oscillatory solution of the averaged amplitude-phase system approximates very well the actual

periodic solution of the HKB oscillator computed numerically for parameter setting that has been fitted directly to experimental data [6]. Therefore, our analysis confirm that the periodic regime of the single HKB oscillator can be well represented by the approximating oscillatory solution for physically related parameter setting.

Relatedly, a numerical continuation of the periodic solutions in the natural frequency parameter ω (Figure 2.5 **a**) also confirms that the periodic regime of the single HKB oscillator for the fitted parameter setting exhibits a drop of oscillation amplitude as the frequency parameter increases. This inverse amplitude-frequency relation has been experimentally observed in many oscillatory movements [6, 12] and it was the main dynamical feature motivating the development of the hybrid HKB oscillator formed by combining the nonlinear damping terms of Van der Pol and Rayleigh oscillators [8].

Our overall analysis of the single HKB hybrid oscillator confirms the suitability of the system to describe the dynamics of a rhythmically moving effector, as well as the intrinsic properties of the coordination dynamics in bimanual movements and joint actions.

Furthermore, the averaged amplitudes of the two oscillators in the full HKB model [8] have a similar dependence [48] on the frequency parameter ω to that of the single HKB oscillator [6]. However, considering the effect of time-delay [16, 47] in the phenomenologically motivated coupling proposed in the original HKB model [8] can lead to a breach of the monotonic decrease in the oscillation amplitude as the frequency parameter increases (see panels a-b Fig.1 in [47]). This effect has been confirmed by the analysis of chapter 4 (see Figure 4.1 **a.1-4**) showing a limitation of the phenomenologically motivated version of coupling to be in agreement with the experimentally observed inverse amplitude-frequency relation.

On the other hand, our analysis in chapter 4 shows that coupling two HKB oscillators by the neurologically motivated coupling proposed in [44] can result in periodic regimes that exhibit the desired amplitude-frequency relation consistently for wide ranges of the coupling parameters with zero and nonzero time-delay (see Figure 4.1 and Figure 4.6).

Furthermore, the numerical bifurcation analysis we presented in Figure 4.5 and Figure 4.6 demonstrates that the periodic regime of the HKB model coupled by the neurologically motivated coupling with non-zero delay $\tau > 0$ undergoes transitions

from bistable in-phase and anti-phase coordination patterns to monostable in-phase coordination mode as the frequency parameter increases. This suggests that the latter coupled system can capture the switch from antisymmetric to symmetric coordination pattern that has been observed in many movements experiments [34] and inspired the development of the HKB model [8, 84] in addition to the amplitude-frequency relation. The analysis also confirms the importance of considering the effect of time-delay in the coupling dynamics to support the desired transition of coordination pattern stability.

Moreover, the bifurcation diagrams in Figure 4.5 and Figure 4.6 also show that varying the coupling parameters, including the degree of crosstalk feedback, can change the proportional ranges of coordination bistability and monostability controlling the critical frequency at which the pattern transition occurs. This flexibility of the parameter regimes is essential for comparison purposes to the experimental observations of rhythmic movement coordination. Additionally, Figure 4.5 and Figure 4.6 demonstrate that decreasing the cross-talk degree r reduces relatively the region of anti-phase stability in the parameter space. This observation is in agreement with similar result of [44], which offers a possible explanation for the decreased stability of the anti-phase coordination pattern in split brain patients (patients suffering from epilepsy whose corpus callosum has been surgically sectioned [44, 45]). Such patients have a tendency to switch into in-phase movement pattern from other specific phase patterns they are instructed to maintain [45].

What is more, the theoretical and numerical analysis we presented reveals that for small values of the parameter ω, the HKB system with neurologically motivated coupling undergoes stationary bistability with the absence of periodic regimes. Such dynamics can be considered for modelling discrete movement behaviours [9] going beyond the original purpose of developing the HKB model to account for rhythmic movement patterns [8].

The JKE model has been proposed to account for a variety of experimental phenomena in rhythmic and discrete movements using the same modelling framework [9]. The modelling approach of the JKE was motivated by the excitable FitzHugh-Nagumo (FHN) system [40], which can be transformed to the JKE system by a smooth nonlinear transformation [9]. Although the dynamics of the JKE and FHN models are equivalent (for finite separation of time-scales), the systems' state vari-

ables, including the shared one, have different physical interpretations (see the discussion following to Figure 2.6). To showcase the dynamic equivalence of the two models (for $\varepsilon > 0$), we present in chapter 2 a number of representative bifurcation diagrams of the two models, in addition to 3D visualisation of the shared dynamics illustrated by projecting the phase-plane dynamics of both models on a 3D hypersurface.

In order to characterise all possible dynamic states supported by the JKE model, as well as their dependence on model parameters, we present in chapter 2 two-parameter bifurcation diagram of the JKE system (see Figure 2.10) and associate the different ranges in the model parameter-plane with the corresponding dynamics the system supports. Based on this analysis, the parameter regimes of the JKE model corresponding to mono- and bistable fixed-points dynamics in addition to stable periodic regime dynamics (describing, respectively, discrete and rhythmic movements [9]) has been identified. Knowing the ranges in the model parameter-space where a specific type and stability of solution exist could greatly facilitate identifying the model parameter regime that is suitable for a particular experiment setting.

Furthermore, the separation of time-scales is a key characteristic feature of the JKE model that provides a threshold property of the model dynamic represented by a separatrix trajectory which partitions the flow in the phase space [9]. According to this threshold property, the JKE model proposes that movements are initiated as the separatrix in the phase space is crossed as a consequence of external stimulation [13]. In chapter 2, we present a rescaled formulation of the JKE system that has the same ratio of time-scale separation as the FHN system facilitating the comparison of the slow and fast phenomena in the two models. In addition, we propose in chapter 2 an approximated representation of the JKE system that exhibits qualitatively similar dynamics to that of the JKE model.

Moreover, despite the equivalence of the JKE and FHN models for finite separation of time scales ($\epsilon > 0$), the slow-fast analysis in the singular limit $\varepsilon = 0$, that we present in chapter 2, reveals that a number of slow-fast characteristic features (such as canards phenomena) in the two models are quite distinct. More precisely, the slow-fast analysis reveals significant differences between the JKE and FHN systems in terms of the boundedness of flow along the fast layers and the slow flow

along the critical manifolds. These differences can be attributed to the breach of the equivalence transformation between the two models at the singular limit $\varepsilon = 0$. Consequently, the infinite growth of oscillation amplitude in the canard explosion of the JKE model is shown to be induced by an unbounded repelling part of the critical manifold the model followed for a considerable period of time by the canard cycles. Although such unbounded growth in oscillation amplitude cannot be observed in a physical system, it can have significant consequences for the application of the JKE model (*e.g.* for design and development of virtual players in joint action tasks [46]).

In order to investigate the dynamical mechanisms organising the canard solutions in the JKE system, which are different from the classical well understood mechanisms of the classical FHN model, we carry out an analysis using a combination of Poincaré sphere projection and blow-up technique. The presented analysis gives an explanation to the return mechanism of the unbounded canard periodic orbits in the singular case, $\varepsilon = 0$. The geometric approach we presented might be also applicable for other models exhibiting unbounded growth of canard cycles such as the aircraft ground dynamics model [69] and the earthquake faulting model [70, 71].

The presented slow-fast analysis shows that the transition between different classes of movements described by the JKE model can also be analysed and understood in terms of the slow-fast nature of the model dynamics controlled by the time-scale parameter ε. For instance, the relaxation oscillations might have very long periods and can be viewed, for sufficiently small values of $\varepsilon \ll 1$, as two almost steady states connected by fast transitions between them. This suggests an alternative approach to describe the transition between discrete and rhythmic movements, in addition to that induced by changing the parameters a and b.

Finally, our overview of different approaches to defining the maximal canards of the JKE model shows that the periodic orbit including the trajectory segment that is tangent to the asymptotic nonhyperbolicity or that has the maximal following time to the repelling critical manifold might be considered as the most representative candidate of the maximal canard. The trajectory segment described here can have a special interpretation for the movement dynamics as it represents the repelling slow manifold that separates the flow directions in the phase space. This separatrix trajectory form a threshold in the model state space that is counted for the occurrence of different movement performances following an external stimulus

[9]. For instance, a sufficiently strong stimulus can lead a movement trajectory to cross the separatrix resulting in a long transient movement, while, a weak stimulus might lead only to short transient if the movement dynamics, initiated close to stable steady state, has not been sufficiently excited to exceed the threshold [9]. The latter movement behaviour is described (in the movement coordination literature) as *false start* [9], which is one of the main predictions of the JK-excitator model that has been experimentally examined and validated [13].

Chapter 6

Conclusions and Future Directions

6.1 Conclusions

This thesis aimed to investigate systematically the dynamical properties of two models of movement coordination, namely the Haken-Kelso-Bunz (HKB) model and the Jirsa-Kelso excitator (JKE). We explored the parameter regimes of the single HKB oscillator and the JKE system identifying the different types and stability of solutions the models support and associating them with the corresponding behaviours of movement coordination. Furthermore, a detailed analysis of the canard phenomenon in the JKE system reveals that the dynamical mechanisms organising the canard cycles in JKE system have different geometrical properties comparing to that known for the equivalent FitzHugh-Nagumo (FHN) model. We also suggest a combination of slow-fast analysis, projection onto the Poincaré sphere and blow-up method to explain the canard organising mechanisms. The phenomena can have possible implications for the description of the transition between discrete and rhythmic movements. However, further empirical studies in relevant movement tasks would be required to validate these observations.

Moreover, we demonstrate that the periodic regimes of two HKB oscillators coupled by the neurologically motivated coupling can consistently exhibit the experimentally observed in-phase and anti-phase bistability patterns in addition to the amplitude-frequency relation that have been reported in many empirical studies of rhythmic movement coordination. Our analysis also highlights some parameter ranges for which the model supports the dynamics of discrete movement, which ex-

tends the class of movements that the HKB model might be considered to count for.

6.2 Future Directions

The analyses and results of this thesis open a venue for further directions which form a basis for future work relating to movement coordination and other real-life models. Here we highlight some of these directions:

- Analysing the effect of heterogeneity in the intrinsic and coupling parameters of the HKB model, with the neurologically motivated coupling, on the stability of the oscillation phase patterns and the properties of the oscillation amplitude.
- Investigating the effect of coupling (the phenomenologically vs the neurologically motivated couplings) on the dynamics of two coupled JK-excitators and considering the possible implication of the resulted dynamics to the modelling of discrete and rhythmic movement coordination.
- Investigating the existence of canard solutions in the coupled JKE systems and exploring the dynamical mechanisms organising such phenomena.
- Applying the presented approach to analyse the canard cycles near infinity to explain the similar canard behaviours in other real-life models, e.g. the aircraft ground dynamics model [69] and the earthquake faulting model [70, 71].

Appendices

Appendix A

Some Dynamical Systems Concepts

A.1 Geometric singular perturbation theory

A fast-slow vector field (or (m, n)-fast-slow system) is a system of ordinary differential equations taking the form [63, 64] (A more general definition can be found in [65])

$$\begin{aligned} \varepsilon \dot{x} = \quad \varepsilon \frac{dx}{d\tau} &= f(x, y, \varepsilon) \\ \dot{y} = \quad \frac{dy}{d\tau} &= g(x, y, \varepsilon) \end{aligned} \tag{A.1}$$

where $(x, y) \in \mathbb{R}^m \times \mathbb{R}^n$ are state-space variables, and ε is a small parameter $0 < \varepsilon \ll 1$ representing the ratio of time scales. The functions $f : \mathbb{R}^m \times \mathbb{R}^n \times \mathbb{R} \to \mathbb{R}^m$ and $g : \mathbb{R}^m \times \mathbb{R}^n \times \mathbb{R} \to \mathbb{R}^n$ are assumed to be sufficiently smooth. The x variables are called fast variables, and the y variables are called slow variables. Furthermore, by switching from the slow time scale τ to the fast time scale $t = \frac{\tau}{\varepsilon}$, system (A.1) can be rescaled to the equivalent form:

$$\begin{aligned} x' = \frac{dx}{dt} = \quad & f(x, y, \varepsilon) \\ y' = \frac{dx}{dt} = \quad & \varepsilon g(x, y, \varepsilon) \end{aligned} \tag{A.2}$$

Considering the limit case $\varepsilon = 0$, the slow time system (A.1) leads to the n-dimensional differential-algebraic system known as *slow subsystem* to the *reduced problem*

$$\begin{aligned} 0 &= f(x, y, 0) \\ \dot{y} &= g(x, y, 0) \end{aligned} \tag{A.3}$$

The flow of (A.3) is called the *fast flow*. On the other hand, the fast time system (A.2) leads to the m-dimensional *fast subsystem* or *layer equations*, in the limit case $\varepsilon = 0$, which read

$$\begin{aligned} x' &= f(x, y, 0) \\ y' &= 0 \end{aligned} \tag{A.4}$$

The flow of (A.4) is referred to as the *slow flow*.

The set

$$C_0 = \{(x, y) \in \mathbb{R}^m \times \mathbb{R}^n : f(x, y, 0) = 0\} \tag{A.5}$$

is called the critical manifold. The critical manifold corresponds to the family of equilibria of the fast subsystem (A.4). A subset of the critical manifold $C_{0,h} \subset C_0$ is *normally hyperbolic* if all $p = (x^*, y^*) \in C_{0,h}$ are hyperbolic equilibria of the layer problem (A.4), *i.e.* all eigenvalues of the Jacobian $D_x f$ evaluated at each $p \in C_{0,h}$ have non-zero real part. Furthermore, a normally hyperbolic subset of the critical manifold $C_{0,a} \subset C_0$ is called *attracting* if all eigenvalues of the Jacobian $D_x f$ have negative real parts for each $p \in C_{0,a}$; similarly, $C_{0,r} \subset C_0$ is called *repelling* if all eigenvalues have positive real parts for each $p \in C_{0,r}$. If the normally hyperbolic subset of the critical manifold $C_{0,s} \subset C_0$ is neither attracting nor repelling, it is described to be of *saddle* type.

Away from the critical manifold, the flow of the slow-fast *full system* (A.1) follows the fast flow of the layer equations. However, close to a hyperbolic critical manifold $C_{0,h} \subset C_0$, the full system flow follows the slow flow of the reduced problem (A.3), which persists for sufficiently small $\varepsilon > 0$ on a locally invariant manifold described by the following main theorem of the GSPT.

Theorem A.1 (**Fenichel's Theorem**). *Suppose $C_h = C_0$ is a compact normally hyperbolic submanifold (possibly with boundary) of the critical manifold C_0 (A.5) and that $f, g \in C^r (r < \infty)$. Then for $\varepsilon > 0$ sufficiently small, the following hold:*

(F1) There exists a locally invariant manifold C_ε diffeomorphic to C_0. Local invariance means that trajectories can enter or leave C_ε only through its boundaries.

(F2) C_ε has Hausdorff distance $\mathcal{O}(\varepsilon)$ (as $\varepsilon \to 0$) from C_0.

(F3) The flow on C_ε converges to the slow flow as $\varepsilon \to 0$.

(F4) C_ε is C^r-smooth.

(F5) C_ε is normally hyperbolic and has the same stability properties with respect to the fast variables as C_0 (attracting, repelling, or of saddle type).

(F6) C_ε is usually not unique. In regions that remain at a fixed distance from ∂C_ε, all manifolds satisfying (F1)-(F5) lie at a Hausdorff distance $\mathcal{O}\left(e^{-K/\varepsilon}\right)$ from each other for some $K > 0$, $K = \mathcal{O}(1)$.

Note that all asymptotic notation refers to $\varepsilon \to 0$. The same conclusions as for C_0 hold locally for its stable and unstable manifolds:

$$W^{\mathrm{s}}_{\mathrm{loc}}(C_0) = \bigcup_{p \in C_0} W^{\mathrm{s}}_{\mathrm{loc}}(p), \qquad W^{\mathrm{u}}_{\mathrm{loc}}(C_0) = \bigcup_{p \in C_0} W^{\mathrm{u}}_{\mathrm{loc}}(p)$$

where we view points $p \in C_0$ as equilibria of the fast subsystem. These manifolds also persist for $\varepsilon > 0$ sufficiently small: there exist local stable and unstable manifolds $W^{\mathrm{s}}_{\mathrm{loc}}(C_\varepsilon)$ and $W^{\mathrm{u}}_{\mathrm{loc}}(C_\varepsilon)$, respectively, for which conclusions (F1)-(F6) hold if we replace C_ε and C_0 by $W^{\mathrm{s}}_{\mathrm{loc}}(C_\varepsilon)$ and $W^{\mathrm{s}}_{\mathrm{loc}}(C_0)$ (or similarly by $W^{\mathrm{u}}_{\mathrm{loc}}(C_\varepsilon)$ and $W^{\mathrm{u}}_{\mathrm{loc}}(C_0)$).

The *Hausdorff distance* mentioned in the theorem is defined between two nonempty sets $V, W \subset \mathbb{R}^{m+n}$, as

$$d_H(V, W) = \max\left\{ \sup_{v \in V} \inf_{w \in W} \|v - w\| \,,\, \sup_{w \in W} \inf_{v \in V} \|v - w\| \right\} \tag{A.6}$$

A representative of the manifolds C_ε, described in the conclusion of Fenichel's theorem A.1, is referred to as the *the slow manifold*, on which the flow of the full system of fast time scale (A.2) has speed that tends to 0 as $\varepsilon \to 0$. However, the slow manifold C_ε is not uniquely represented, though, all possible choices C_ε lie within a Hausdorff distance $\mathcal{O}\left(e^{-K/\varepsilon}\right)$ from each other for some $K > 0$.

To obtain an analytical expression for the slow flow on a hyperbolic critical manifold C_0, consider the algebraic equation in (A.3). Since all the points $p \in C_{0,h}$ are hyperbolic, the Jacobian $(D_x f)(p, 0)$ is invertible and the slow flow in $\mathbb{R}^{m+n}$ restricted on $C_{0,h}$ can be described by

$$\begin{aligned} \dot{x} &= \pm \left(D_x f\right)^{-1} \left(D_y f\right) g \\ \dot{y} &= g \end{aligned} \tag{A.7}$$

Furthermore, the *implicit function theorem* implies that $C_{0,h}$ can be locally described by the graph of a function $h(y) = x$. Hence, the slow flow of the reduced problem (A.3) can be expressed in the dynamics of slow variables y as

$$\dot{y} = g(h(y), y, 0) \tag{A.8}$$

At nonhyperbolic points, the conclusions of Fenichel's theorem A.1 breaks down and since the Jacobian $(D_x f)(q, 0)$ is not invertible, the implicit function theorem is no longer satisfied. Such points of the critical manifold are called singular points and denoted by $C_{0,s}$. A typical example of a singular point is the fold (saddle-node bifurcation), for which the critical manifold C_0 is tangential to the fast flow of the layer equations. Another possible tangential singularity is the self-intersection of a critical manifold (*e.g.* transcritical bifurcation). Moreover, the blow-up method [50, 66, 75] can be used to desingularise the slow flow at nonhyperbolic points allowing Fenichel's theorem to be applied after regaining local hyperbolicity for $C_{0,s}$.

A.2 Canard Theory

Canard phenomena occur in various physical, chemical and biological applications involving multiple time scales [50, 69]. The term *canard explosion* refers to a rapid transition, over exponentially small variation of a parameter, from a small amplitude limit cycle to a relaxation oscillation via a family of *canard cycles*, which follow a stable slow manifold until crossing a small neighborhood of a bifurcation point of the critical manifold, and then follow an unstable slow manifold for a considerable period of time [50, 64, 67]. Figure A.1 illustrates a number of canard cycles computed

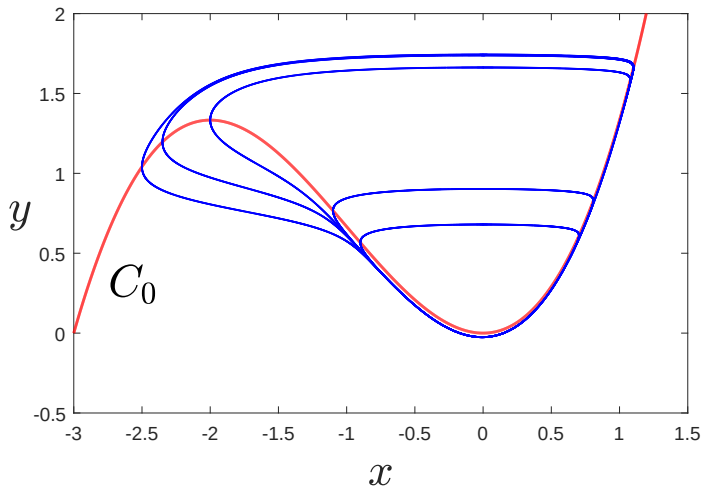

Figure A.1: Canard cycles in Van der pol. The family of canard cycles vary, over small parameter range $-0.00650907 < \lambda < -0.00650906$, from a small amplitude limit cycle to a relaxation oscillation. Computed for $\varepsilon = 0.05$.

numerically from the Van der Pol system:

$$\begin{aligned} x' &= x^2 + \frac{x^3}{3} - y \\ y' &= \varepsilon\,(x - \lambda) \end{aligned} \tag{A.9}$$

A more general definition of canard trajectories [64, 67] is:

Definition A.2.1. A trajectory segment of a slow-fast system is a *canard* if it stays within $\mathcal{O}(\varepsilon)$ distance to a repelling branch of a slow manifold for a time that is $\mathcal{O}(1)$ on the slow time scale $\tau = \varepsilon t$.

A special representation of canards trajectories is the one following the repelling slow manifold for the longest time, as in the following definition:

Definition A.2.2. A solution lying in the intersection of attracting and repelling slow manifolds $C_{\varepsilon,a} \bigcap C_{\varepsilon,r}$ near a nonhyperbolic point is called a *maximal canard*.

The loss of hyperbolicity near the intersection can be via fold, transcritical or pitchfork bifurcations [66, 75, 85]. Here we mention two theorems regarding canard

cycles near fold singularity in a slow-fast system satisfying the normal form

$$\begin{aligned} x' &= -\,y\; h_1(x,y,\lambda,\varepsilon) + x^2\; h_2(x,y,\lambda,\varepsilon) + \varepsilon\; h_3(x,y,\lambda,\varepsilon), \\ y' &= \varepsilon\left(\pm x\; h_4(x,y,\lambda,\varepsilon) - \lambda\; h_5(x,y,\lambda,\varepsilon) + y\; h_6(x,y,\lambda,\varepsilon)\right), \end{aligned} \tag{A.10}$$

where

$$\begin{aligned} h_3(x,y,\lambda,\varepsilon) =& \mathcal{O}(x,y,\lambda,\varepsilon), \\ h_j(x,y,\lambda,\varepsilon) =& 1 + \mathcal{O}(x,y,\lambda,\varepsilon), \quad j = 1,2,4,5. \end{aligned} \tag{A.11}$$

and define

$$\begin{aligned} a_1 =& \frac{\partial}{\partial x} h_3(0,0,0,0), \quad a_2 = \frac{\partial}{\partial x} h_1(0,0,0,0), \quad a_3 = \frac{\partial}{\partial x} h_2(0,0,0,0), \\ a_4 =& \frac{\partial}{\partial x} h_4(0,0,0,0), \quad a_5 = h_6(0,0,0,0), \quad A = -a_2 + 3a_3 - 2a_4 - 2a_5. \end{aligned} \tag{A.12}$$

Theorem A.2. *Suppose the slow-fast system* (A.10) *has a generic folded singularity and assume that the slow flow connects the two branches of the critical manifold $C_{0,a}$ and $C_{0,r}$. Then there exist $\varepsilon_0 > 0$ and a smooth function $\lambda = \lambda_c(\sqrt{\varepsilon})$ defined on $[0, \varepsilon_0]$ such that the following hold:*

(R1) $\Pi(q_{\varepsilon,a}) = q_{\varepsilon,r}$ *if and only if* $\lambda = \lambda_c(\sqrt{\varepsilon})$.

(R2) the function λ_c has the expansion

$$\lambda_c(\sqrt{\varepsilon}) = -\left(\frac{a_1 + a_5}{2} + \frac{A}{8}\right)\varepsilon + \mathcal{O}(\varepsilon^{3/2}); \tag{A.13}$$

(R3) the transition map Π is defined only for λ in an interval around $\lambda_c(\sqrt{\varepsilon})$ of width $\mathcal{O}\left(e^{-c/\varepsilon}\right)$ for some $c > 0$;

(R4) $\frac{\partial}{\partial \lambda}\left(\Pi(q_{\varepsilon,a}) - q_{\varepsilon,r}\right)|_{\lambda=\lambda_c(\sqrt{\varepsilon})} > 0$.

Theorem A.3. *Suppose the slow-fast system* (A.10) *has a generic folded singularity at $(x,y) = (0,0)$ for $\lambda = 0$. Then there exist $\varepsilon_0 > 0$ and $\lambda_0 > 0$ such that for $0 < \varepsilon < \varepsilon_0$ and $|\lambda| < \lambda_0$, in a suitable neighborhood of the origin, the system* (A.10) *has precisely one equilibrium point p with $p \to (0,0)$ as $(\lambda,\varepsilon) \to (0,0)$. Furthermore, there exists a curve $\lambda = \lambda_H(\sqrt{\varepsilon})$ Hopf bifurcations such that p is*

stable for $\lambda < \lambda_H(\sqrt{\varepsilon})$ *and*

$$\lambda_H(\sqrt{\varepsilon}) = -\left(\frac{a_1 + a_5}{2}\right)\varepsilon + \mathcal{O}(\varepsilon^{3/2}) \tag{A.14}$$

The Hopf bifurcation is nondegenerate when $A \neq 0$*, where* A *is defined in* (A.12)*. It is supercritical if* $A < 0$ *and subcritical if* $A > 0$*.*

The Hopf bifurcation concluded by Theorem A.3, which occurs at $\mathcal{O}(\varepsilon)$-distance from the fold point, is called *singular Hopf bifurcation* [50, 64]. Theorems A.2 and A.3 were proved using *blow-up technique,* which extends Fenichel's theory to non-hyperbolic points.

A. APPENDICES A

Appendix B

Dynamical Systems Techniques

B.1 Blow-up technique

The blow-up technique is a widely used method for geometric desingularization of nonhyperbolic equilibrium points [50, 64, 66, 75, 86].

As hyperbolic slow manifolds pass close to nonhyperbolic bifurcation equilibrium of a critical manifold, Fenichel's theory can no longer be applied. In this case, the blow-up technique might be used to desingularize the slow flow close to the bifurcation point by inserting a suitable manifold, *e.g.* sphere or cylinder, at the singularity and restore enough hyperbolicity to allow for a complete analysis of the local dynamics by established dynamical systems techniques.

Here we attempt to use minimum terminology from the theory of singularity to define two kinds of blow-up transformation (spherical and cylindrical) that are suitable for our analysis. Further theoretical terminology and general definitions for blow-up technique can be found in [64, 87–91].

Definition B.1.1. The *spherical blow-up* $\Phi_{\mathcal{S}} : B_{\mathcal{S}} \to \mathbb{R}^n$ is the mapping

$$\Phi_{\mathcal{S}}(\bar{x}_1, \ldots, \bar{x}_n, r) = (r^{\alpha_1}\bar{x}_1, \ldots, r^{\alpha_n}\bar{x}_n) = (x_1, \ldots, x_n) \tag{B.1}$$

with weights $(\alpha_1, \ldots, \alpha_n) \in \mathbb{N}^n$, where $B_{\mathcal{S}} = \mathcal{S}^{n-1} \times [0, \rho]$. Here the origin is blown-up

by $\Phi_{\mathcal{S}}$ to an $(n-1)$-sphere $\mathcal{S}^{n-1}$ determined by

$$\sum_{1\leq i\leq n} \bar{x}_i^2 = 1.$$

Definition B.1.2. The *cylindrical blow-up* $\Phi_{\mathcal{C}} : B_{\mathcal{C}} \to \mathbb{R}^n$ around the x_j-axis is the mapping

$$\Phi_{\mathcal{C}}(\bar{x}_1, \ldots, \bar{x}_n, r) = (r^{\alpha_1}\bar{x}_1, \ldots, r^{\alpha_n}\bar{x}_n) = (x_1, \ldots, x_n) \tag{B.2}$$

with weights $(\alpha_1, \ldots, \alpha_n) \in \mathbb{N}^n$ and $\alpha_j = 0$ for some $1 \leq j \leq n$, where $B_{\mathcal{C}} = \mathcal{C}^{n-1} \times [0, \rho]$. Here the x_j-axis is blown-up by $\Phi_{\mathcal{C}}$ to an $(n-1)$-cylinder $\mathcal{C}^{n-1} = \mathcal{S}^{n-2} \times \mathbb{R}$, where $\mathcal{S}^{n-2}$ is determined by

$$\sum_{\substack{1\leq i\leq n \\ i\neq j}} \bar{x}_i^2 = 1.$$

Now, consider the vector field:

$$X' = F(X); \tag{B.3}$$

where $X = [x_1, \ldots, x_n]^\top$ and $F = [f_1, \ldots, f_n]^\top$. In order to determine appropriate weights $(\alpha_1, \ldots, \alpha_n)$ leading to a suitable blow-up Φ (denoting to either spherical or cylindrical transformation), the following property should be considered:

Definition B.1.3. A function $f : \mathbb{R}^n \to \mathbb{R}$ is called *quasihomogeneous* of type $(\alpha_1, \ldots, \alpha_n) \in \mathbb{N}^n$ and degree k if for every $r \in \mathbb{R}$,

$$f(r^{\alpha_1}x_1, \ldots, r^{\alpha_n}x_n) = r^k f(x_1, \ldots, x_n) \tag{B.4}$$

Definition B.1.4. A vector field F is called *quasihomogeneous* of type $(\alpha_1, \ldots, \alpha_n) \in \mathbb{N}^n$ and degree $k+1$ if its jth component functions $f_j(x_1, \ldots, x_n)$ is quasihomogeneous of type $(\alpha_1, \ldots, \alpha_n)$ and degree $k + \alpha_j$, *i.e.*

$$F(r^{\alpha_1}x_1, \ldots, r^{\alpha_n}x_n) = r^k[r^{\alpha_1}f_1(x_1, \ldots, x_n), \ldots, r^{\alpha_n}f_n(x_1, \ldots, x_n)]^\top \tag{B.5}$$

Now we can define the vector field resulting from the blow-up transformation,

Definition B.1.5. Let F be a C^∞ vector field on $\mathbb{R}^n$ with $F(0) = 0$. The *blown-up*

vector field $\hat{F}$ defined by the blow-up transformation Φ is given by

$$\hat{F}(\bar{x}_1, \ldots, \bar{x}_n, r) := \left(D^{-1}_{(\bar{x}_1,\ldots,\bar{x}_n,r)} \Phi \circ F \circ \Phi \right) (\bar{x}_1, \ldots, \bar{x}_n, r) \tag{B.6}$$

If, in addition, F is a quasihomogeneous vector field of type $(\alpha_1, \ldots, \alpha_n)$ and degree $k+1$, then the *rescaled blown-up vector field* $\bar{F}$ is defined as

$$\bar{F} := \frac{1}{r^k} \hat{F} \tag{B.7}$$

If the vector field F of singularity at the origin has been blown-up by the transformation Φ and the resulted rescaled blown-up vector field $\hat{F}$ has either hyperbolic or partially hyperbolic isolated equilibrium points, then $\hat{F}$ ia called *desingularisation* of the vector F.

Analysing the dynamic of the blown-up vector field $\bar{F}$ on the manifold B might lead to rather lengthy computations [66]. Alternatively, the analysis can be simplified by using directional blowups which map the local dynamics on B into different charts K_i and reduce the problem to $\mathbb{R}^n$ coordinates.

Definition B.1.6. The *directional blow-ups* $(\Phi_i, \ i = 1, \ldots, n)$ are obtained by setting the variable $\bar{x}_i$ to ± 1 in Definitions B.1.1 and B.1.2. The resulted charts and vector fields defined on it are respectively denoted by K_i and F_j

Each directional blow-up covers only one part of the dynamics on the manifold B. Patching all directional blown-up vector fields together describes the dynamics of the vector field $\bar{F}$ on B. The change of coordinates from chart K_i to chart K_j is denoted as κ_{ij}.

Hence, to desingularize a vector field of singular origin, the blow-up technique requires the following steps [64]:

- Step 1: Find a suitable blow-up map to desingularize the singular point.
- Step 2: Find charts to express the blow-up in local coordinates.
- Step 3: Calculate all the local data of the problem.
- Step 4: Investigate the local dynamics of the blown-up vector fields.
- Step 5: Connect the results from different charts and blow-down.

B.2 Poincaré sphere

The behaviour of trajectories on (x, y)-plane far from the origin can be studied by projecting them into the so-called Poincaré sphere, where the unit sphere

$$\mathcal{S}^2 = \left\{(X, Y, Z) \in \mathbb{R}^3 : X^2 + Y^2 + Z^2 = 1\right\} \tag{B.8}$$

is projected onto the (x, y)-plane, which is tangent to either the north or south pole of $\mathcal{S}^2$ at the origin. The transformation

$$X = \frac{x}{\sqrt{1 + x^2 + y^2}}, \qquad Y = \frac{y}{\sqrt{1 + x^2 + y^2}}, \qquad Z = \frac{1}{\sqrt{1 + x^2 + y^2}}. \tag{B.9}$$

defines a one-to-one correspondence between the points (x, y) in the plane and the points (X, Y, Z) on one of the hemisphere (we consider $Z \geq 0$); it follows that $x = X/Z$ and $y = Y/Z$. The advantage of using the Poincaré sphere is that the critical points at infinity are spread out along its equator,

$$\mathcal{S}^1 = \left\{(X, Y, Z) \in \mathbb{R}^3 : X^2 + Y^2 = 1, \quad Z = 0\right\} \tag{B.10}$$

However, some of the critical points at infinity projected on the Poincaré sphere may still be very complicated in nature and their analysis requires using other methods, *e.g.* the blow-up technique.

Consider the flow defined by a planar dynamical system

$$\begin{aligned} x' &= P(x, y) \\ y' &= Q(x, y) \end{aligned} \tag{B.11}$$

where P and Q are polynomial functions of x and y with maximum degree m. The flow on the Poincaré sphere $\mathcal{S}^2$ is defined by [54]

$$Q(X/Z, Y/Z)(ZdX - XdZ) - P(X/Z, Y/Z)(ZdY - YdZ) = 0 \tag{B.12}$$

The flow defined by (B.12) allows us to study the behaviour of the flow defined by (B.11) at infinity; in a neighbourhood of the equator of $\mathcal{S}^2$.

Theorem B.1. *The critical points at infinity for the system* (B.12) *occur at the*

points $(X, Y, 0)$ *on the equator of the Poincaré sphere where* $X^2 + Y^2 = 1$ *and*

$$G(X, Y) := XQ_m(X, Y, 0) - YP_m(X, Y, 0) = 0 \tag{B.13}$$

where,

$$\begin{aligned} P_m(X, Y, Z) &= Z^m\, P(X/Z, Y/Z) \\ Q_m(X, Y, Z) &= Z^m\, Q(X/Z, Y/Z) \end{aligned} \tag{B.14}$$

If $G(X, Y, 0)$ *is not identically zero, then the flow on the equator of the Poincaré sphere is counter-clockwise if* $G(X, Y, 0) > 0$ *and it is clockwise if* $G(X, Y, 0) < 0$.

Theorem B.2. *The flow defined by* (B.12) *in a neighborhood of any critical point on the equator of the Poincaré sphere* $\mathcal{S}^2$*, except the points* $(0, \pm 1, 0)$*, is topologically equivalent to the flow defined by the system*

$$\begin{aligned} \pm y' &= yz^m P\left(\frac{1}{z}, \frac{y}{z}\right) - z^m Q\left(\frac{1}{z}, \frac{y}{z}\right) \\ \pm z' &= z^{m+1} P\left(\frac{1}{z}, \frac{y}{z}\right) \end{aligned} \tag{B.15}$$

the signs being determined by the flow on the equator of $\mathcal{S}^2$ *as determined in Theorem B.1. Similarly, the flow defined by* (B.12) *in a neighborhood of any critical point on the equator of* $\mathcal{S}^2$*, except the points* $(\pm 1, 0, 0)$*, is topologically equivalent to the flow defined by the system*

$$\begin{aligned} \pm x' &= xz^m Q\left(\frac{x}{z}, \frac{1}{z}\right) - z^m P\left(\frac{x}{z}, \frac{1}{z}\right) \\ \pm z' &= z^{m+1} Q\left(\frac{x}{z}, \frac{1}{z}\right) \end{aligned} \tag{B.16}$$

the signs being determined by the flow on the equator of $\mathcal{S}^2$ *as determined in Theorem B.1.*

References

[1] J. Diedrichsen. **Motor coordination**. *Scholarpedia*, **7**(12):12309, 2012. revision #129329. 1

[2] Raoul Huys and Viktor K Jirsa. *Nonlinear dynamics in human behavior*, **328**. Springer, 2010. 1, 2, 9, 95

[3] James AS Kelso. **Coordination dynamics**. In *Encyclopedia of complexity and systems science*, pages 1537–1565. Springer, 2009. 1, 3, 4, 7, 8

[4] PJ Beek, CE Peper, and DF Stegeman. **Dynamical models of movement coordination**. *Human Movement Science*, **14**(4):573–608, 1995. 1, 2

[5] PJ Beek, CE Peper, and Andreas Daffertshofer. **Modeling rhythmic interlimb coordination: Beyond the Haken–Kelso–Bunz model**. *Brain and cognition*, **48**(1):149–165, 2002. 2

[6] BA Kay, JA Kelso, EL Saltzman, and G Schöner. **Space–time behavior of single and bimanual rhythmical movements: Data and limit cycle model.** *Journal of Experimental Psychology: Human Perception and Performance*, **13**(2):178, 1987. 2, 5, 8, 9, 12, 13, 14, 15, 26, 27, 28, 29, 30, 98, 100, 112, 115, 116, 120

[7] Chao Zhai, Francesco Alderisio, Piotr Słowiński, Krasimira Tsaneva-Atanasova, and Mario di Bernardo. **Design and validation of a virtual player for studying interpersonal coordination in the mirror game**. *IEEE transactions on cybernetics*, 2017. 1, 2, 9

[8] Hermann Haken, JA Scott Kelso, and Heinz Bunz. **A theoretical model of phase transitions in human hand movements**. *Biological cy-*

bernetics, **51**(5):347–356, 1985. 1, 2, 4, 5, 6, 7, 8, 12, 13, 26, 28, 30, 95, 96, 99, 112, 119, 120, 121

[9] Viktor K Jirsa and JA Scott Kelso. **The excitator as a minimal model for the coordination dynamics of discrete and rhythmic movement generation**. *Journal of motor behavior*, **37**(1):35–51, 2005. 1, 2, 9, 10, 13, 32, 42, 43, 44, 94, 110, 117, 121, 122, 124

[10] JA Scott Kelso and G Schöner. **Self-organization of coordinative movement patterns**. *Human Movement Science*, **7**(1):27–46, 1988. 1

[11] Hermann Haken, CE Peper, Peter J Beek, and Andreas Daffertshofer. **A model for phase transitions in human hand movements during multifrequency tapping**. *Physica D: Nonlinear Phenomena*, **90**(1):179–196, 1996. 2, 3

[12] Peter J Beek, Walther EI Rikkert, and Piet CW van Wieringen. **Limit cycle properties of rhythmic forearm movements.** *Journal of Experimental Psychology: Human Perception and Performance*, **22**(5):1077, 1996. 2, 5, 8, 12, 26, 30, 100, 112, 120

[13] Philip W Fink, JA Scott Kelso, and Viktor K Jirsa. **Perturbation-induced false starts as a test of the Jirsa-Kelso Excitator model**. *Journal of motor behavior*, **41**(2):147–157, 2009. 2, 9, 10, 42, 94, 122, 124

[14] JA Scott Kelso, Gonzalo C de Guzman, Colin Reveley, and Emmanuelle Tognoli. **Virtual partner interaction (VPI): exploring novel behaviors via coordination dynamics**. *PloS one*, **4**(6):e5749, 2009. 2, 9, 12, 30

[15] Guillaume Dumas, Gonzalo C de Guzman, Emmanuelle Tognoli, and JA Scott Kelso. **The human dynamic clamp as a paradigm for social interaction**. *Proceedings of the National Academy of Sciences*, **111**(35):E3726–E3734, 2014. 9

[16] Manuel Varlet, Ludovic Marin, Stéphane Raffard, Richard C Schmidt, Delphine Capdevielle, Jean-Philippe Boulenger,

Jonathan Del-Monte, and Benoît G Bardy. **Impairments of social motor coordination in schizophrenia**. *PloS one*, **7**(1):e29772, 2012. 2, 9, 13, 96, 120

[17] H. Haken. **Synergetics**. *Scholarpedia*, **2**(1):1400, 2007. revision #87434. 2, 3, 4

[18] C Lieke E Peper and Peter J Beek. **Modeling rhythmic interlimb coordination: The roles of movement amplitude and time delays**. *Human Movement Science*, **18**(2):263–280, 1999. 3, 7, 8, 9, 99

[19] JA Kelso. **Phase transitions and critical behavior in human bimanual coordination**. *American Journal of Physiology-Regulatory, Integrative and Comparative Physiology*, **246**(6):R1000–R1004, 1984. 3, 15, 95, 116

[20] JAS Kelso. **On the oscillatory basis of movement**. In *Bulletin of the psychonomic society*, **18**, pages 63–63. PSYCHONOMIC SOC INC 1710 FORTVIEW RD, AUSTIN, TX 78704, 1981. 3

[21] JA Kelso, JD Del Colle, and Gregor Schöner. **Action-perception as a pattern formation process.** 1990.

[22] Richard C Schmidt, Claudia Carello, and Michael T Turvey. **Phase transitions and critical fluctuations in the visual coordination of rhythmic movements between people.** *Journal of experimental psychology: human perception and performance*, **16**(2):227, 1990.

[23] CE Peper, PJ Beek, and PCW Van Wieringen. **Bifurcations in polyrhythmic tapping: In search of Farey principles**. In *Tutorials in motor neuroscience*, pages 413–431. Springer, 1991.

[24] Raymond H Wimmers, Peter J Beek, and Piet CW van Wieringen. **Phase transitions in rhythmic tracking movements: A case of unilateral coupling**. *Human Movement Science*, **11**(1-2):217–226, 1992.

[25] Winston D Byblow, Richard G Carson, and David Goodman. **Expressions of asymmetries and anchoring in bimanual coordination**. *Human Movement Science*, **13**(1):3–28, 1994.

[26] Winston D Byblow, R Chua, and D Goodman. **Asymmetries in coupling dynamics of perception and action**. *Journal of Motor Behavior*, **27**(2):123–137, 1995.

[27] John J Jeka and JAS Kelso. **Manipulating symmetry in the coordination dynamics of human movement.** *Journal of Experimental Psychology: Human Perception and Performance*, **21**(2):360, 1995.

[28] C Lieke E Peper, Peter J Beek, and Piet CW van Wieringen. **Frequency-induced phase transitions in bimanual tapping**. *Biological cybernetics*, **73**(4):301–309, 1995.

[29] C Lieke E Peper and Peter J Beek. **Are frequency-induced transitions in rhythmic coordination mediated by a drop in amplitude?** *Biological cybernetics*, **79**(4):291–300, 1998. 3, 4, 5, 7, 8, 9, 12, 30, 96

[30] Hermann Haken. **SYNERGETICS-An Introduction: Nonequilibrium Phase Transition and Self-Organization in Physics**. *Chemistry and Biology*, 1978. 4, 95

[31] Armin Fuchs and Viktor K Jirsa. **JA Scott Kelsos contributions to our understanding of coordination**. *Coordination: Neural, Behavioral and Social Dynamics*, pages 327–346, 2008. 4

[32] Gregor Schöner, H Haken, and JAS Kelso. **A stochastic theory of phase transitions in human hand movement**. *Biological cybernetics*, **53**(4):247–257, 1986. 9

[33] JAS Kelso, G Schöner, JP Scholz, and H Haken. **Phase-locked modes, phase transitions and component oscillators in biological motion**. *Physica Scripta*, **35**(1):79, 1987. 9

[34] JAS Kelso. **The informational character of self-organized coordination dynamics**. *Human Movement Science*, **13**(3):393–413, 1994. 121

[35] B. Ermentrout. **XPPAUT**. *Scholarpedia*, **2**(1):1399, 2007. revision #136177. 25

[36] Viktor K Jirsa, R Friedrich, Hermann Haken, and JA Scott Kelso. **A theoretical model of phase transitions in the human brain**. *Biological cybernetics*, **71**(1):27–35, 1994.

[37] Armin Fuchs and JA Kelso. **A theoretical note on models of interlimb coordination.** *Journal of Experimental Psychology: Human Perception and Performance*, **20**(5):1088, 1994. 9

[38] Raoul Huys, Breanna E Studenka, Nicole L Rheaume, Howard N Zelaznik, and Viktor K Jirsa. **Distinct timing mechanisms produce discrete and continuous movements**. *PLoS Comput Biol*, **4**(4):e1000061, 2008. 9, 42

[39] Raoul Huys, Dionysios Perdikis, and Viktor K Jirsa. **Functional architectures and structured flows on manifolds: A dynamical framework for motor behavior.** *Psychological review*, **121**(3):302, 2014. 9, 42

[40] Richard FitzHugh. **Impulses and physiological states in theoretical models of nerve membrane**. *Biophysical journal*, **1**(6):445, 1961. 10, 13, 35, 121

[41] Carmen Rocsoreanu, Adelina Georgescu, and Nicolaie Giurgiteanu. *The FitzHugh-Nagumo model: bifurcation and dynamics*, **10**. Springer Science & Business Media, 2012. 11, 13, 42, 47, 48, 52, 57

[42] Eugene M Izhikevich. *Dynamical systems in neuroscience*. MIT press, 2007.

[43] William Erik Sherwood. **Fitzhugh–nagumo model**. *Encyclopedia of Computational Neuroscience*, pages 1202–1211, 2015. 11

[44] Arpan Banerjee and Viktor K Jirsa. **How do neural connectivity and time delays influence bimanual coordination?** *Biological Cybernetics*, **96**(2):265–278, 2007. 11, 13, 96, 99, 100, 106, 110, 111, 112, 116, 120, 121

[45] B Tuller and JAS Kelso. **Environmentally-specified patterns of movement coordination in normal and split-brain subjects**. *Experimental Brain Research*, **75**(2):306–316, 1989. 11, 121

[46] Daniele Avitabile, Piotr Słowiński, Benoit Bardy, and Krasimira Tsaneva-Atanasova. **Beyond in-phase and anti-phase coordination in a model of joint action**. *Biological Cybernetics*, pages 1–16, 2016. 12, 13, 18, 19, 20, 21, 25, 119, 123

[47] Piotr Słowiński, Krasimira Tsaneva-Atanasova, and Bernd Krauskopf. **Effects of time-delay in a model of intra-and interpersonal motor coordination**. *The European Physical Journal Special Topics*, **225**(13-14):2591–2600, 2016. 12, 13, 30, 96, 98, 99, 100, 112, 120

[48] Tanya Leise and Andrew Cohen. **Nonlinear oscillators at our fingertips**. *American Mathematical Monthly*, **114**(1):14–28, 2007. 12, 27, 28, 96, 119, 120

[49] Till D Frank, Paula L Silva, and Michael T Turvey. **Symmetry axiom of Haken–Kelso–Bunz coordination dynamics revisited in the context of cognitive activity**. *Journal of Mathematical Psychology*, **56**(3):149–165, 2012. 12, 96

[50] Martin Krupa and Peter Szmolyan. **Relaxation oscillation and canard explosion**. *Journal of Differential Equations*, **174**(2):312–368, 2001. 13, 51, 52, 60, 77, 132, 135, 137

[51] M Desroches and MR Jeffrey. **Canards and curvature: the 'smallness of ε' in slow-fast dynamics**. *Proceedings of the Royal Society of London Series A*, **467**:2404–2421, 2011. 13, 60, 77, 79, 80, 82, 84

[52] Paul Glendinning. *Stability, Instability and Chaos: An Introduction to the Theory of Nonlinear Differential Equations*. Cambridge University Press, 1994. 20, 21, 28

[53] Shui-Nee Chow, Chengzhi Li, and Duo Wang. *Normal forms and bifurcation of planar vector fields*. Cambridge University Press, 1994. 20

[54] Lawrence Perko. *Differential equations and dynamical systems*, **7**. Springer Science & Business Media, 2013. 21, 68, 140

[55] John Guckenheimer and Philip Holmes. *Nonlinear oscillations, dynamical systems, and bifurcations of vector fields*, **42**. Springer Science & Business Media, 2013.

[56] Yuri A Kuznetsov. *Elements of applied bifurcation theory*, **112**. Springer Science & Business Media, 2013. 21, 34, 52, 55

[57] Eusebius J Doedel. **AUTO: A program for the automatic bifurcation analysis of autonomous systems**. *Congr. Numer*, **30**:265–284, 1981. 25, 93

[58] J.A. Sanders, F. Verhulst, and J. Murdock. *Averaging methods in nonlinear dynamical systems*. Number 59 in Applied Mathematical Sciences. Springer, 2007. MR2316999. 28

[59] Viviane Kostrubiec, Guillaume Dumas, Pier-Giorgio Zanone, and JA Scott Kelso. **The virtual teacher (VT) paradigm: learning new patterns of interpersonal coordination using the human dynamic clamp**. *PloS one*, **10**(11):e0142029, 2015. 30

[60] Piotr Słowiński, Sohaib Al-Ramadhani, and Krasimira Tsaneva-Atanasova. **Relaxation oscillations and canards in the Jirsa-Kelso excitator model: global flow perspective**. *The European Physical Journal Special Topics*, 2018. 35, 68

[61] Stephen Schecter. **The saddle-node separatrix-loop bifurcation**. *SIAM journal on mathematical analysis*, **18**(4):1142–1156, 1987. 42

[62] John Guckenheimer. **Singular Hopf bifurcation in systems with two slow variables**. *SIAM Journal on Applied Dynamical Systems*, **7**(4):1355–1377, 2008. 43, 51, 52, 60

[63] Mathieu Desroches, John Guckenheimer, Bernd Krauskopf, Christian Kuehn, Hinke M Osinga, and Martin Wechselberger. **Mixed-mode oscillations with multiple time scales**. *Siam Review*, **54**(2):211–288, 2012. 51, 129

[64] Christian Kuehn. *Multiple time scale dynamics*, **191**. Springer, 2015. 43, 60, 129, 132, 133, 135, 137, 139

[65] Neil Fenichel. **Persistence and smoothness of invariant manifolds for flows**. *Indiana Univ. Math. J*, **21**(193-226):1972, 1971. 60, 129

[66] M Krupa and Peter Szmolyan. **Extending geometric singular perturbation theory to nonhyperbolic points—fold and canard points in two dimensions**. *SIAM journal on mathematical analysis*, **33**(2):286–314, 2001. 63, 77, 132, 133, 137, 139

[67] M. Wechselberger. **Canards**. *Scholarpedia*, **2**(4):1356, 2007. revision #152256. 60, 77, 132, 133

[68] Christian Kuehn. **A Remark on Geometric Desingularization of a Non-Hyperbolic Point using Hyperbolic Space**. *arXiv preprint arXiv:1403.3789*, 2014. 71

[69] J Rankin, M Desroches, B Krauskopf, and M Lowenberg. **Canard cycles in aircraft ground dynamics**. *Nonlinear Dynamics*, **66**(4):681–688, 2011. 76, 94, 123, 126, 132

[70] Elena Bossolini, Morten Brøns, and Kristian Uldall Kristiansen. **Singular limit analysis of a model for earthquake faulting**. *Nonlinearity*, **30**(7):2805, 2017. 76, 123, 126

[71] Kristian Uldall Kristiansen. **Blowup for flat slow manifolds**. *Nonlinearity*, **30**(5):2138, 2017. 76, 123, 126

[72] Mathieu Desroches and Mike R Jeffrey. **Canards and curvature: nonsmooth approximation by pinching**. *Nonlinearity*, **24**(5):1655, 2011. 77, 79

[73] Mathieu Desroches, Martin Krupa, and Serafim Rodrigues. **Inflection, canards and excitability threshold in neuronal models**. *Journal of mathematical biology*, **67**(4):989–1017, 2013. 77, 79

[74] Christian Kuehn. **From first Lyapunov coefficients to maximal canards**. *International Journal of Bifurcation and Chaos*, **20**(05):1467–1475, 2010. 77, 80

[75] M Krupa and P Szmolyan. **Extending slow manifolds near transcritical and pitchfork singularities**. *Nonlinearity*, **14**(6):1473, 2001. 77, 132, 133, 137

[76] Shinji Doi, Takahiro Kodama, and Hiroki Oosaki. **Importance of sufficient precision in stable dynamics for the numerical computation of canards in singularly perturbed systems**. *Nonlinear Theory and Its Applications, IEICE*, **6**(4):454–465, 2015. 79

[77] Jeff Moehlis. **Canards for a reduction of the Hodgkin-Huxley equations**. *Journal of mathematical biology*, **52**(2):141–153, 2006. 79

[78] John Guckenheimer and Christian Kuehn. **Computing slow manifolds of saddle type**. *SIAM Journal on Applied Dynamical Systems*, **8**(3):854–879, 2009. 85

[79] Bernd Krauskopf and Hinke M Osinga. **Computing invariant manifolds via the continuation of orbit segments**. In *Numerical Continuation Methods for Dynamical Systems*, pages 117–154. Springer, 2007.

[80] Mathieu Desroches, Bernd Krauskopf, and Hinke M Osinga. **Numerical continuation of canard orbits in slow–fast dynamical systems**. *Nonlinearity*, **23**(3):739, 2010. 85

[81] Jan Sieber, Koen Engelborghs, Tatyana Luzyanina, Giovanni Samaey, and Dirk Roose. **DDE-BIFTOOL Manual-Bifurcation analysis of delay differential equations**. *arXiv preprint arXiv:1406.7144*, 2014. 96, 102

[82] Ian D Loram, Peter J Gawthrop, and Martin Lakie. **The frequency of human, manual adjustments in balancing an inverted pendulum is constrained by intrinsic physiological factors**. *The Journal of physiology*, **577**(1):417–432, 2006. 98, 112

[83] T Heil, I Fischer, W Elsässer, B Krauskopf, K Green, and A Gavrielides. **Delay dynamics of semiconductor lasers with short**

external cavities: Bifurcation scenarios and mechanisms. *Physical Review E*, **67**(6):066214, 2003. 102

[84] JA Scott Kelso. *Dynamic patterns: The self-organization of brain and behavior*. MIT press, 1997. 121

[85] Peter De Maesschalck. **Planar Canards with Transcritical Intersections**. *Acta Applicandae Mathematicae*, **137**(1):159–184, 2015. 133

[86] Christian Kuehn. **Normal hyperbolicity and unbounded critical manifolds**. *Nonlinearity*, **27**(6):1351, 2014. 137

[87] Freddy Dumortier. **Techniques in the theory of local bifurcations: Blow-up, normal forms, nilpotent bifurcations, singular perturbations**. In *Bifurcations and periodic orbits of vector fields*, pages 19–73. Springer, 1993. 137

[88] Freddy Dumortier. **Singularities of vector fields on the plane**. *Journal of Differential Equations*, **23**(1):53–106, 1977.

[89] Freddy Dumortier and S Ibánez. **Singularities of vector fields on**. *Nonlinearity*, **11**(4):1037, 1998.

[90] Robert Roussarie. **Techniques in the theory of local bifurcations: cyclicity and desingularization**. In *Bifurcations and Periodic Orbits of Vector Fields*, pages 347–382. Springer, 1993.

[91] Zofia Denkowska and Robert Roussarie. **A method of desingularization for analytic two-dimensional vector field families**. *Boletim da Sociedade Brasileira de Matemática-Bulletin/Brazilian Mathematical Society*, **22**(1):93–126, 1991. 137